creative commons
COMMONS DEED

저작자표시-비영리-변경금지 2.0 대한민국

이용자는 아래의 조건을 따르는 경우에 한하여 자유롭게

- 이 저작물을 복제, 배포, 전송, 전시, 공연 및 방송할 수 있습니다.

다음과 같은 조건을 따라야 합니다:

**저작자표시**. 귀하는 원저작자를 표시하여야 합니다.

**비영리**. 귀하는 이 저작물을 영리 목적으로 이용할 수 없습니다.

**변경금지**. 귀하는 이 저작물을 개작, 변형 또는 가공할 수 없습니다.

- 귀하는, 이 저작물의 재이용이나 배포의 경우, 이 저작물에 적용된 이용허락조건을 명확하게 나타내어야 합니다.
- 저작권자로부터 별도의 허가를 받으면 이러한 조건들은 적용되지 않습니다.

**저작권법에 따른 이용자의 권리는 위의 내용에 의하여 영향을 받지 않습니다.**

이것은 이용허락규약(Legal Code)을 이해하기 쉽게 요약한 것입니다.

Disclaimer

dCollection

공학박사 학위논문

LAYERED DOUBLE HYDROXIDE BASED
NANOHYBRIDS FOR DIAGNOSIS AND THERAPY

# 진단 및 치료를 위한 금속 이중층 수산화물 기반의 나노복합체 연구

2016 년 8 월

서울대학교 대학원

협동과정 바이오엔지니어링 전공

김 명 훈

LAYERED DOUBLE HYDROXIDE BASED
NANOHYBRIDS FOR DIAGNOSIS AND THERAPY

# 진단 및 치료를 위한 금속 이중층 수산화물 기반의 나노복합체 연구

지도 교수 최 영 빈

이 논문을 공학박사 학위논문으로 제출함

2016 년 8 월

서울대학교 대학원

협동과정 바이오엔지니어링 전공

김 명 훈

김명훈의 공학박사 학위논문을 인준함

2016 년 7 월

위 원 장 김 희 찬 (인)

부위원장 최 영 빈 (인)

위 원 최 태 현 (인)

위 원 이 정 찬 (인)

위 원 최 진 호 (인)

Ph. D. Dissertation

# LAYERED DOUBLE HYDROXIDE BASED NANOHYBRIDS FOR DIAGNOSIS AND THERAPY

BY

MYUNG HUN KIM

AUGUST 2016

INTERDISCIPLINARY PROGRAM IN BIOENGINEERING

THE GRADUATE SCHOOL

SEOUL NATIONAL UNIVERSITY

# LAYERED DOUBLE HYDROXIDE BASED NANOHYBRIDS FOR DIAGNOSIS AND THERAPY

BY

MYUNG HUN KIM

INTERDISCIPLINARY PROGRAM IN BIOENGINEERING

THE GRADUATE SCHOOL

SEOUL NATIONAL UNIVERSITY

THIS DISSERTATION IS APPROVED FOR THE DEGREE OF DOCTOR OF PHILOSOPHY

JULY 2016

DOCTORAL COMMITTEE:

| | |
|---|---|
| Chairman | *Hee Chan Kim, Ph. D.* |
| Vice Chairman | *Young Bin Choy, Ph. D.* |
| Member | *Tae Hyun Choi, MD, Ph. D.* |
| Member | *Jung Chan Lee, Ph. D.* |
| Member | *Jin-Ho Choy, Ph.D.* |

# Abstract

## LAYERED DOUBLE HYDROXIDE BASED NANOHYBRIDS FOR DIAGNOSIS AND THERAPY

By

*Myung Hun Kim*

Interdisciplinary Program in Bioengineering

The Graduate School

Seoul National University

In this dissertation, among various biomedical engineering fields, I have studied not only the accurate diagnosis but also appropriate therapy of diseases with layered double hydroxide (LDH) based nanohybrids to advance health care treatment (e. g. diagnosis, monitoring, and therapy). Moreover, the nanohybrids can give body to theranostic system, which could develop more specific, personalized treatments for various diseases, and integrate diagnostic and therapeutic functionalities into a single agent.

This dissertation is focused on the design, fabrication and evaluation of layered double hydroxide (LDH) based nanohybrids for diagnosis and therapy. LDHs as drug delivery carriers have attracted a great deal of attentions due to their interesting properties to release of drugs in a controlled/sustained manner, to facilitate cellular interaction, and to enhance cellular uptake, which eventually leads to a high efficacy of drugs. In chapter 2, a novel gel formulation of the drug encapsulated LDH nanohybrid have a potential for transdermal controlled drug delivery system (DDS). In chapter 3, the drug loaded LDH nanohybrid could be considered as a promising DDS for improving intracellular drug efficacy, which results in higher therapeutic efficacy.

In Chapter 4, I propose a bioabsorbable bone plate enabled with diagnostic X-ray visibility. LDHs can work as radiopaque materials thanks to their chemical compositions containing di- and trivalent metals with higher X-ray attenuation coefficients, such as magnesium (0.1686 $cm^2/g$), aluminum (0.1704 $cm^2/g$), and zinc (0.4973 $cm^2/g$). The radiopaque fixation plate, in which radiopaque sheets made of a fine powder of layered metal hydroxides (LMHs) as radiopaque agents and poly (lactic-co-glycolic acid) (PLGA) as a biodegradable binder material, is attached onto a bioabsorbable bone plate approved for clinical use, is a promising fixation device enabled with X-ray visibility, biodegradability, and biocompatibility.

In chapter 5, with those diagnostic and therapeutic functionalities, I finally develop a theranostic bone plate in

combination with the theranostic drug intercalated LDH nanohybrid. which can be a promising system enabled with dual functionalities of both diagnostic X-ray visibility and therapeutic expedited bone repair.

- Keywords : layered double hydroxide, nanohybrid, diagnosis, therapy, theranosis

- Student Number : 2010-21053

# Contents

Abstract ..... i

Contents ..... iv

List of Tables ..... x

List of Figures ..... xi

Part I. General Introduction ..... 1

Chapter 1. Introduction ..... 2

1.1 Research Backgrounds ..... 2

1.2 Layered Double Hydroxides (LDHs) ..... 5

1.3 Synthetic Routes for LDH Based Nanohybrids ..... 10

1.4 Research Aims ..... 14

Part II. Layered Double Hydroxide Based Nanohybrid as Therapeutic Agent ..... 17

Chapter 2. Drug-Inorganic-Polymer Nanohybrid for Transdermal Drug Delivery ..... 18

2.1 Abstract ..... 18

2.2 Introduction ..... 20

2.3 Experimental Section ..... 22

2.3.1 Materials .....22
2.3.2 Preparation of FB-LDH Nanohybrid ..... 24
2.3.3 Preparation of FB-LDH Gel Formulations..... 24
2.3.4 Characterizations of FB-LDH Nanohybrid ..... 25
2.3.4.1 Powder X-ray Diffraction (PXRD) .....25
2.3.4.2 Fourier Transform Infrared (FT-IR) .....26
2.3.4.3 Scanning Electron Microscopy (SEM) .....26
2.3.4.4 Transmission Electron Microscopy (TEM) .....26
2.3.4.5 Particle Size Distribution and Zeta Potential Measurements .....27
3.3.4.6 Characterizations of FB-LDH Nanohybrid .....27
3.3.4.7 High Performance Liquid Chromatography (HPLC) Analysis .....27
2.3.5 *In vitro* Drug Release Test..... 28
2.3.6 *In vitro* Skin Permeability Test..... 28
2.4 Results and Discussion .....30
2.4.1 PXRD Analysis ..... 30
2.4.2 FT-IR Analysis ..... 36
2.4.3 Particle Analysis..... 38
2.4.4 Thermal Analysis ..... 41
2.4.5 *In vitro* Release Test of the FB-LDH..... 46
2.4.6 *In vitro* Skin Permeability Test of the FB-LDH Formulations ..... 48
2.5 Conclusion .....52

Chapter 3. Alendronate-Layered Double Hydroxide Nanohybrid for *In vitro* Enhancement of Osteogenic Proliferation and Differentiation of MG63 Cells ..... 53

3.1 Abstract ..... 53

3.2 Introduction ..... 55

3.3 Experimental Section ..... 58

3.3.1 Materials ..... 58

3.3.2 Preparation of Nanohybrids ..... 58

3.3.3 Characterizations ..... 61

3.3.4 *In vitro* Drug Release Test ..... 62

3.3.5 *In vitro* Cell Study ..... 62

3.3.5.1 Quantification of Accumulated AL in MG63 Cells ..... 63

3.3.5.2 Confocal Laser Scanning Microscopy Study ..... 64

3.3.5.3 Proliferation Study ..... 64

3.3.5.4 Alkaline Phosphatase (ALP) Activity ..... 65

3.3.6 Statistical Analysis ..... 66

3.4 Results and Discussion ..... 67

3.4.1 Powder X-ray Diffraction (PXRD) Analysis ..... 67

3.4.2 High Resolution Transmission Electron Microscopy (HR-TEM) Study of the AL-LDH ..... 70

3.4.3 Fourier Transform Infrared (FT-IR) Analysis ..... 76

3.4.4 Particle Analysis ..... 78

3.4.5 UV-Vis Spectroscopy Analysis ..... 80

3.4.6 *In vitro* Release Test ..... 82

3.4.7 Cellular Uptake Studies ..... 87
3.4.8 *In vitro* Cell Proliferation and ALP Activity ..... 94
3.5 Conclusion ..... 98

**Part III. Layered Double Hydroxide Based Nanohybrid as Diagnostic Agent ..... 99**

**Chapter 4. X-ray Visible Bioabsorbable Bone Fixation Plate *via* Various Layered Metal Hydroxides ..... 100**

4.1 Abstract ..... 102
4.2 Introduction ..... 106
4.3 Experimental Section ..... 107
4.3.1 Materials ..... 107
4.3.2 Preparation of LMHs ..... 108
4.3.3 Preparation of Radiopaque Bone Plates ..... 108
4.3.4 Characterizations ..... 110
4.3.5 *In vitro* X-ray Visibility Test ..... 110
4.3.6 *In vitro* Cell Study ..... 111
4.3.7 *In vivo* Animal Study ..... 112
4.3.7.1 *In vivo* X-ray Visibility ..... 113
4.3.7.2 Histologic Evaluation ..... 114
4.3.8 Statistical Analysis ..... 114
4.4 Results and Discussion ..... 115
4.4.1 Structural and Element Analysis of LMHs ..... 115
4.4.2 Characterization of the Radiopaque LMH Sheets ..... 117
4.4.3 *In vitro* X-ray Visibility ..... 124

4.4.4 *In vitro* Cell Visibility .....128
4.4.5 *In vivo* X-ray Visibility .....131
4.4.6 *In vivo* Histological Analysis .....135
4.5 Conclusion .....137

Part IV. Layered Double Hydroxide Based Nanohybrid as Theranostic Agent .....138
Chapter 5. Theranostic Bioabsorbable Bone Fixation Plate with Drug-Layered Double Hydroxide Nanohybrids .....139
5.1 Abstract .....139
5.2 Introduction .....141
5.3 Experimental Section .....144
5.3.1 Materials .....144
5.3.2 Preparation of Pristine LDH and RS-LDH .....145
5.3.3 Preparation of Functional Bone Plates .....145
5.3.4 Characterizations .....149
5.3.5 Measurement of Drug-Loading Amount .....149
5.3.6 *In vitro* Cell Study .....150
5.3.6.1 Cell Culture .....150
5.3.6.2 Cell Proliferation Study .....151
5.3.6.3 Alkaline Phosphatase (ALP) Activity .....152
5.3.7 *In vitro* Drug Release Study .....152
5.3.8 *In vitro* X-ray Visibility Test .....153
5.3.9 *In vivo* Animal Study .....153
5.3.9.1 *In vivo* X-ray Visibility Test .....154

5.3.9.2 *In vivo* μCT Analysis .....155
5.3.9.3 Histologic and Histomorphometric Evaluation .156
5.3.10 Statistical Analysis .....156
5.4 Results and Discussion .....157
5.4.1 Particle Analysis .....157
5.4.2 *In vitro* Proliferation and ALP Activity .....165
5.4.3 Analysis of Theranostic Plates.....167
5.4.4 *In vitro* Drug Release Study.....169
5.4.5 *In vitro* X-ray Visibility.....171
5.4.6 *In vivo* X-ray Visibility.....173
5.4.7 *In vivo* New Bone Formation.....174
5.4.8 Biocompatibility Evaluation.....176
5.5 Conclusion .....180

**Part V. Conclusion ..... 181**

**Chapter 6. Conclusion and Perspectives ..... 182**

**References ..... 187**

**Abstract in Korean ..... 198**

**Acknowledgement..... 200**

**Appendix ..... 204**

# List of Tables

Table 2.1 Components for transdermal drug delivery formulation. .....23

Table 2.2 Chemical compositions of the pristine LDH and FB-LDH. .....45

Table 3.1 Evaluated rate constants and $r^2$ coefficients based on the kinetic models. .....86

# List of Figures

Figure 1.1 Schematic crystal structure of layered double hydroxides (LDHs).....9

Figure 1.2 Synthetic routes to LDH based nanohybrids. (A) Co-precipitation, (B) ion-exchange reaction, (C), calcination-reconstruction, and (D) exfoliation-reassembling (reproduced from reference 18).....13

Figure 2.1 PXRD patterns of the (a) intact FB, (b) pristine LDH and (c) FB-LDH.....32

Figure 2.2 Longitudinal and lateral dimensions of FB molecule. 33

Figure 2.3 1D electron density projection along c-axis for the FB-LDH and the corresponding structural model. The solid and dashed lines show the curves of observed and calculated electron density projection, respectively. 36

Figure 2.4 1D electron density projections along c-axis for the FB-LDH and the corresponding two different structural models. The solid and dashed lines show the curves of observed and calculated electron density projection, respectively. .....35

Figure 2.5 FT-IR spectra of the (a) intact FB, (b) pristine LDH and (c) FB-LDH.....37

Figure 2.6 Particle analyses of the FB-LDH, showing (a) SEM image, (b) TEM image, (c) selected-area electron diffraction pattern, (d) cross-section TEM image with inlet of higher magnification, (e) particle size distribution, and (e) zeta potential of the FB-LDH nanohybrid (5.25

mV) ..... 39
Figure 2.7 Zeta potentials of the pristine LDH (34.1 ± 1.4 mV) and FB–LDH nanohybrid (5.25 ± 0.17 mV) ..... 40
Figure 2.8 TGA–DTA curves of the (a) pristine LDH and (b) FB–LDH. The solid and dashed lines show the curves of TGA and DTA, respectively. ..... 43
Figure 2.9 PXRD patterns of ZnO, $Al_2O_3$, and spinel $ZnAl_2O_4$. ... 43
Figure 2.10 *In vitro* drug release profiles of the FB–LDH in pH 7.4 PBS (a) without Eudragit® S–100 and (b) with Eudragit® S–100. ..... 47
Figure 2.11 Phase separation was observed with the formulations with a mass ratio of Eudragit® S–100 aqueous solution, higher than 200 μl per g suspension. ..... 50
Figure 2.10 *In vitro* skin permeability profiles of (a) G–FN–0, (b) G–FN–50, (c) G–FN–100, and (d) G–FN–200 ..... 51
Figure 3.1 Chemical structures and dissociations of AL depending on the values of equilibrium dissociation constant (pKa) of AL. Molar fraction of AL calculated from its pKa values depending on pH. ..... 71
Figure 3.2 PXRD patterns of AL intercalated into (a) $Mg_2Al_CO_3$ LDH, (b) $Mg_2Al_NO_3$ LDH, and (c) $Zn_2Al_NO_3$ LDH nanohybrids. ..... 72
Figure 3.3 (A) PXRD patterns of (a) intact AL, (b) LDH–$NO_3$, and (c) AL–LDH. (B) HR–TEM image of AL–LDH with inset of higher magnification. ..... 73
Figure 3.4 (A) Chemical structure and (B) 3–dimensional chemical structure of AL. (C) Schematic diagram of AL molecules intercalated in the LDH layer *via* intercalative ion–

exchange reaction. .....74
Figure 3.5 (A–C) Structural models for the AL–LDH along c–axis. (D) The relative X–ray intensity ($I_{rel}$) of the observed and calculated X–ray intensity of AL–LDH. .....75
Figure 3.6 FT–IR spectra of (a) intact AL, (b) LDH–NO3, and (c) AL–LDH.....77
Figure 3.7 Particle analyses; FE–SEM images of (a) LDH–$NO_3$ and (b) AL–LDH. (c) Particle size distributions and (d) zeta potentials of LDH–$NO_3$ (solid line) and AL–LDH (dashed line), respectively.....79
Figure 3.8 (A) Absorption spectra of (I) base line ($HClO_4$), (II) AL only, (III) AL–LDH only, (IV) standard $Fe^{3+}$ only, (V–XI) $Fe^{3+}$–AL complexes with different concentrations of AL, and (XII) $Fe^{3+}$–AL–LDH complex in 2.0 M $HClO_4$. (B) Absorbances of $Fe^{3+}$–AL complexes depending on the concentration of AL measured at 300 nm using UV–Vis spectroscopy.....81
Figure 3.9 *In vitro* cumulative AL release profile of AL–LDH in pH 7.4 PBS.....84
Figure 3.10 The plots of each kinetic equation based on (A) $1^{st}$ order rate model, (B) parabolic diffusion model, (C) Freundlich model, and (D) Elovich model for the release of AL from the AL–LDH at pH 7.4 PBS media.....86
Figure 3.11 Cellular accumulation of AL molecules in MG63 cells treated with either AL (■) or AL–LDH (●).....90
Figure 3.12 PXRD patterns of (a) LDH–$CO_3$ and (b) FITC–LDH–$CO_3$. .....91
Figure 3.13 Particle analyses; FE–SEM images of (A) LDH–$CO_3$ and

(B) FITC−LDH−$CO_3$. (C) Particle size distributions and (D) zeta potentials of LDH−$CO_3$ (solid line) and FITC−LDH−$CO_3$ (dashed line), respectively. The scale bars are 200 nm. .....92

Figure 3.14 Confocal microscopic images of MG63 cells treated with (A) 20 μg/ml FITC−LDH−$CO_3$, (B) supernatant solution of 20 μg/ml FITC−LDH−$CO_3$, and (C) 20 μg/ml FITC.93

Figure 3.15 *In vitro* proliferation of MG63 cells treated with osteogenic media containing different concentrations of LDH−$NO_3$, intact AL, and AL−LDH for (A) 2, (B) 3, and (C) 4 days. All experiments were performed at least three times for statistics. *Intact AL or AL−LDH was significantly different from LDH−$NO_3$ ($p < 0.05$). **AL−LDH was significantly different from both LDH−$NO_3$ and intact AL ($p < 0.05$). .....96

Figure 3.16 *In vitro* alkaline phosphatase activity (ALP) activity of MG63 cells treated with osteogenic media containing different concentrations of LDH−$NO_3$, intact AL, and AL−LDH for (A) 2, (B) 3, and (C) 4 days. All experiments were performed at least three times for statistics. *Intact AL or AL−LDH was significantly different from both negative control and LDH−$NO_3$ ($p < 0.05$). **AL−LDH was significantly different from the other groups ($p < 0.05$). .....97

Figure 4.1 (A) PXRD patterns of (a) CaFe−HC, (b) MgAl−LDH, (c) ZnAl−LDH, and (d) Zn−HDS. .....116

Figure 4.2 TGA curves of (a) PLGA, (b) LMH sheet, and (c) LMH of (A) CaFe−HC, (B) MgAl−LDH, (C) ZnAl−LDH, and

(D) Zn–HDS. .....119
Figure 4.3 (A) Optical image of a whole Inion bone plate. (B) Optical images of the 6.5 mm × 6.5 mm square–shaped piece of the plate (a) without and with a radiopaque (b) CaFe–HC, (c) MgAl–LDH, (d) ZnAl–LDH, and (e) Zn–HDS sheet. Scale bar represents 5.0 mm.....120
Figure 4.4 FE–SEM images of (A) CaFe–HC, (B) MgAl–LDH, (C) ZnAl–LDH, and (D) Zn–HDS sheet with inset of higher magnification. .....121
Figure 4.5 PXRD patterns of (a) PLGA, (b) LMH sheet, and (c) LMH of (A) CaFe–HC, (B) MgAl–LDH, (C) ZnAl–LDH, and (D) Zn–HDS. .....122
Figure 4.6 FTIR spectra of (a) PLGA, (b) LMH sheet, and (c) LMH of (A) CaFe–HC, (B) MgAl–LDH, (C) ZnAl–LDH, and (D) Zn–HDS. .....123
Figure 4.7 (A) Representative *in vitro* X–ray images and (B) densitometry measurements of the CaFe–HC_P, (b) MgAl–LDH_P, (c) ZnAl–LDH_P, and (d) Zn–HDS_P for a period of 28 days. *The CaFe–HC_P was statistically significantly different from MgAl–LDH_P ($p < 0.05$). **The ZnAl–LDH_P was statistically significantly different from both CaFe–HC_P and MgAl–LDH_P ($p < 0.05$). ***The Zn–HDS_P was statistically significantly different from all other radiopaque plates ($p < 0.05$). .....126
Figure 4.8 The theoretically calculated solubility diagrams of metal hydroxides depending on pH values. .....127
Figure 4.9 *In vitro* cell viability of of L929 cells treated with (A) the

powder of LMH and (B) the collected extract medium from the immersion medium where the radiopaque plates were each immersed in the cell culture medium at 37℃ for 42 days. The immersion medium was withdrawn to give the extract medium and an equal volume of the fresh medium was added back every 2 days. *The ZnAl-LDH was significantly different from both CaFe-HC and MgAl-LDH ($p < 0.05$). **The Zn-HDS_P was significantly different from all other LMHs ($p < 0.05$). .....130

Figure 4.10 (A) Representative *in vivo* X-ray images and (B) densitometry measurements of the (a) MgAl-LDH_P, (b) ZnAl-LDH_P, and (c) Zn-HDS_P inserted on subcutaneous tissue in rats for a period of 42 days. *The ZnAl-LDH_P was significantly different from MgAl-LDH_P ($p < 0.05$). **The Zn-HDS_P was significantly different from both MgAl-LDH_P and ZnAl-LDH_P ($p < 0.05$).....133

Figure 4.11 Representative *in vivo* X-ray images of the CaFe-HC_P inserted on subcutaneous tissue in rats at (A) day 0, (B) day 1, and (C) day 3. .....134

Figure 4.12 Histological images from the tissues around surgical area obtained at 42 days after plate implantation of (A) UP, (B) MgAl-LDH_P, (C) ZnAl-LDH_P, and (D) Zn-HDS_P. .....136

Figure 5.1 Optical image of a whole Inion bone plate (PLT-1031). To prepare the experimental samples, I cut a whole plate into pieces, each of 6.5 mm x 6.5 mm square shape with

a screw hole at the center. The scale bar represents 1 cm. .....148

Figure 5.2 (A) PXRD patterns of (a) intact RS, (b) pristine LDH, and (c) RS–LDH. (B) HR–TEM image of RS–LDH with inset of higher magnification. FE–SEM images of (C) pristine LDH and (D) RS–LDH. (E) Particle size distributions and (F) zeta potentials of the pristine LDH (dashed line) and RS–LDH (solid line). .....161

Figure 5.3 (A) Molcular dimension of RS and (B–D) structural models of the RS–LDH along the crystallographic c–axis. (E) The relative X–ray intensity ($I_{rel}$) of observed intensity ($I_{obs}$) obtained from PXRD of the RS–LDH and calculated intensity ($I_{cal}$) corresponding to three different structural models of RS–LDH. .....162

Figure 5.4 (A) Chemical structures and dissociations of RS depending on the values of equilibrium dissociation constant (pKa) of RS. (B) Speciation curves calculated from the pKa values of RS. The theoretical contents of RS intercalated in RS–LDH was 22.5 wt%. Briefly, it was determined on the basis of the net charge of RS (−3.53) calculated by its mole fractions ($RS^{3-}$ = 0.47 and $RS^{4-}$ = 0.53) at pH = 10.5, in which RS–LDH was formed during ion exchange reaction. .....163

Figure 5.5 FT–IR spectra of (a) intact RS, (b) pristine LDH, and (c) RS–LDH. .....164

Figure 5.6 (A) *In vitro* proliferation and (B) ALP activity of MG63 cells treated with osteogenic media containing different concentrations of the pristine LDH, intact RS, and RS–

LDH for 3 days. For each sample type, at least three experiments were performed for statistics. *Intact RS was significantly different from pristine LDH ($p < 0.05$). **RS-LDH was significantly different from both pristine LDH and intact RS ($p < 0.05$). .....166

Figure 5.7 Schematic process for preparation of a theranostic plate. (A) RS-LDH sheets were separately prepared from the polydimethylsiloxane molds of square-shaped frame filled with a paste of RS-LDH and PLGA (5:1, w/w). (B) PLGA solution was sprayed on the surface of a bone plate and (C) the RS-LDH sheet was attached on top of it to finally give (D) a theranostic bone plate. (E) Optical images of the bioabsorbable bone fixation plates without and with a theranostic RS-LDH sheet. (F) FE-SEM image of the surface of a theranostic RS-LDH sheet. .....168

Figure 5.8 *In vitro* drug release profiles of the intact RS, RS-LDH, RS-LDH_P1, and RS-LDH_P2 in pH 7.4 PBS for 42 days. (B) *In vitro* drug release profiles plotted in amounts with the RS-LDH_P1 and RS-LDH_P2 in pH 7.4 PBS for 42 days. .....170

Figure 5.9 (A) Representative *in vitro* X-ray images and (B) densitometry measurements of the LDH_P2, RS-LDH_P1 and RS-LDH_P2 for a period of 42 days. *RS-LDH_P1 was significantly different from both LDH_P2 and RS-LDH_P2 ($p < 0.05$). .....172

Figure 5.10 (A) Representative *in vivo* X-ray images and (B) densitometry measurements of the UP, LDH_P2, RS-

LDH_P1, and RS-LDH_P2 implanted on a cranial bone defect in rats. The no treatment group was also imaged as control. *The RS-LDH_P1 group was significantly different from both LDH_P2 and RS-LDH_P2 groups ($p < 0.05$). .....177

Figure 5.11 (A) Representative *in vivo* μCT images and (B) new bone volume percent in cranial bone defects treated with the UP, LDH_P2, RS-LDH_P1, and RS-LDH_P2. The no treatment group was also imaged as control. *The RS-LDH_P1 group was significantly different from no treatment group ($p < 0.05$). **The RS-LDH_P2 group was significantly different from all other different groups ($p < 0.05$).....178

Figure 5.12 (A) Histological images from the tissues around the cranial bone defect obtained at 12 weeks after plate implantation. The arrows indicate the specific locations of new bone formation. The scale bars represent 100 μm. (B) Histomorphometric analysis on new bone formation in cranial defects of the animal groups with no treatment and the ones fixed with the UP, LDH_P2, RS-LDH_P1, and RS-LDH_P2 at 12 weeks after implantation. *The RS-LDH_P1 group was significantly different from the no treatment, UP, and LDH_P2 groups. ** The RS-LDH_P2 group was statistically different from all other different groups ($p < 0.05$). .....179

# Part I.

# General Introduction

# Chapter 1

# Introduction

## 1. 1 Research Backgrounds

Nanoparticles (NPs) have been widely used to combine more than one kind of diagnostic or therapeutic functions, which makes them promising multifunctional nanohybrids for various biomedical applications. The nanohybrid can be constructed by either organic materials such as liposome, polymeric micelle, and dendrimer [1−3], inorganic ones such as iron oxide, gold, and mesoporous silica , or organic−inorganic hybrid materials [4, 5]. In particular, inorganic nanomaterials have been intensively studied for several decades because of their high chemical or biological stability and easy modification for the diagnosis and therapy.

Among various inorganic nanoplatforms, layered double

hydroxide (LDH) has been suggested as a promising nanomaterial for diagnosis and therapy. In materials chemistry, the "intercalation" denotes a chemical process, the reversible inclusion or insertion of a guest molecule into compounds with two-dimensional (2D) layered structures such LDH in order to form a new heterostructured hybrid materials[6-13].

Since a LDH based bio-inorganic nanohybrid was proposed for the first time in 1999 by Choy's group[14, 15], many attempts have been made to not only lead to a paradigm shift in the research fields such as nano-engineering and nano-medicine but also develop a new multidisciplinary convergence science and technology and multifunctional nanohybrid systems. 2D bio-inorganic nanohybrids prepared *via* intercalation reaction, a soft chemistry approach, of bioactive guest species into LDHs make a breakthrough in drug delivery, diagnostics, therapeutics, and even theranostics.[9, 16-20]

A synthetic LDH in the form of hydrotalcite have been used as an antacid or antipepsin agent, whose pharmacodynamic effect can be described as relief for pain and disorders of indigestion and heartburn due to excessive amount of stomach acid by raising the local pH to above 3.5.[21] Commercially available product in form of chewable tablet includes 500 mg of hydrotalcite, which is the equivalent amount for a neutralization capacity of 13 mVal HCl.[21]

The recent studies on biomedical applications of LDH based nanohybrid have demonstrated their feasibility for storage, transport, and subsequent controlled release of bioactive molecules with

potential therapeutic functions in diseased environments.[7–9, 11, 13, 18, 22] These studies showed advantages of LDHs such as anion exchange capacity (AEC), variable chemical compositions, bio–compatibility, crystallization–dissolution characters, and host–guest interactions. Such hybrid systems have been prepared on the basis of four different synthetic strategies such as, co–precipitation, ion–exchange, calcination–reconstruction, and exfoliation–reassembling. The LDHs can play a role as a reservoir to stably protect chemical and biological integrity of bioactive molecules from severe physical, chemical, and biological environments arising from the change in parameters like temperature, light, moisture, pH, and enzyme.

It has been also proved that thus prepared LDH based nanohybrids could be used as delivery carrier systems, since they can easily be permeated inside the cells by reducing the electrostatic repulsion between anionic biomolecules in LDHs and negatively charged cell membrane giving rise to enhanced cellular transfection efficiency. Since LDHs are fairly insoluble in neutral and basic pH domains, but become soluble at low pH, one can intentionally recover drugs or biomolecules intercalated in LDHs by dissolving them in a weakly acidic medium like a cellular cytoplasm, and/or induce sustained release of guest molecules out of LDHs *via* ion–exchange reaction in electrolyte solution. Additionally, LDH can function as a radiopaque material because of the higher X–ray attenuation coefficients of di– and trivalent metals, such as Zn and Al, respectively, in LDH lattice.[23–25]

## 1. 2 Layered Double Hydroxide (LDH)

LDHs are promising functional biomaterials and have been extensively studied due to their scientific and technological importance. They are synthetic anionic clays, exemplified by the natural mineral hydrotalcite, whose structure is based on brucite-like layers. LDHs have tailored chemical characteristics from the various possible metal compositions and exchangeable interlayer anions. The metal cations occupy the centers of edge sharing octahedra, whose vertexes contain hydroxide ions that connect to form infinite two-dimensional layers. Isomorphous substitutions of the divalent ($M^{2+}$) cation in the brucite-like layers by trivalent ($M^{3+}$) cation give rise to have positively-charged metal hydroxide layers. In order to compensate the positive layer charge in LDH lattice, exchangeable anionic species should be simultaneously stabilized in the interlayer space of LDHs, which can be then further exchanged with other anionic species like atomic ions to molecular clusters and even supramolecular anions. Hence, within the LDH crystal, the positively-charged brucite-like layers ($[M^{2+}_{1-x}M^{3+}_{x}(OH)_2]^{x+}$), are bound together by interlayer counter-anions and water molecules ($[A^{n-}]_{x/n}\cdot mH_2O$).[20, 21] Their general chemical formula can be described as; $[M^{2+}_{1-x}M^{3+}_{x}(OH)_2][A^{n-}]_{x/n}\cdot mH_2O$ (stoichiometric coefficient; x = 0.2 – 0.4; n = 0.5 – 1), where $M^{2+}$ may be common; $Mg^{2+}$, $Ca^{2+}$, $Ni^{2+}$, $Zn^{2+}$, $Fe^{2+}$, $Co^{2+}$, $Cu^{2+}$, or $Mn^{2+}$ and $M^{3+}$ may be common $Al^{3+}$, $Ga^{3+}$, $Mn^{3+}$, $Fe^{3+}$ or $Cr^{3+}$. $A^{n-}$ is a non-framework charge compensating inorganic or organic anion. Interlayer anions in

LDH are exchangeable, with the order of preference being, for example, $NO_3^-$ < $Br^-$ < $Cl^-$ < $F^-$ < $OH^-$ < $SO_4^{2-}$ < $HPO_4^{2-}$ < $CO_3^{2-}$, which is the consequence of hydrogen bonding and charge density. The electrostatic interactions and hydrogen bonds between layers and contents of the gallery hold the layers together, forming a three-dimensional structure, as shown in Figure 1.1.

The flexibility in a variety of possible chemical compositions is one of the most attractive features to allow functional LDHs with a wide variety of properties. Thus, chemistry of LDHs is now widely studied and this is in part driven by the use of these materials as precursors for preparing $CO_2$ adsorbents, catalysts, or directly as ion exchange hosts, fire retardant additives, polymer/LDH nanocomposites, and as cement additives. In particular, they have been extensively researched and applied to biomedical field, which include use as a pharmaceutics ingredient, drug or gene delivery carrier, diagnosis agent, and theranostic material. The variety of possible compositions enables the combination of various biocompatible elements in LDHs, with the lattice designs having controllable solubility in water. For example, LDHs with Mg/Al metal hydroxides are inert in the physiological condition of pH ~ 7.4, but dissolve in slightly acidic conditions such as in endosome (pH 5.5 – 6.0) and lysosome (pH 4.5 – 5.0) inside cells, which makes LDHs very interesting in terms of biological applications such as drug or gene reservoirs.

High AEC of LDH offers to intercalate various kinds of

negatively charged bioactive molecules in the interlayer space of LDHs, resulting in novel bio-inorganic nanohybrids.[15, 26-29] Since the intercalated anions can be chemically stabilized with LDH lattice by electrostatic interactions and hydrogen bonding, they could be controllably released out of the inorganic lattice, which is paramount importance to maintain pharmacologically active drug levels for long periods and avoiding repeated drug administration.

The positive surface charge of LDH, even after intercalation of anionic molecules into the LDH, enables easy approach and adhesion to inherently negatively charged cell membranes by electrostatic interactions without further chemical modifications.[30, 31] Most importantly, it has been known that LDH contributes to a high transportation efficiency of bioactive molecules through its unique cellular uptake mechanism, clathrin-mediated endocytosis.[32-34] Although, most inorganic nanoparticles require chemical and/or biological pre-modification(s) in order to obtain desirable properties for cellular delivery, such as good biocompatibility, suitable charge densities, cell targeting, suspension stability, and long circulation time, LDHs meet those requirements without any chemical modifications. As compared to other inorganic nano-vehicles, including silica and gold nanoparticles, quantum dots, and carbon nanotubes, LDH is highly advantageous due to its excellent biocompatibility[9, 35], high drug loading capacity[36, 37] and pH-responsive property[38-40] with biodegradability in the cellular cytoplasm[11, 31, 34], and therefore, applicable as an

efficient non-viral drug delivery vehicle and also as a reservoir for bioactive or bio-fragile molecules.

LDHs can work as a radiopaque materials since metal hydroxide layers of LDHs contain di- and trivalent metals with high X-ray attenuation coefficients such as magnesium (0.1686 $cm^2/g$), aluminum (0.1704 $cm^2/g$), calcium (0.2571 $cm^2/g$), iron (0.3717 $cm^2/g$), and zinc (0.4973 $cm^2/g$).

All these properties of LDH, such as high chemical versatility, anionic exchange capacity, controlled release property, efficient intracellular permeability, and radiopaque property, are leading to a promising future in biomedical field, opening up wide possibilities for researches and development for its clinical application.

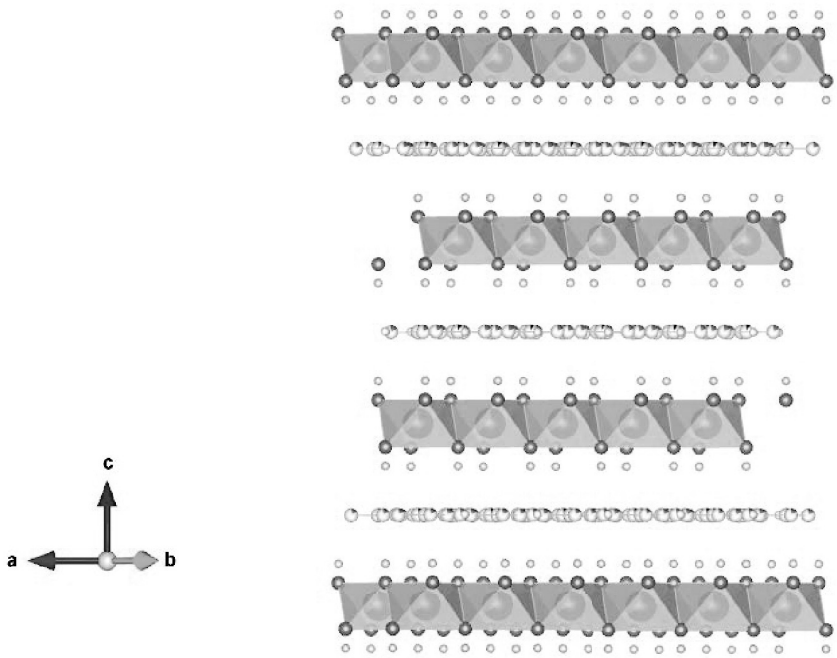


Figure 1.1. Schematic crystal structure of layered double hydroxides (LDHs)

## 1. 3 Synthetic Routes for LDH based Nanohybrids

Recently, the intercalative LDH-based nanohybrid with unique 2D nature in terms of crystal structure have received substantial attentions because of their extraordinarily high synergetic effects and complementary behaviours resulting from nanohydridization.[6, 8, 18] There are various synthetic routes for preparing functional LDH based nanohybrids: co-precipitation, ion-exchange, calcination-reconstruction, exfoliation-reassembling methods, as shown in Figure 1.2. The chemical driving forces to form LDH based nanohybrids would be an electrostatic interaction, coordination bonding, and/or van der Waals interaction at interface between host lattice planes and guest species.

The coprecipitation method is a simple and economic way for the one-pot synthesis of LDH based nanohybrids. The formation of 2D framework of LDH is made by base titration of aqueous solution containing $M^{2+}/M^{3+}$ metal precursors and anionic biomolecules that is to be directly intercalated into the LDH. The pH of a solution is adjusted at their coprecipitation region of mixed metal hydroxides of $[M^{2+}_{1-x}M^{3+}_{x}(OH)_2]^{x+}$, where the functional group of guest molecules are also deprotonated. However it is not always applicable, if the bioactive species are unstable in basic condition or directly interact with metal cations to form a coordinative dative bonding. Thus, alternative post-synthetic intercalative routes to form LDH based nanohybrid have been suggested such as ion exchange reaction, calcination-reconstruction one, and exfoliation-reassembling one.

The ion-exchange reaction to LDH based nanohybrids is the most widely introduced by replacing preoccupied anions within interlayer space of host with desired guest species. In order to prepare LDH based nanohybrids *via* ion exchange reactions, at first, the pristine LDHs are prepared with exchangeable anions, such as nitrate and chloride, and then ion exchange reaction is carried out by adding desired anionic guest species to a suspension of the pristine LDHs, in which a driving force is concentration gradient of guest molecules. Such ion-exchange reaction can be affected by chemical compositions of a pristine LDH influencing charge density, charge distribution, and hydration state, as well as a molecular dimension of guest component.

The formation of LDH based nanohybrids can be realized by calcination-reconstruction route, an unique method found in LDH based compounds, thanks to the structural memory effect of LDHs. In the process of calcination at around 400-500℃, the interlayer water, interlayer anions and the hydroxyl groups of the prepared pristine LDHs were completely decomposed, resulting in a mixed metal oxide with a formula $[M^{2+}_{1-x}M^{3+}_{x}O_{1+0.5x}]$. The calcined LDH, a mixed metal oxide, has potential to reversibly return to the layered structure of LDH by rehydrating the meta-phase, which can be referred to as "memory effect". Based on the memory effect, therefore, LDH based nanohybrid can be readily and simultaneously formed upon rehydration reaction of the mixed metal oxide in the presence of a desired anionic guest species. This kind of engineering

route to prepare LDH based nanohybrid is usually employed for large guest species to be intercalated into LDH.

The exfoliation-reassembling technique has been also used for the encapsulation of bulky and large-sized biomolecules or biopolymers. LDH based nanohybrids can be prepared by exfoliating the LDH into nanosheets, and reassembled into the pristine LDHs, when the positively charged LDH sheets and negatively charged biomolecules were coexisting in an aqueous solution as in the case of reconstruction route. Since the exfoliated LDH nanosheets commonly can be reassembled to form a wide range of LDH based nanohybrids with 2-dimensional layer-by-layer stacking structure, coreshell nanostructures, or hetero-multilayered thin films and membranes under mild condition.

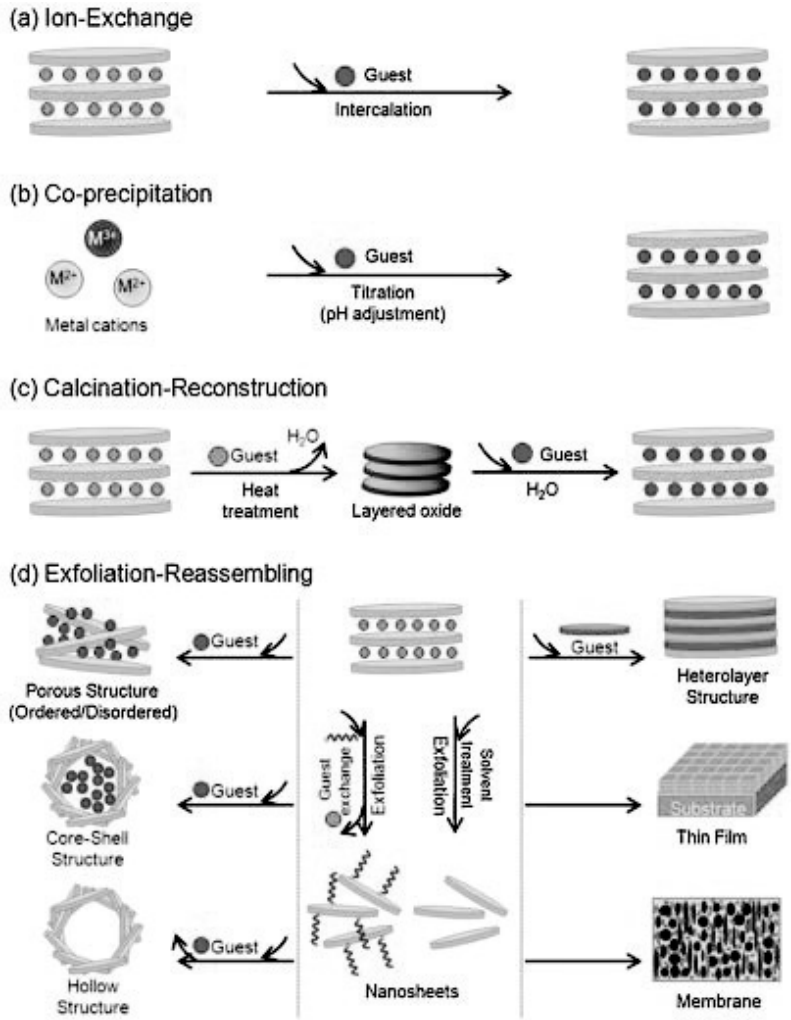


Figure 1.2. Synthetic routes to LDH based nanohybrids. (A) Co-precipitation, (B) ion-exchange reaction, (C), calcination-reconstruction, and (D) exfoliation-reassembling (reproduced from reference 18).

## 1. 4 Research Aims

In various biomedical engineering fields, I try to integrate engineering and medicine by combining the design and problem solving skills of engineering with medical and biological sciences in order to improve health care treatment, including diagnosis, monitoring, and therapy.[41] Nanoparticle-based diagnostic, therapeutic, and theranostic agents are emerging as a promising paradigm toward individualized nanomedicine for disease- and patient-specific diagnosis and therapy. I have developed several highly innovative diagnostic, therapeutic, and theranostic nano-platforms with LDH based nanohybrids in order to allow precise monitoring of disease, enhance therapeutic drug efficacy, and realize the integration of imaging and therapeutic functions into a single nano-formulation, respectively.

The major objective of this dissertation is to develop new LDH based nanohybrids for effective diagnosis and therapy, as well as both functionalities at a time. For therapeutic purpose, two features of LDH based nanohybrids—controlled/sustained drug release and high intracellular uptake efficacy-are used to enhance the treatment of diseases. For diagnostic purpose, LDH based nanohybrids with radiopaque property is used for developing a new type of X-ray visible bioabsorbable plate. The superior X-ray visibility of LDHs can be utilized to monitor after implantation. These LDH based nanohybrids represent a new generation of smart multifunctional nanomaterials for convenient integration of X-ray

imaging and therapeutic functions that simultaneously addresses the complex requirements of non-invasive X-ray imaging, effective therapeutic efficacy and the real-time *in vivo* drug delivery by a simple approach.

In Part II, I provide nonaqueous gel suspension of flurbiprofen (FB), a transdermal model drug, intercalated LDH nanohybrid, in which amount of the water including an anionic macromolecule, Eudragit® S-100, was added to control transdermal drug delivery. Also, an attempt has been made to enhance the intracellular uptake efficacy of alendronate (AL), an anti-resorptive and bone-remodeling drug, by encapsulating it into the LDH as drug delivery vehicle, to form a nanohybrid (i.e., AL-LDH) with two-dimensional heterostructure. Once a drug of interest is encapsulated in the LDH, the extent and period of activity of the drug can be controlled and drug efficacy can be improved, hence resulting in enhanced therapeutic effect.

In Part III, I employ biodegradable and biocompatible layered metal hydroxides (LMHs) as alternative radiopaque materials in order to develop bioabsorbable polymeric plate enabled with diagnostic advantages (i.e., X-ray imaging), which is highly desirable for post-operative diagnosis. I separately prepared radiopaque sheets made of a blend of poly(lactic-co-glycolic acid) (PLGA) and radiopaque LMHs, and then attached onto top of bioabsorbable plate. It is expected that di- and trivalent metals with higher X-ray attenuation coefficients, such as magnesium (0.1686 $cm^2/g$),

aluminum (0.1704 $cm^2/g$), calcium (0.2571 $cm^2/g$), iron (0.3717 $cm^2/g$), and zinc (0.4973 $cm^2/g$), located in LMH lattice than carbon (0.1514 $cm^2/g$), the main source of bioabsorbable polymeric plate, would give X-ray diagnostic functionality to the plate. The degree of X-ray visibility can be also modulated depending on the metal compositions of LMHs.

In Part IV, I propose a bioabsorbable bone plate enabled with dual functionalities of both diagnostic and therapeutic abilities. For this purpose, I employ a drug intercalated layered double hydroxide (LDH) nanohybrid as a theranostic agent to be integrated with a bioabsorbable bone fixation device in clinical use. For the first time to our knowledge, I proposed a combined entity of a bioabsorbable bone plate and the LDH based nanohybrid to be enabled with both X-ray imaging and sustained, local drug release for expedited bone repair.

Therefore, in this thesis, new LDH based nanohybrid systems have been developed for utilization in various biomedical applications, such as drug delivery, diagnostics, therapeutics, and even theranostics. The prepared LDH based nanohybrids showed noticeably high drug efficacy due to controlled/sustained drug release behavior and enhanced cellular uptake behavior based on clathrin-mediated endocytosis.[42-45] Moreover, the di-and trivalent metals in LDH based nanohybrids give radiopaque property. It is, therefore, theranostic system with LDH based nanohybrids could be realized by utilizing their diagnostic and therapeutic functionality together.

# Part II.

# Layered Double Hydroxide Based Nanohybrid as Therapeutic Agent

# Chapter 2

## Drug-Inorganic-Polymer Nanohybrid for Transdermal Delivery

### 2.1 Abstract

For transdermal drug delivery, I prepared a drug-inorganic nanohybrid (FB-LDH) by intercalating a transdermal model drug, flurbiprofen (FB), into the layered double hydroxides (LDH) *via* coprecipitaion reaction. The X-ray diffraction patterns and FT-IR

spectra of the FB-LDH indicated that the FB molecules were successfully intercalated via electrostatic interaction within the LDH lattices. The *in-vitro* drug release revealed that the Eudragit® S-100 in release media could facilitate the drug out-diffusion by effectively replacing the intercalated drug and also enlarging the lattice spacing of the FB-LDH. In this work, a hydrophobic gel suspension of the FB-LDH was suggested as a transdermal controlled delivery formulation, where the suspensions were mixed with varying amounts of Eudragit® S-100 aqueous solution. The Frantz diffusion cell experiments using mouse full-skins showed that a lag time and steady-state flux of the drug could be controlled from 12.8 h and 3.28 $\mu g\ cm^{-2}\ h^{-1}$ to less than 1 h and 14.57 $\mu g\ cm^{-2}\ h^{-1}$, respectively, by increasing the mass fraction of Eudragit® S-100 solution in gel suspensions from 0 to 20% w/w, respectively. Therefore, I conclude gel formulation of the FB-LDH have a potential for transdermal controlled drug delivery.

## 2.2 Introduction

Transdermal drug delivery system (TDDS) has gained a great deal of interest due to the advantages over conventional oral dosage forms, such as avoidance of hepatic first pass metabolism and gastrointestinal side effects, and less frequent administrations[42, 43]. TDDS has been developed in many different forms, such as ointment and patch, which mainly serve as a drug reservoir on the top of the skin to have drug molecules diffuse *via* the stratum corneum, a major permeation barrier, into the systemic circulation in a sustained manner [44, 45]. However, without controlled delivery, a massive flux of a drug from a reservoir into the skin could occur, which would be extremely problematic especially for the drugs with safety concerns [46]. Transdermal patches with drug-delivery membranes can control drug delivery to some extent, which, However, is still subject to be destroyed and its fabrication is known to be quite complicating [47].

Recently, layered materials have been regarded as useful inorganic macromolecules or building blocks to prepare various 2D heterostructures with desired functions in a wide range of applications [7, 8, 13, 48-51]. Extensive studies have been carried out on the layered nanomaterials incorporating a therapeutic agent to increase drug stability[15, 26, 52] and control drug release [40, 53], hence enhanced drug bioavailability [33, 38]. Among the inorganic layered nanomaterials, layered double hydroxides (LDHs) have been

widely studied as an efficient carrier of therapeutic agents. In this work, I propose the LDH-based nanohybrid for transdermal delivery formulation. I prepared the nanohybrids, employing flurbiprofen (FB) as a model drug (i.e., FB-LDH), where the anionic FB molecules were intercalated into the positively charged LDH layers by electrostatic interaction. FB, a non-steroidal anti-inflammatory drug, has been already approved in transdermal dosage forms [56-58].

For controlled delivery, I prepared a nonaqueous gel suspension of the FB-LDH, where a varying amount of the water including an anionic macromolecule, Eudragit® S-100, was added. Thus, four different gel suspensions were prepared in this work by mixing 0, 50, 100 and 200 μl of an aqueous solution of Eudragit® S-100 (2.5 w/v%) with 1 g of the FB-LDH gel suspension, respectively. The macromolecules, possessing the same polarity as the intercalated compounds, are known to facilitate the out-diffusion of intercalated compounds by enlarging the lattice spacing of nanohybrid [38, 59]. Therefore, the strategy is following: 1) the drug is released from the FB-LDH in a gel medium and 2) drug in a gel medium is then permeated *via* the skin. The former is tailored by the amount of an aqueous solution of Eudragit® S-100 present in a gel and the latter by the drug concentration in a gel medium. FB is a poorly soluble (< 8 $\mu$g/ml) and thus, most of the drug is expected to distribute in a hydrophobic gel medium when released from the FB-LDH.

## 2.3 Experimental Section

### 2.3.1 Materials

$ZnCl_2$, $AlCl_3 \cdot 6H_2O$, flurbiprofen ($C_{15}H_{13}FO_2$), monopotassium phosphate and ethylcellulose were obtained from Sigma (St. Louis, MO, USA). Sodium hydroxide and ethanol (EtOH) were purchased from Daejung (Siheung, Korea). Anhydride acetic acid and acetonitrile, all in HPLC grade, were obtained from JT Baker (NJ, USA). Eudragit® S-100 was purchased from Degussa (Essen, Germany). Labrafac® CC, Labrafil® M 1944 CS, and Transcutol® P purchased from Gattefosse (Lyon, France) were utilized to prepare the gel medium (Table 2.1).

Table 2.1. Components for transdermal drug delivery formulations

| Component | | Chemical formula | Structural formula |
|---|---|---|---|
| Flurbiprofen | | $C_{15}H_{13}FO_2$ | 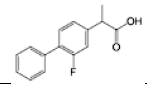 |
| Ethyl cellulose | | $C_{20}H_{38}O_{11}$ | 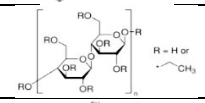 |
| Eudragit® S-100 | | $C_9H_{14}O_3$ | 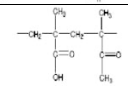 |
| Labrafac® CC (Caprylic/Capric Triglyceride) | | $C_{21}H_{44}O_7$ | 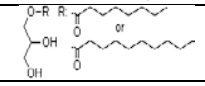 |
| Labrafil® M 1944 CS, (Unsaturated polyglycolysed glycerides) | Mono glycerides | $C_3H_6(OR)(OH)_2$ | 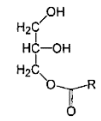 |
| | Diglycerides | $C_3H_6(OR)_2(OH)$ | 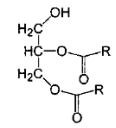 |
| | Triglycerides | $C_3H_6(OR)_3$ | 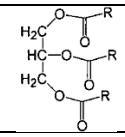 |
| | Monofatty esters of polyethylene glycol 300 | $(C_2H_4O)_6(OR)(OH)$ | 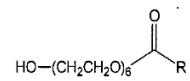 |
| | Difatty esters of polyethylene glycol 300 | $(C_2H_4O)_6(OR)_2$ | 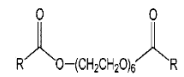 |
| Transcutol® P | | $C_6H_{14}O_3$ | 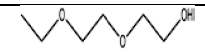 |

### 2.3.2 Preparation of FB-LDH Nanohybrid

A solution of 0.04 M FB in 15 ml EtOH and a solution of 0.08 M $ZnCl_2$ and 0.04 M $AlCl_3 \cdot 6H_2O$ (molar ratio of $M^{2+}/M^{3+}$ = 2) in 15 ml of deionized water were vigorously mixed for 30 min until the solution became transparent. After this, the solution was coprecipitated by titrating with 0.5 M NaOH solution to pH 8, and aged at room temperature for 12 h. All the reaction was carried out under nitrogen atmosphere to prevent carbonate contamination from air. The resulting FB-LDH precipitate was separated by centrifugation and washed three times with the mixed solution of EtOH and deionized water (1:1, v/v) to remove the unreacted salt ions and excess FB. A dry powder of the FB-LDH nanohybrid was obtained by freeze-drying.

### 2.3.3 Preparation of FB-LDH Gel Formulations

To prepared the gel formulation of the FB-LDH, the nanohybrids were suspended in a nonaqueous gel medium, which is already widely accepted for transdermal drug-delivery formulations [60, 61]. The gel medium was prepared by mixing Labrafac® CC and ethyl cellulose (49:6, w/w) with agitation at 90℃ until the mixture became transparent. After cooling down the resulting mixture to room temperature, Labrafil® M 1944, Transcutol® and the FB-LDH were added (Labrafil: Transcutol: FB-LDH: the mixture = 15: 20: 10: 55, weight ratio) and stirred at 90℃ to give a gel suspension of the FB-

LDH. Thus, all gel formulations prepared in this work contained 45 mg FB-LDH per g gel suspension.

In this work, I also added a varying amount of Eudragit® S-100 aqueous solution to the FB-LDH gel suspensions for controlled drug delivery: 0, 50, 100 and 200 μl of Eudragit® S-100 aqueous solution (2.5 wt%) into 1 g of the FB-LDH gel suspension to give G-FN-0, G-FN-50, G-FN-100 and G-FN-200, respectively.

### 2.3.4 Characterizations of FB-LDH Nanohybrid

#### 2.3.4.1 Powder X-ray Diffraction (PXRD)

The crystallinity of the FB-LDH was examined by an X-ray diffractometer (D/MAXRINT 2200-Ultima, Rigaku, Japan) equipped with Ni-filtered Cu-K$\alpha$ radiation ($\lambda$ = 1.5418 Å). The samples were loaded on a glass substrate holder and continuously scanned at the tube voltage and the current of 40 kV and 30 mA, respectively. To predict the interlayer structure of guest species in layered inorganic compounds, one-dimensional (1D) electron density was also calculated by eliminating certain conformational possibilities of guest species that are incompatible with the experimental X-ray diffraction data. The 1D electron densities along the z axis ($\rho(z)$) were calculated by using the following equation [62].

$$\rho(z) = \sum_{l=0}^{\infty} F_{00l} \cos\frac{2\pi lz}{c}$$

where c is the unit cell parameter of FB-LDH and $F_{00l}$ is the structure factors for the (00*l*) reflections, derived from their intensities corrected by Lorentz polarization factor. The signs of the structure factors were directly obtained from the scattering contributions of octahedral $Zn_2Al$ hydroxide layers, assuming that the contribution of incorporated molecule is relatively small. For the FB-LDH, six (*00l*) reflections were used.

#### 2.3.4.2 Fourier Transform Infrared (FT-IR)

FT-IR spectra of the intact FB, pristine LDH, and FB-LDH were collected with a JASCO 6100 spectrophotometer (JASCO, Inc., Japan) in a range of 400 - 4000 $cm^{-1}$ with 4 $cm^{-1}$ resolution, using the KBr disk method.

#### 2.3.4.3 Scanning Electron Microscopy (SEM)

The field emission scanning electron microscopic image of the FB-LDH was monitored with JEOL JSM-6700F (JEOL Ltd., Japan). The sample was coated with platinum before imaging.

#### 2.3.4.4 Transmission Electron Microscopy (TEM)

The transmission electron microscopic image of the FB-LDH was obtained on JEOL JEM-2000EXII (JEOL Ltd., Japan) at 200 kV of an accelerating voltage. To prepare a TEM sample, the FB-LDH

was suspended in deionized water, a drop of which was placed on a Cu grid coated with carbon and dried. To obtain the cross-sectional image, the FB-LDH was embedded in an epoxy resin, which was ultramicrotomed (RMC, Tucson, USA) with 50 nm thickness without staining and placed on a Cu grid coated with carbon.

#### 2.3.4.5 Particle Size Distribution and Zeta Potential Measurements

The size distribution and surface charge of the pristine LDH and the FB-LDH in distilled water were measured with Malvern Zetasizer Nano ZS (Malvern, UK).

#### 2.3.4.6 Characterizations of FB-LDH Nanohybrid

The chemical compositions of the pristine LDH and FB-LDH were determined by the elemental CHN analyses with EA1110 (CE instrument, Italy) and inductive coupled plasma (ICP) analyses with Optima-4300 DV (PerkinElmer, USA).

#### 2.3.4.7 High Performance Liquid Chromatography (HPLC) Analysis

To evaluate the amount of FB incorporated in the FB-LDH, 45 mg FB-LDH was dispersed into 100 ml of the solution mixed with EtOH and pH 7.4 PBS (1:4, volume ratio), which was then sonicated for 30 min to completely extract the FB from the FB-LDH. The suspension was then filtered by a Nylon syringe filter with a pore

size of 0.45 $\mu$m (Millipore, USA). The chromatogram of the solution was obtained with the high performance liquid chromatography (HPLC) (Agilent 1100 series, Agilent Technologies, USA) equipped with a UV detector ($\lambda_{max}$ = 254) and reverse phase Zorbax® C18 column (25 cm × 0.45 cm, 5 $\mu$m, Agilent Technologies, USA). The mobile phase composed of anhydride acetic acid, acetonitrile and deionized water (1:7:12, volume ratio) was used with a flow rate and injection volume of 1.5 ml/min and 10 $\mu$l, respectively. The column temperature was maintained at 25℃.

### 2.3.5 *In vitro* Drug Release Test

*In vitro* release experiments were carried out using a dissolution apparatus 2, Vision® G2 Elite 8™ Dissolution Tester (Hanson, USA) with the paddle-type stirrer (50 rpm) based on a USP dissolution test method (USP, 2002a, pp. 2011-2012). Two distinct release media were employed, which were the pH 7.4 PBS solutions without and with Eudragit® S-100 (2.5% w/v), to examine the effect of anionic macromolecules on FB release. The FB-LDH (45 mg) was suspended in 900 ml of the release media at 37℃ and the amount of released FB was determined by monitoring the HPLC spectra at scheduled intervals.

### 2.3.6 *In vitro* Skin Permeability Test

The *in vitro* passive skin permeability of FB from the FB-

LDH was investigated by Franz diffusion cell diffusion method [63]. At first, fresh full skins were obtained from six-week-old female hairless nude mice (Orientbio, Korea). Only the mice without the signs of overt toxicity and readily apparent clinical symptoms were selected and sacrificed by cervival dislocation, from which the skins without any defect were collected. All experiments were conducted in compliance with the experimental protocol, which was approved by the Institutional Animal Care and Use Committee (IACUC) at the Ewha Womans University (IACUC No.: 2010-9-3).

The full skins thus obtained were each placed between the donor and acceptor chambers, where the stratum corneum and dermal side were exposed to the donor and receptor chambers, respectively. The receptor chamber was filled with pH 7.4 PBS, where the temperature was maintained at 37 ± 1℃ by the thermostatically controlled circulating water jacket. The exposed area of the skin membrane available for drug permeation was 1.76 $cm^2$ and the capacity of each receptor chamber was 12.5 ml. The gel formulations prepared in this work was each applied on top of the skin *via* the donor chamber. At scheduled intervals, the media in the receptor chamber was drawn out and the receptor was re-filled with an equal amount of fresh PBS. The sampled media were each assayed with the HPLC as described above. Each of the gel formulations was tested at least five times for statistics.

## 2.4 Results and Discussion

### 2.4.1 PXRD Analysis

To assess the formation of the nanohybrid prepared by the conventional coprecipitation method, I examined the PXRD pattern of the FB−LDH, together with the ones of intact FB and pristine LDH, as shown in Figure 2.1. The pristine LDH shows a series of well ordered (00*l*) reflections corresponding to the basal spacing of 7.5 Å, indicating the formation of the $Cl^-$ intercalated LDH while the FB−LDH shows the sharp and well developed (00*l*) reflections with an increase in basal spacing to 24.4 Å. This clearly demonstrated that the FB were well intercalated into the interlayer space of LDH lattice. From the thickness of the LDH layer and the basal spacing of the FB−LDH, the gallery height of the FB−LDH could be determined to be 19.6 Å, larger than the molecular dimensions of FB as shown in Figure 2.2. Therefore, it was expected that the FB molecules were likely to be stabilized in a tilted double layer arrangement.

To assess this configuration, I first examined the steric limitation between the intercalated FB molecules and charged sites of LDH layers [17]. The steric limitation in the interlayer of layered materials can be explained in the viewpoint of the equivalent area ($A_e$) (area per positive unit charge ($Å^2/e^-$) of a layered double hydroxide) and the area demand ($A_c$) (area demand per unit charge ($Å^2/e^-$) for intercalated single molecules). $A_e$ of the layered host lattices can be estimated from the equation, $A_e = a \cdot b \cdot \sin\gamma / 2\xi$, where *a* and *b* are

the lattice parameters and $\xi$ is the layer charge per formula unit [64]. Based on the lattice parameters of the FB-LDH ($a$ = $b$ = 3.07 Å, $c$ = 73.04 Å, $\gamma$ = 120° and $\xi$ = 1/3e$^-$), $A_e$ of the $Zn_2Al$ host layer and $A_c$ of a single FB molecule are about 12.2 Å$^2$ and 71.3 Å$^2$, respectively. As $A_c$ is larger than $2A_e$, the FB molecules in LDH were likely to have a tilted bilayer arrangement to avoid steric hindrance.

To get further insight into the interlayer arrangement of FB molecules, the 1D electron density map of the FB-LDH structure along the $c$ axis was constructed. Among various different structure models, the FB-LDH structure model in Figure 2.3, which has confidence with value of difference Fourier map ($\Delta\rho(z)$ = 0.98), was quite well consistent with the results of observed and calculated electron density projection compared to different models tilted from 0° to 31.55° (Figure 2.4). The 1D plot can be used to support a structural model for the interlayer space. The $\rho(z)$ values were obtained by Fourier transform of the intensities for well-developed (00$l$) reflection peaks. The 1D electron density map displayed two strong peaks at z = 0 and 1, corresponding to the metals present in the hydroxide layers. Between these two strong peaks, six additional peaks of lower electron densities were observed due to the intercalated FB molecules. Given this and upon comparison with the length of the FB molecule, I could again propose that FB in the LDH layer has an interdigitated bilayer arrangement with a tilt angle of ≈20.96° .

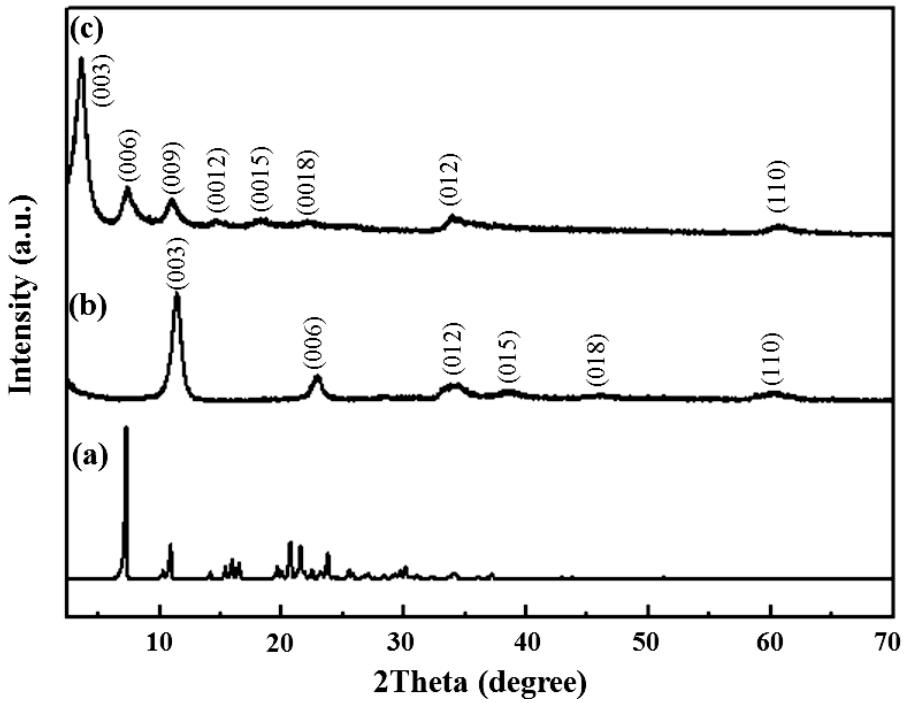


Figure 2.1. PXRD patterns of the (a) intact FB, (b) pristine LDH and (c) FB-LDH.

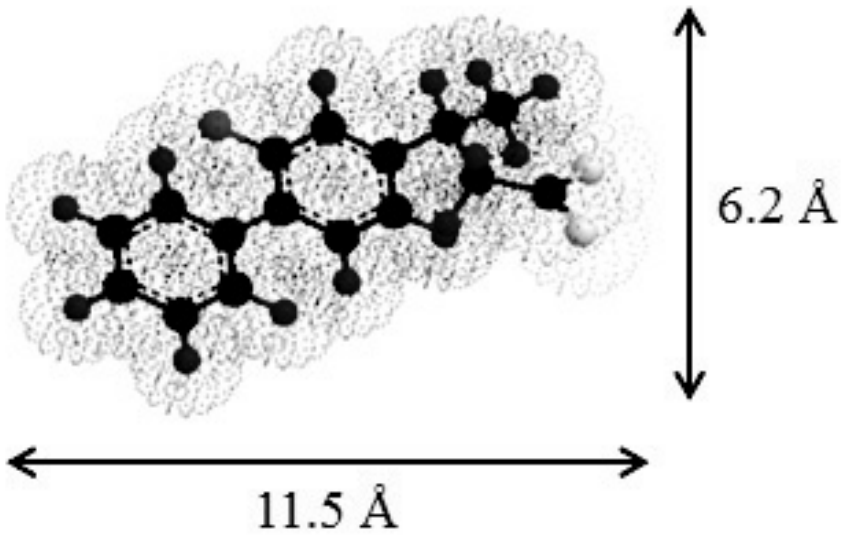


Figure 2.2. Longitudinal and lateral dimensions of FB molecule.

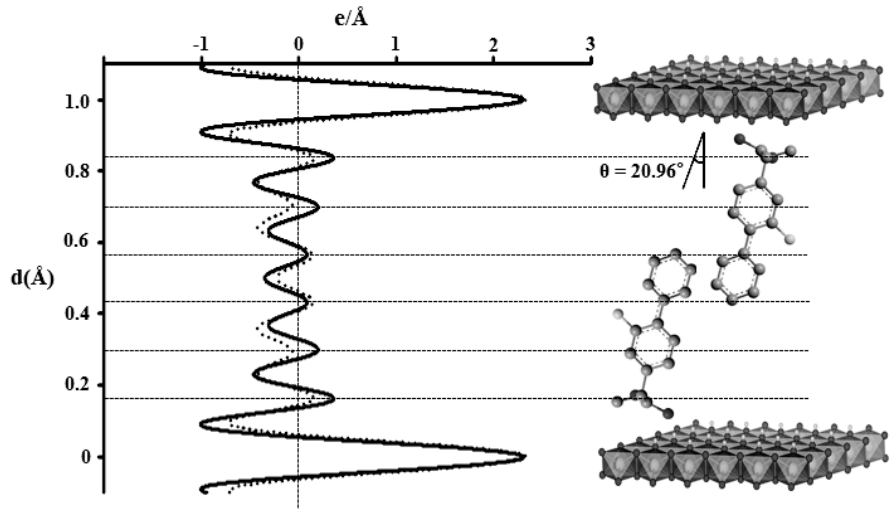


Figure 2.3. 1D electron density projection along c−axis for the FB−LDH and the corresponding structural model. The solid and dashed lines show the curves of observed and calculated electron density projection, respectively.

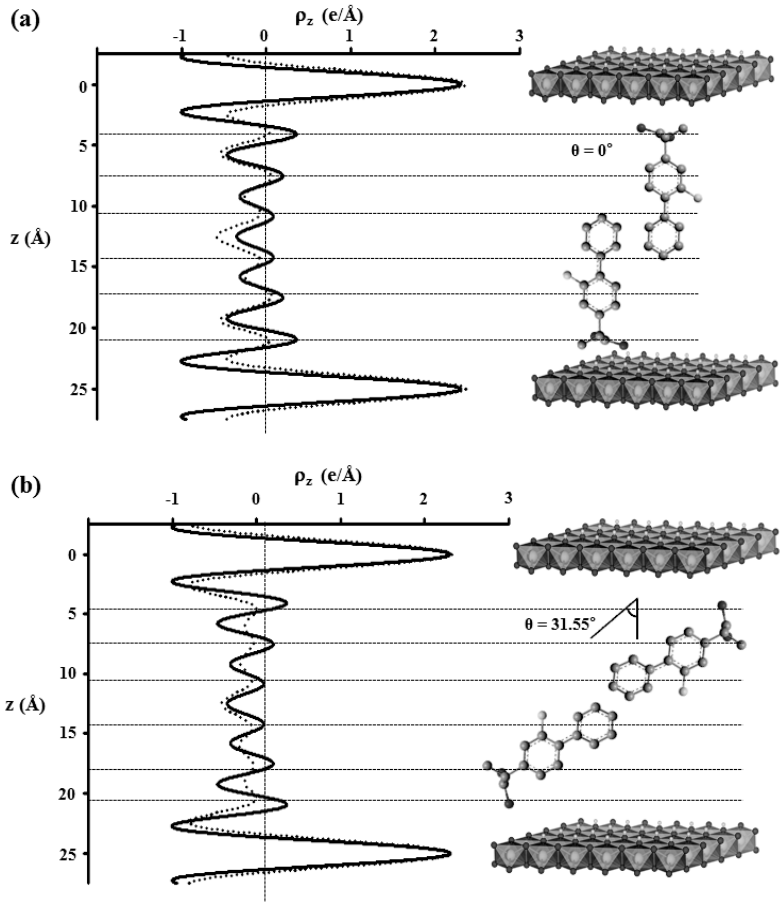


Figure 2.4. 1D electron density projections along c−axis for the FB−LDH and the corresponding two different structural models. The solid and dashed lines show the curves of observed and calculated electron density projection, respectively.

.

### 2.4.2 FT-IR Analysis

To examine the chemical interaction between FB molecules and LDH lattices, I compared the FT-IR spectra of the (a) intact FB, (b) pristine LDH, and (c) FB-LDH, as shown in Figure 2.5. In the spectra of intact FB, the characteristic peaks were observed at 1195 $cm^{-1}$ (C-F) and 1624 $cm^{-1}$ (C-C) due to stretching mode of aromatic ring. These characteristic peaks were superimposed on the spectra of the FB-LDH, indicating that the FB was intercalated into the LDH matrix without any noticeable structural changes. The notable feature upon the intercalation of the FB into LDH was disappearance of the absorption peak at 1698 $cm^{-1}$, and appearance of the new bands at 1550 and 1403 $cm^{-1}$. The former was ascribed to the carbonyl group (C=O) of the free carboxylic acid group in FB and the latter was due to asymmetric and symmetric modes of ($COO^-$), implying the deprotonated carboxylate form of FB molecules were bound to the interlayer of LDH lattice by electrostatic interaction [65]. The pristine LDH exhibited the broad absorption band at 3452 $cm^{-1}$ assigned to OH vibration and interlayer water. This broad band was also seen with the FB-LDH. The peak seen around at 1629 $cm^{-1}$ was assigned to the O-H stretching modes of interlayer water molecules of the pristine LDH. The absorption bands observed below 800 $cm^{-1}$ were associated with lattice vibration modes attributed to M-O and M-O-M vibration in the brucite layer, which were observed on both pristine LDH and FB-LDH.

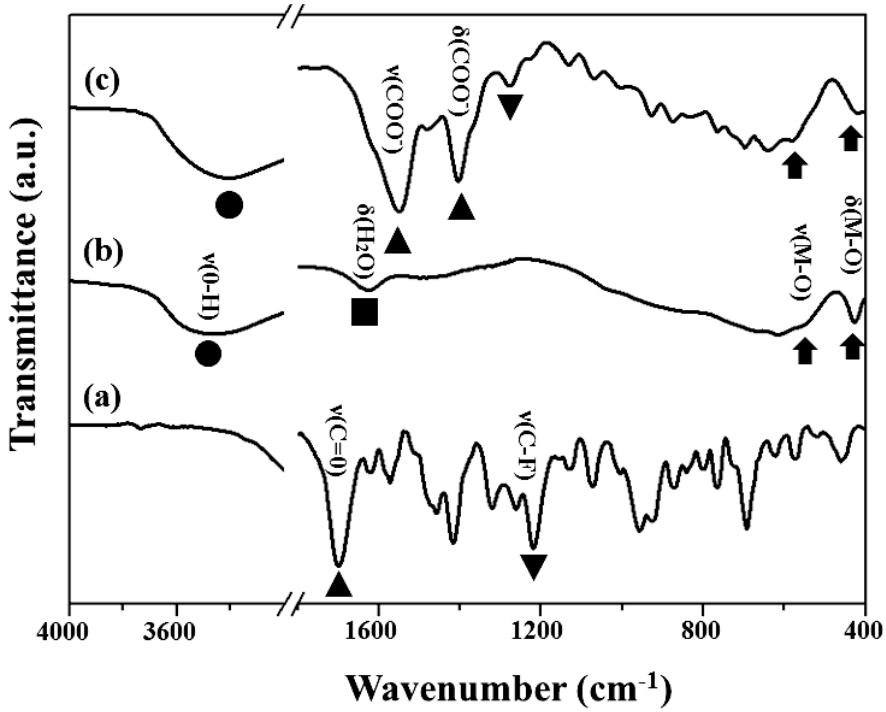


Figure 2.5. FT-IR spectra of the (a) intact FB, (b) pristine LDH and (c) FB-LDH.

### 2.4.3 Particle Analysis

The FB-LDH was observed with both SEM and TEM to assess their morphology and crystal structure. Figures 2.6(a-b) show that the FB-LDH possessed plate-like morphology with primary particle size of 105 nm. The selected-area electron diffraction (SAED) patterns of the FB-LDH displayed hexagonally arranged spots (Figure 2.6(c)). The corresponding calculated cell parameter ($a$ = 0.30 nm) were, within the error limit, identical to those obtained from the XRD analysis. The cross-sectional TEM image revealed that the FB-LDH was composed of the layered matrices with the basal spacing of 24.4 Å (Figure 2.6(d)), which was also in good agreement with the dimension estimated from the PXRD data.

I also examined the size distribution and surface charge of the FB-LDH based on the dynamic light scattering (DLS) and zeta potential methods, respectively. As shown in Figure 2.6(e), the FB-LDH exhibited an average size of 105 ± 13 nm, as obtained with the SEM and TEM data. The FB-LDH had a positive surface charge (zeta potential: + 5.25 ± 0.17 mV at pH 7.4) in Figure 2.6(f) due to the positively-charged nature of $Zn_2Al$ hydroxide layer. After intercalation of negatively-charged FB, the surface charge of the FB-LDH was lowered by charge compensation, as compared to the pristine $Zn_2Al$ LDH (Figure 2.7).

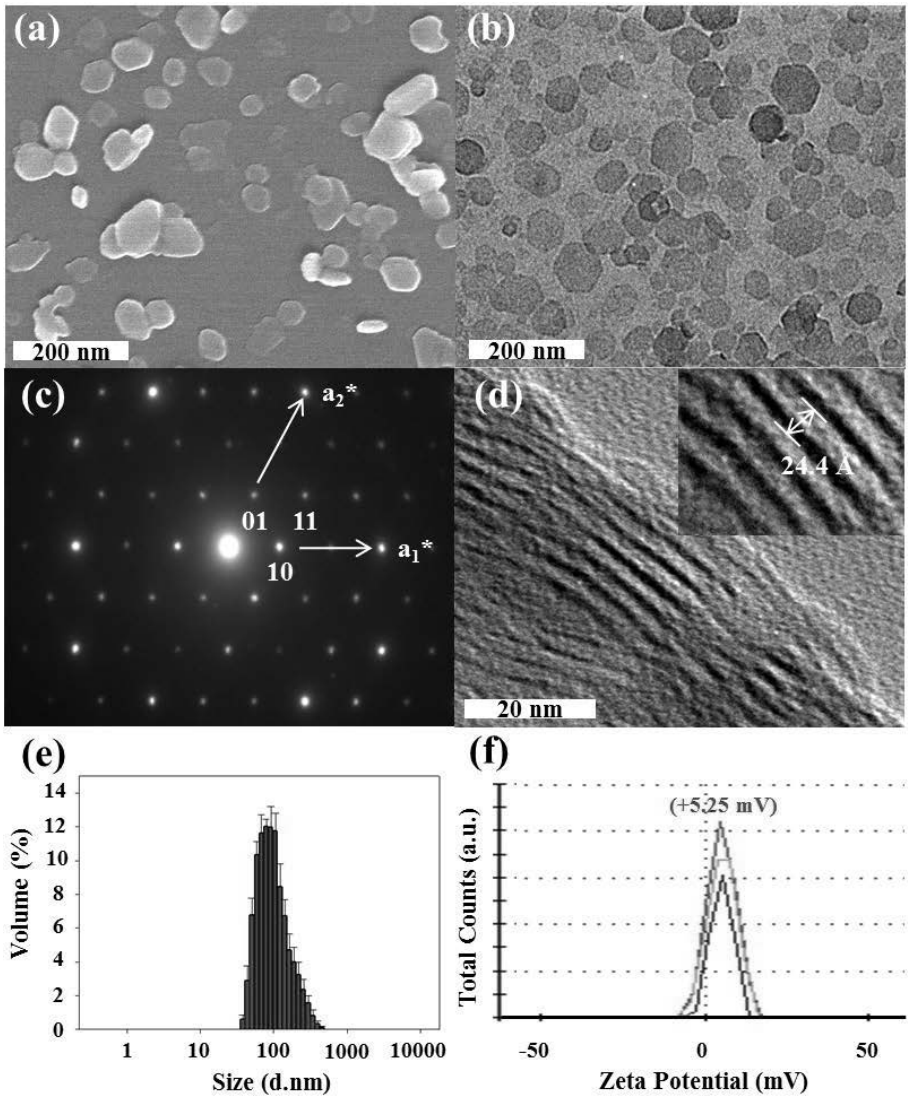


Figure 2.6. Particle analyses of the FB-LDH, showing (a) SEM image, (b) TEM image, (c) selected-area electron diffraction pattern, (d) cross-section TEM image with inlet of higher magnification, (e) particle size distribution, and (e) zeta potential of the FB-LDH nanohybrid (5.25 mV).

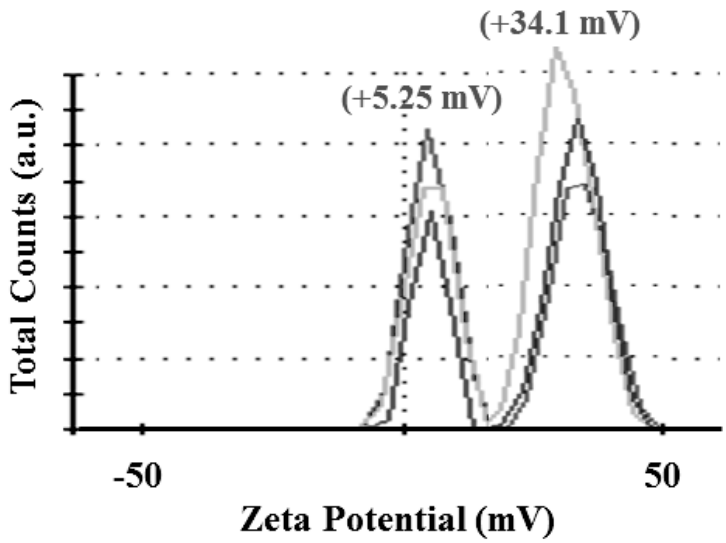


Figure 2.7. Zeta potentials of the pristine LDH (34.1 ± 1.4 mV) and FB−LDH nanohybrid (5.25 ± 0.17 mV).

### 2.4.4 Thermal Analysis

I performed the TGA-DTA on the dry powder of the pristine LDH and FB-LDH. In the TGA-DTA curve for the pristine LDH (Figure 2.8(a)), the first weight loss (ca. 13.1%) with an endothermic peak at 135.9℃ was attributed to the dehydration of physically absorbed water molecules located both at the exterior surface and in the interlayer space of the LDH particles (30.0 - 232.8℃). A second mass loss (ca. 24.1%) with an endothermic peak centered at 363.19℃ is related to partial dehydroxylation of the brucite-type layers (232.8 - 493.4℃). Still, the third weight loss (ca. 4.8%) was observed above 493.4℃, which is attributed to the carbonate decomposition and elimination of chloride species [66]. For the FB-LDH, the TGA-DTA curves show the thermal evolution with three consecutive stages due to dehydration, decomposition, and dehydroxylation, respectively (Figure 2.8(b)).

The first weight loss (ca. 6.51%) with a weak endothermic response around at 71.9℃ was ascribed to removal of absorbed water on the surface of the FB-LDH, which was smaller than that with the pristine LDH because of the presence of intercalated hydrophobic FB. The second weight loss (ca. 8.03%) with an endothermic peak around at 166.26℃ was due to dehydration of cointercalated water in FB-LDH (120 - 225℃). The third weight loss (ca. 47.06%) was associated with an exothermic reaction in the range from 225 to 520℃. The three consecutive exothermic weigh losses were assigned to the multiple-step thermal decomposition

process of the organic guest, FB, simultaneously accompanied with the dehydroxylation of the hydroxide of $Zn_2Al$ layer. In the case of the FB-LDH hybrid, an additional weak exothermic peak is discernible at 654.08℃, which resulted from the formation of spinel $ZnAl_2O_4$ from ZnO and $Al_2O_3$ (Figure 2.9).

The content of FB in the FB-LDH nanohybrid measured by the elemental analysis and HPLC analysis was 44.21 ± 0.34 wt%, slightly lower than the one measured by thermal analysis because the latter seemed to be overestimated by concurrent dehydration and dehydroxylation of LDH layer at 225 - 520℃. The chemical compositions of pristine LDH and FB-LDH were $Zn_{0.67}Al_{0.33}(OH)_2Cl_{0.33} \cdot 0.32H_2O$ and $Zn_{0.68}Al_{0.33}(OH)_2FB_{0.24}Cl_{0.11} \cdot 1.06H_2O$, respectively, as shown in Table 2-2.

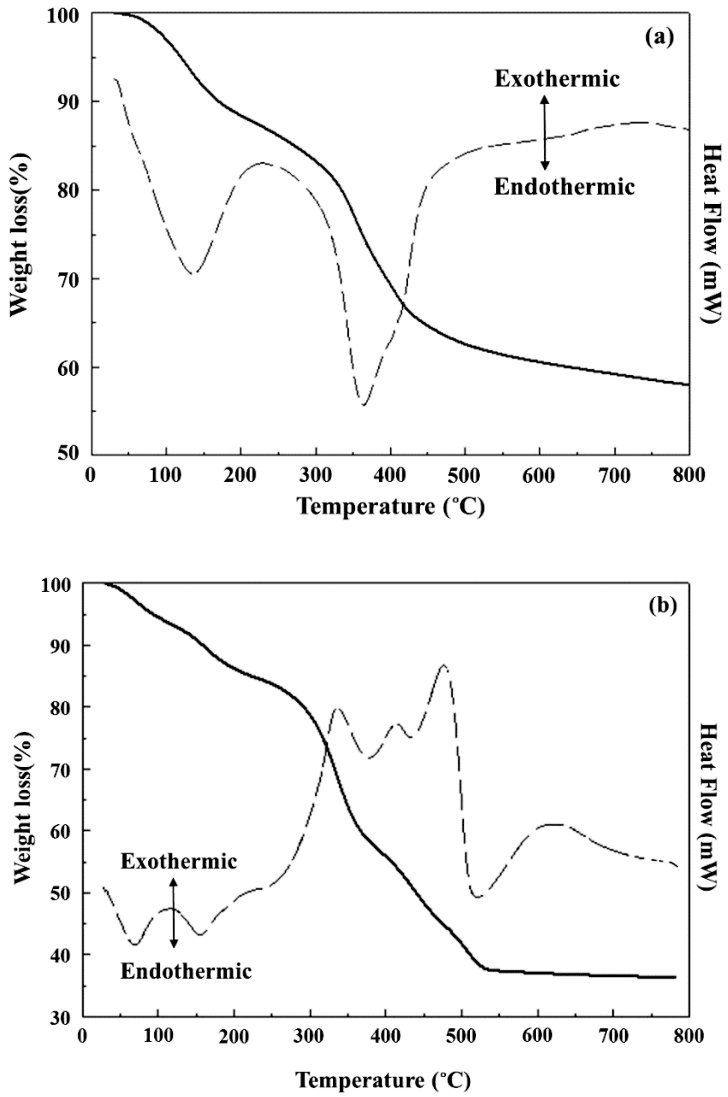


Figure 2.8. TGA–DTA curves of the (a) pristine LDH and (b) FB–LDH. The solid and dashed lines show the curves of TGA and DTA, respectively.

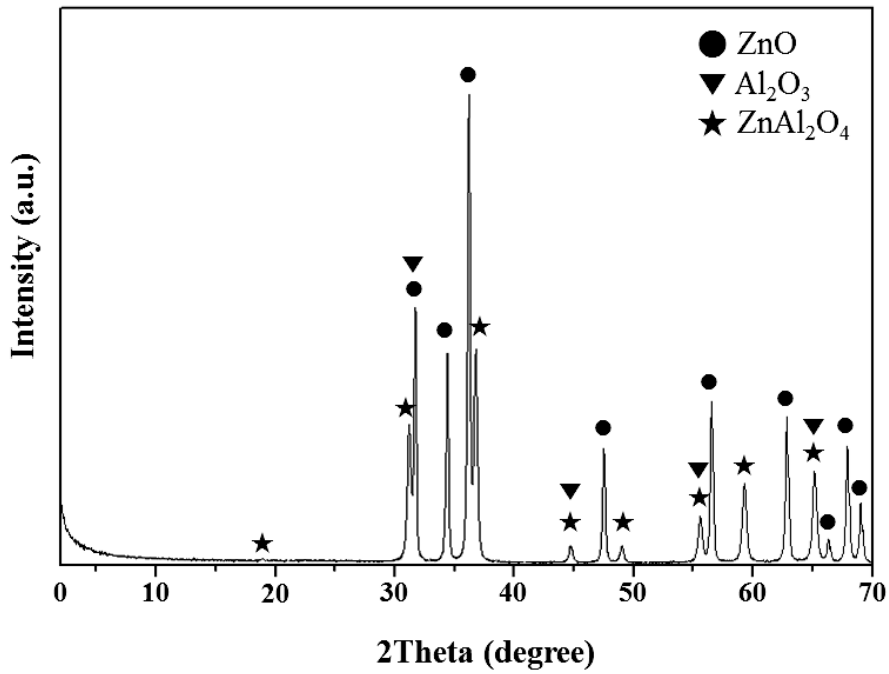

Figure 2.9. PXRD patterns of ZnO, $Al_2O_3$, and spinel $ZnAl_2O_4$.

Table 2.2. Chemical compositions of the pristine LDH and FB-LDH.

| | Chemical composition[a] | Zn/Al molar ratio[b] |
|---|---|---|
| Pristine LDH | $Zn_{0.67}Al_{0.33}(OH)_2Cl_{0.33} \cdot 0.32H_2O$ | 2.00 |
| FB-LDH | $Zn_{0.68}Al_{0.33}(OH)_2FB_{0.25}Cl_{0.10} \cdot 1.06H_2O$ | 2.06 |

[a] Calculated from elemental CHN analysis, ICP, TGA data.
[b] Calculated from ICP data.

### 2.4.5 *In vitro* Release Test of the FB-LDH

I performed the *in vitro* drug release experiments with the FB-LDH in pH 7.4 PBS at 37℃. To examine the effect of an anionic macromolecule on drug release, two distinct release media were employed, which were the pH 7.4 PBS solutions without and with Eudragit® S-100 (2.5 % w/v), respectively. As shown in Figure 2.10, more than a half of FB was released rapidly during the first 2 h in both media. The prevalent anions in PBS, such as $Cl^-$, appeared to facilitate deintercalation of FB molecules, hence initial burst release from the FB-LDH. However, in PBS without Eudragit® S-100, drug release was minimal after 4 h, showing almost a plateau of drug release (Figure 2.10(a)). The anions in PBS would cause the zipping effect due to its small size, where the lattice spacing would become smaller than the size of FB molecules and thus, eventually hinder the out-diffusion of the drug from the lattice space. However, the presence of Eudragit® S-100 indeed expedited drug release, realizing 100% release during the first 24 h (Figure 2.10(b)). Eudragit® S-100 would be fully dissolved and ionized in pH 7.4 PBS, which would efficiently replace the intercalated FB with many anionic sites in Eudragit® S-100. In addition, due to its large molecular size (*M*w : 125,kDa), the edge of LDH lattice would be enlarged to further aid the out-diffusion of the drug. As a result, with the presence of Eudragit® S-100, drug was continuously released from the FB-LDH in a sustained manner after 2 h (~ 1.06%/h).

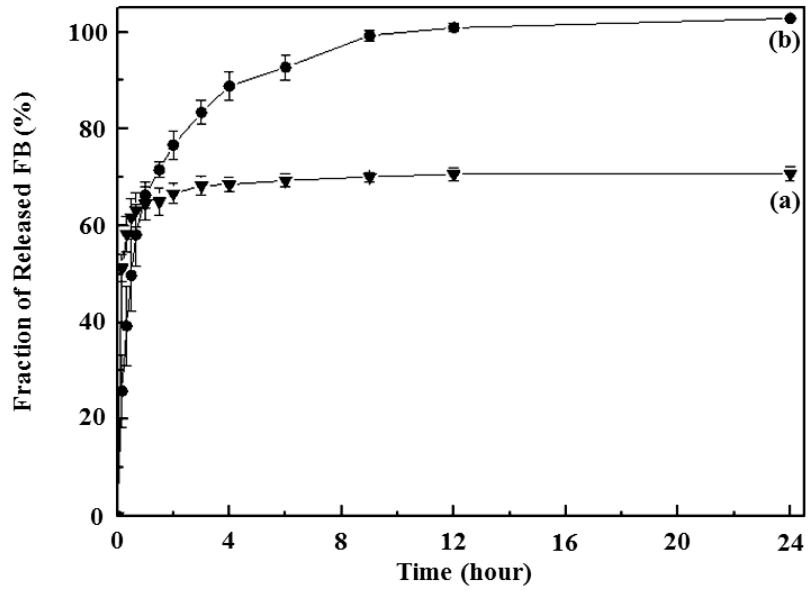


Figure 2.10. *In vitro* drug release profiles of the FB-LDH in pH 7.4 PBS (a) without Eudragit® S-100 and (b) with Eudragit® S-100

### 2.4.6 *In vitro* Skin Permeability Test of the FB-LDH Formulations

As a potential transdermal drug delivery formulation, I prepared a nonaqueous gel suspension of the FB-LDH, which was homogeneously mixed with an aqueous solution of Eudragit® S-100 (2.5 w/v%). In this work, I varied the amount of a Eudragit® S-100 aqueous solution to 0, 50, 100 and 200 μl per g of the FB-LDH gel suspension (i.e., G-FN-0, G-FN-50, G-FN-100, and G-FN-200, respectively) to examine the controlled-release property of the FB-LDH formulations, depending on the presence of anionic macromolecules. The formulations with a higher weight ratio of Eudragit® S-100 aqueous solution (> 20% w/w) were not tested in this work due to discernible phase separation between a gel and aqueous solution (Figure 2.11).

As shown in Figure 2.12, the cumulative amounts of FB delivered across a full thickness nude mouse skin were obtained from each of the gel formulations prepared in this work. The dose of FB was 20 mg for all gel formulations tested in this *in vitro* skin permeation study. For G-FN-0 (i.e., a gel suspension without a Eudragit® S-100 solution), drug permeation *via* the skin was very low, showing an evident lag time of 12.8 h and a steady state flux of ≈ 3.28 $\mu$g $cm^{-2}$ $h^{-1}$. The ionic exchange of the intercalated FB in the LDH lattices appeared to occur inefficiently without an aqueous phase, hence minimal drug release and thus, almost no drug available in the gel medium.

However, with the presence of a Eudragit® S-100 solution, drug delivery across the skin became more efficient. The steady state flux of FB increased to ≈ 5.79 $\mu$g $cm^{-2}$ $h^{-1}$ for G-FN-5 with the lag time of less than 1 h (Figure 2.12(b)). Anionic macromolecules (i.e., Eudragit® S-100) ionized in an aqueous phase would allow effective deintercalation of FB from the FB-LDH. The released drug would be distributed in a hydrophobic gel medium, which would then be delivered across the skin. As stated above, the hydrophobic FB would be likely to distribute mostly in a gel medium when released from the FB-LDH. The concentration of FB released into a gel medium is a critical determinant of the drug permeability *via* the skin.

Therefore, to control transdermal drug delivery, I increased the added amount of a Eudragit® S-100 solution, which would further facilitate the deintercalation of FB (i.e., FB release) from the FB-LDH and increase the drug concentration in the gel. As a result, the steady state flux of FB increased to ≈ 8.42 $\mu$g $cm^{-2}$ $h^{-1}$ and ≈ 14.57 $\mu$g $cm^{-2}$ $h^{-1}$ for G-FN-10 and G-FN-20, respectively, both also showing the lag times of less than 1 h (Figure 2.12(c-d)). As compared to G-FN-5, about a 3-fold increase in steady state flux of FB could be obtained with G-FN-200 in this work.

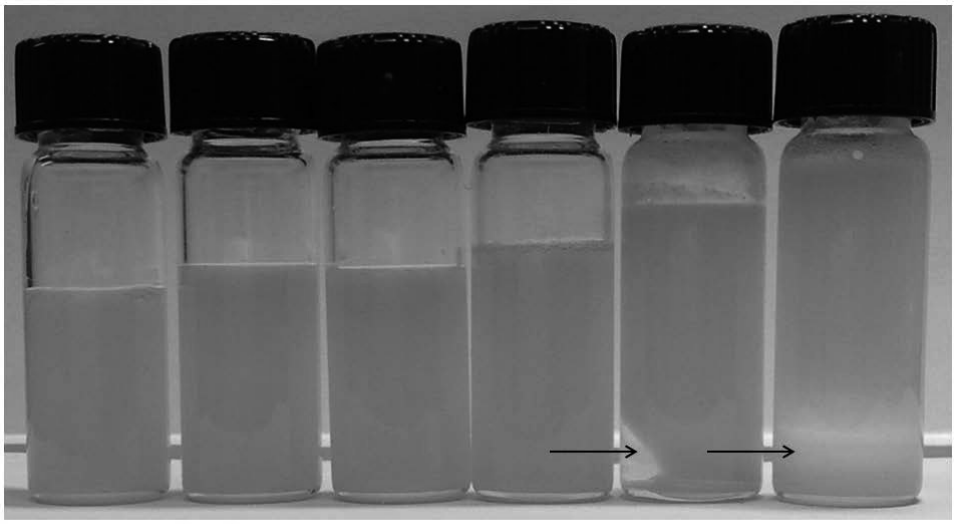


Figure 2.11. Phase separation was observed with the formulations with a mass ratio of Eudragit® S−100 aqueous solution, higher than 200 μl per g suspension.

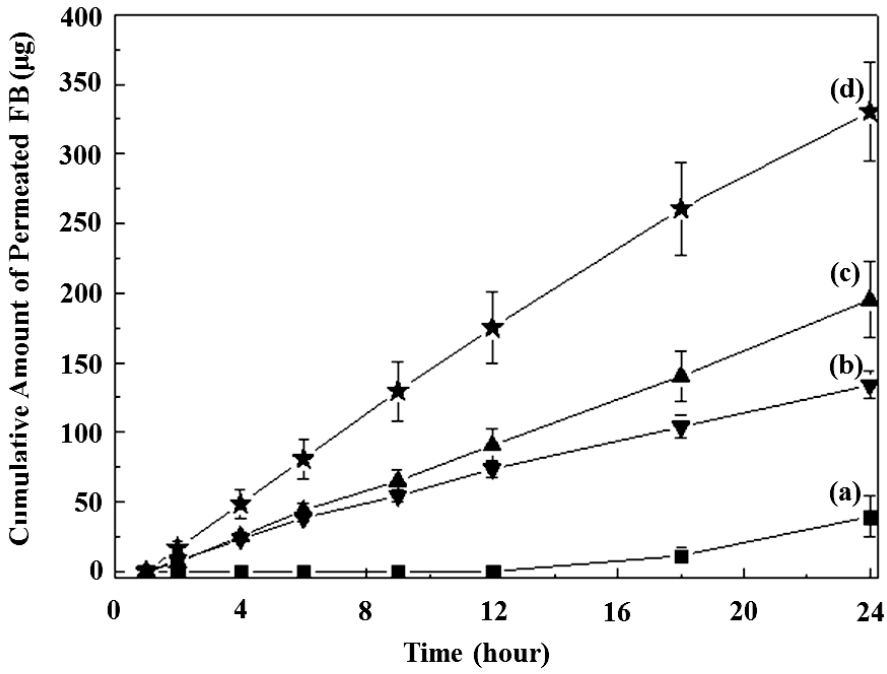


Figure 2.12. *In vitro* skin permeability profiles of (a) G-FN-0, (b) G-FN-5, (c) G-FN-10, and (d) G-FN-20.

## 2.5 Conclusion

For transdermal controlled drug delivery, I suggest a formulation of the drug–inorganic nanohybrid in this work. As I prepared FB–LDH by intercalating a transdermal model drug, FB, into LDH, the drug molecules could be well stabilized in the LDH layers. The nanohybrid can release the drug in a sustained manner, which can be better controlled with the presence of a macromolecule, possessing the same polarity comparable to the incorporated drug. According to the *in vitro* release experiments with the FB–LDH, the drug release could be facilitated with the presence of an anionic macromolecule, Eudragit® S–100, in the release media by expediting deintercalation of FB in LDH lattices.

The gel suspension of the nanohybrid can deliver the drug across the skin in a controlled manner, depending on the amount of aqueous solution of an anionic macromolecule mixed with gel suspension. I herein prepared the gel suspensions of FB–LDH with a varying amount of an aqueous solution of Eudragit® S–100 and performed the diffusion cell experiments using mouse skins. As a result, an average lag time and steady state flux of the drug could be varied from 12.8 h and ≈ 3.28 $\mu$g cm$^{-2}$ h$^{-1}$ to less than 1 h and ≈ 14.57 $\mu$g cm$^{-2}$ h$^{-1}$, respectively. Therefore, I conclude that a gel suspension of the nanohybrid containing a tailored amount of an aqueous solution of macromolecules is a novel formulation for controlled delivery of a transdermal drug.

# Chapter 3

## Alendronate-Layered Double Hydroxide Nanohybrid for *In vitro* Enhancement of Osteogenic Proliferation and Differentiation of MG63 Cells

### 3.1 Abstract

Alendronate (AL), a drug for inhibiting osteoclast-mediated bone-resorption, was successfully intercalated into layered double hydroxide (LDH) by ion-exchange reaction to form an X-ray single phasic drug-clay nanohybrid (AL-LDH). The accumulated AL content in human osteoblast-like cells (MG63) treated with the AL-LDH was determined to be 10.6-fold higher than that within those

treated with intact AL after incubation for 1h, suggesting that intracellular permeation of AL was facilitated due to the hybridization with the drug delivery vehicle, LDH. To verify an enhanced cellular uptake behavior of LDH itself, a green fluorescent dye, FITC, was adsorbed on carbonate type of LDH (LDH−$CO_3$) to form FITC−LDH−$CO_3$, which was then further treated in the cell culture lines and studied with confocal laser scanning microscopy. As expected, the fluorescence intensity within cytoplasm of MG63 cells treated with the FITC−LDH−$CO_3$ was significantly stronger than that treated with FITC only. Furthermore, both in vitro proliferation level and ALP activity of MG63 treated with the AL−LDH were found to be much more enhanced than those treated with intact AL, though LDH itself could not prompt cell proliferation and osteogenic differentiation of MG63. Therefore, the AL−LDH, the combined entity of AL and anionic clay, could be considered as a promising drug delivery system for improving efficacy of AL.

## 3.2 Introduction

Intracellular delivery has attracted great attentions for improving therapeutic benefits of various bioactive molecules that have difficulty and inefficiency to go across the cell membrane due to their enzymatic drug degradation, low circulation stability, and lack of target specificity [67-69]. In the past few decades, many efforts have been made to design and investigate various inorganic nanovehicles due to their suitable features for intracellular delivery, such as facile surface modification for targeted delivery, low toxicity, and controlled/sustained release property [37, 70, 71].

High anion exchange capacity (AEC) of LDH offers to intercalate various kinds of negatively charged bioactive molecules in the interlayer space of LDHs *via* simple co-precipitation or ion-exchange reactions, resulting in novel bio-inorganic nanohybrids [15, 26-29]. Also, the positive surface charge of LDH enables easy approach and adhesion to inherently negatively charged cell membranes by electrostatic interactions without further chemical modifications [30, 31]. Most importantly, LDH contributes to a high transportation efficiency of bioactive molecules through its unique cellular uptake mechanism, clathrin-mediated endocytosis [32-34]. As compared to other inorganic nano-vehicles, including silica and gold nanoparticles, quantum dots, and carbon nanotubes, LDH is highly advantageous due to its excellent biocompatibility [9, 35], high drug loading capacity [36, 37], and pH-responsive property [38-40]

with biodegradability in the cellular cytoplasm [11, 31, 34], and therefore, applicable as an efficient non-viral drug delivery vehicle and also as a reservoir for bioactive or bio-fragile molecules.

In the present study, an attempt has been made to enhance the cellular uptake efficacy of alendronate (AL), an anti-resorptive and bone-remodeling drug, by encapsulating it into the drug delivery vehicle (LDH), to form a AL-LDH with layered heterostructure. AL has been clinically used to treat diseases from osteoclast-mediated bone resorption such as bone metastasis, post-menopausal osteo-porosis and Paget's disease [78, 79], because it impedes bone resorption by selective uptake and absorption to divalent ions in bone due to its strong chelating molecular configuration with di-phosphates (P–O–P and P–C–P) [80, 81]. Moreover, it has been proved to not only inhibit osteoclastic bone resorption but also induce mineralization of newly formed bone by osteoblasts [82-84]. Due to its negative molecular charge and high hydrophilicity, however, AL has its intrinsic adverse effect such as low intracellular permeability, which in turn results in low drug efficacy [85, 86]. To the best of our knowledge, this is the first study to examine the improved efficacy of AL-LDH, the chemically well-defined two-dimensional nanohybrid, on the proliferation and osteogenic differentiation of human osteoblast-like cell line (MG63) by employing LDH as a drug delivery carrier. Though there was only one trial related to the intercalation reaction of AL into LDH, all the samples were, however, neither X-ray single phasic nor chemically defined, due to the fact

that the intercalation reaction could not reach to an equilibrium [87]. In this respect, I intended to prepare the X-ray single phasic AL-LDH considering various reaction parameters such as reaction pH, concentration of AL, and AEC of LDH.

I attempted to find out the synthetic condition of the AL–LDH based on intercalative ion-exchange reaction, where 2.5-fold excess amount of AL was reacted with the pristine LDH taking into account AEC of LDH, since the reaction rate should be responsible for the formation of the X-ray single phasic AL-LDH. The pH of solution should influence the ion-exchange reaction of AL with LDH due to amphiprotic nature of AL. Thus, I carefully controlled the pH during the reaction on the basis of the pKa values of AL. The AL-LDH herein was characterized by powder X-ray diffraction (PXRD), high resolution transmission electron microscopy (HR-TEM), and Fourier transform infrared (FTIR) spectroscopy in order to confirm the single phasic AL-LDH with 2D heterostructure. And finally, the cellular uptake behavior of AL-LDH was quantitatively studied by evaluating concentrations of AL within cells, which was then compared with that of intact AL. Furthermore, a green dye, fluorescein isothiocyanate (FITC) was immobilized into carbonate type of LDH (LDH-$CO_3$) to form FITC-LDH-$CO_3$, used to trace the internalization of LDH into the cells by confocal laser scanning microscopy (CLSM). The improved efficacy of AL using the AL-LDH was compared to that of intact AL by evaluating *in vitro* cell proliferation and alkaline phosphatase (ALP) activity of MG63 cells.

## 3.3 Experimental Section

### 3.3.1 Materials

All chemicals zinc nitrate hexahydrate ($Zn(NO_3)_2 \cdot 6H_2O$), magnesium nitrate hexahydrate ($Mg(NO_3)_2 \cdot 6H_2O$), aluminum nitrate nonahydrate ($Al(NO_3)_3 \cdot 9H_2O$), alendronate in sodium trihydrate form ($C_4H_{12}NaNO_7P_2 \cdot 3H_2O$), sodium hydroxide (NaOH), sodium carbonate ($Na_2CO_3$), fluorescein 5'-isothiocyanate (FITC), ferric chloride hexahydrate ($FeCl_3 \cdot 6H_2O$), β-glycerophosphate, dexamethasone, and L-ascorbic acid were purchased from Sigma (MO, USA). Perchloric acid ($HClO_4$) was obtained from Junsei (Japan). Dulbecco's modified Eagle's essential medium (DMEM), penicillin streptomycin, fetal bovine serum (FBS), 0.25% Trypsin-EDTA (1X) and Dulbecco's Phosphate-buffered saline (DPBS) were obtained from Gibco (MA, USA). A cell counting Kit-8 (CCK-8) and p-nitrophenyl phosphate (pNPP) ALP assay kit were supplied from Dojindo (Japan) and AnaSpec (CA, USA), respectively.

### 3.3.2 Preparation of Nanohybrids

10 mmol $Zn(NO_3)_2 \cdot 6H_2O$ and 5 mmol $Al(NO_3)_3 \cdot 9H_2O$ (molar ratio of $M^{2+}/M^{3+}$ = 2) were dissolved in 100 ml decarbonated water by vigorous agitation for 0.5 h until the solution became transparent. Then, the mixed metal solution was coprecipitated by titrating with 0.5 M NaOH solution to pH 8.0 and aged at room temperature for 12

h. The resulting white precipitate (LDH−$NO_3$) was separated by centrifugation and washed with decarbonated water to completely remove the unreacted ions, and finally freeze−dried.

The AL−LDH was synthesized by intercalating AL molecules into the LDH−$NO_3$ *via* ion−exchange reaction. At first, 0.05 M solution of AL in 100 ml of decarbonated water was adjusted to pH 8.0 with 0.5 M NaOH solution in order to dissociate the protons in AL. The LDH−$NO_3$ suspension was then intermixed with this AL solution and the pH of the final solution was maintained at 10.9 for 24 h at room temperature. The resulting AL−LDH was separated by centrifugation and washed thoroughly with decarbonated water, and freeze−dried. All the reactions were carried out under nitrogen atmosphere to avoid carbonate contamination.

10 mmol $Mg(NO_3)_2 \cdot 6H_2O$ and 5 mmol $Al(NO_3)_3 \cdot 9H_2O$ (molar ratio of $M^{2+}/M^{3+}$ = 2) was dissolved in 100 ml decarbonated water by vigorous agitation for 0.5 h until the solution became transparent. For nitrate and carbonate type of MgAl LDH (abbreviated as MgAl_$NO_3$ LDH and MgAl_$CO_3$ LDH, respectively), each of the mixed metal solution was titrated with 0.5 M NaOH solution and a mixture of 0.5 M NaOH containing basic $Na_2CO_3$ (50 mmol), respectively, to pH 10.0, which was then aged at room temperature for 12 h. The resulting each precipitate was separated by centrifugation and washed three times with decarbonated water to remove the unreacted ions. A dry powder of MgAl_$NO_3$ LDH and MgAl_$CO_3$ LDH was obtained by freeze−drying.

Next, I attempted to prepare AL intercalated LDH nanohybrid by ion-exchange reaction. Briefly, 0.05 M solution of AL was dissolved in 100 ml of decarbonated water and the pH was adjusted to 8.0 simply with 0.5 M NaOH solution. To this AL solution, each suspension of MgAl_$NO_3$ LDH or MgAl_$CO_3$ LDH was pour and the pH of the mixed solution was maintained at 10.9 for 24 h at room temperature. The each of resulting precipitates was filtered, washed thoroughly with decarbonated water, and freeze-dried. All the reactions were carried out under nitrogen atmosphere to avoid carbonate contamination from air.

For preparing FITC adsorbed LDH, 10 mmol $Zn(NO_3)_2 \cdot 6H_2O$ and 5 mmol $Al(NO_3)_3 \cdot 9H_2O$ (molar ratio of $M^{2+}/M^{3+}$ = 2) were completely dissolved in 100 ml deionized (DI) water. Then, 0.5 M NaOH solution containing $Na_2CO_3$ (50 mmol) was drop-wisely added to the mixed metal solution and its pH was maintained at 8.0. And the mixture was aged at room temperature for 12 h with continuous stirring. The resulting carbonate type of LDH (LDH-$CO_3$), were centrifuged, washed with DI water to remove unreacted ions, and freeze-dried. Then, FITC was adsorbed on the surface of the LDH-$CO_3$ by mixing equal volumes of FITC (5 mg/ml) and LDH-$CO_3$ (5 mg/ml) together, followed by stirring for 12 h. The resulting FTIC adsorbed LDH-$CO_3$ (FITC-LDH-$CO_3$) was obtained by thoroughly washing the excess FITC with DI water and freeze-dried.

### 3.3.3 Characterizations

PXRD patterns were measured using an X-ray diffractometer (D/MAXRINT 2200-Ultima, Rigaku, Japan) equipped with Ni-filtered Cu-K$\alpha$ radiation ($\lambda$ = 1.5418 Å). The samples were separately loaded on a glass holder and continuously scanned at the tube voltage of 40 kV and the current of 30 mA. HR-TEM image of the AL-LDH was obtained using JEM-2100F (JEOL, Japan), which was operated at an accelerating voltage of 200 kV. FT-IR spectra were measured with a JASCO 6100 spectrophotometer (JASCO, Japan) in a range of 400 – 4000 $cm^{-1}$ with 4 $cm^{-1}$ resolution with the potassium bromide disk pellet method. Field emission scanning electron microscopy (FE-SEM) images were obtained using JSM-6700F (JEOL, Japan). Before imaging, each sample was sputter-coated with platinum (208HR, Cressington Scientific, UK). The size distribution and surface charge were measured with a zetasizer (Nano ZS, Malvern, UK).

$FeCl_3$ standard solution (5 mM) in a 2 M $HClO_4$ were used in order to measure the contents of AL in the AL-LDH. Five different concentrations of AL, ranging from 0.025 to 2.5 mM, were dissolved in 2 M $HClO_4$ as well. A mixtures of AL and $FeCl_3$ standard solution (1:1, v/v) were measured by UV-Vis spectrophotometer (Perkin-Elmer Lambda 35, USA) for calibration curve of AL [88]. The AL-LDH was dissolved in 2 M $HClO_4$ solution and filtered with Nylon syringe filter (0.45 $\mu$m pore, Millipore, USA). Then, the dissolved

AL from the AL- LDH was mixed with the $FeCl_3$ standard solution (1:1, v/v). The resulting mixtures were measured by UV-Vis spectrophotometer. Elemental CHN analyses with EA1110 (CE instrument, Italy) and inductively coupled plasma (ICP) analyses with Optima-4300 DV (PerkinElmer, USA) were further carried out in order to confirm chemical compositions of the LDH-$NO_3$ and AL-LDH.

### 3.3.4 *In vitro* Drug Release Test

To examine *in vitro* drug release profile, the AL-LDH was suspended in 900 ml of pH 7.4 PBS at 37° C and continuously stirred at 125 rpm using a dissolution apparatus 2 (paddle type, Vision® G2 Elite 8TM Dissolution Tester, Hanson, USA) [19]. At scheduled time for 100 days, 3 ml of the medium was collected and the same amount of fresh PBS was added back. The sampled medium was filtered with Nylon syringe filter (0.45 $\mu$m pore, Millipore, USA), which was added to the $FeCl_3$ standard solution to quantitatively measure the released amount of AL out of the AL-LDH using UV-Vis spectrophotometer. At least three batches were tested for statistics.

### 3.3.5 *In vitro* Cell Study

MG63 cells (Korean Cell Line Bank) were grown in DMEM medium supplemented with 10% heat inactivated fetal bovine serum, 100 units/ml penicillin, and 100 μg/ml streptomycin under a 5% $CO_2$

atmosphere with 95% humidity at 37 ° C. When the cells grew up to 80 – 90% confluence, they were isolated from cell culture dishes by trypsinization and washed with 10 mM DPBS.

### 3.3.5.1 Quantification of Accumulated AL in MG63 Cells

MG63 cells seeded on a 60 mm culture dish at a density of $2.0 \times 10^6$ cells/well were treated with intact AL (50 μg/mL) and AL-LDH containing an equivalent amount of AL. After the given incubation time for 1, 2, 4, 6, 12, and 24 h, the cells were washed twice with DPBS, harvested by trypsin-EDTA treatment, and separated by centrifugation. After the precipitated pellets were washed twice with DPBS, 5 ml of cell lysis buffer (20 mM Tris-HCl, pH 7.5, 1% Triton X-100, 150 mM NaCl, and 1 mM EDTA) was added and the pellets were incubated on ice for 20 min followed by ultrasonication (Sonics & Materials Inc.) for 20 s. After centrifuging the crude cell lysates at 10000 rpm for 5 min, 10 ml acetonitrile (DAEJUNG, Korea) was added to the cell supernatants the resulting mixture was vigorously vortexed to precipitate proteins. After further centrifugation of the mixture at 10000 rpm for 3 min, 20 ml chloroform (DAEJUNG, Korea) was added to the supernatant to remove lipids, which was then collected by centrifugation at 2000 rpm for 10 min. The final supernatant was added to the $FeCl_3$ standard solution to measure the concentration of AL using UV-Vis spectrophotometer. Each experiment was repeated at least three

times.

### 3.3.5.2 Confocal Laser Scanning Microscopy Study

For CLSM measurements, MG63 cells in 2 ml of DMEM medium ($2.0 \times 10^6$ cells/well) were seeded in Coverglass bottom dish (SPL Lifesciences Co., Ltd, Korea) and incubated 24 h at 37° C and 5% $CO_2$. Then, the medium in the well was replaced by the FITC-LDH-$CO_3$ suspension (20 μg/ml) in fresh medium and incubated under the same condition. A control experiment was also performed with the centrifugal supernatant of the FITC-LDH-$CO_3$ suspended in the cell medium under the same conditions. After incubation for 1 h, the cells were washed three times with DPBS and fresh cell medium were then added to the plates. For the staining of nucleus, 140 μl of NucBlue (Live Cell Stain ReadyProbes™ reagent, molecular probes by Life technologies) was added and incubated for additional 20 min at 25° C. The stained cells were imaged under a confocal laser scanning microscope (Leica TCS SP8 STED CW) equipped with both DAPI filter (Ex. 420nm/Em. 460 nm) and FITC filter (Ex. 495nm/Em. 520 nm). The obtained images were processed using Leica LAS AF software.

### 3.3.5.3 Proliferation Study

MG63 cells were seeded onto 96-well plates at a density of $2 \times 10^4$ cells/well and incubated at 37° C under a 5% $CO_2$

atmosphere for 24 h. Then, the cell medium in each well was completely substituted with osteogenic medium (2 mM L-glutamine, 10 mM $\beta$-glycerophosphate, and 50 ng/ml L-ascorbic added to cell media) containing LDH-$NO_3$, intact AL, or AL-LDH and the cells were cultured for 2, 3, or 4 days. The cells were incubated with intact AL or AL-LDH at the equivalent AL concentrations of $1 \times 10^{-10}$ M, $1 \times 10^{-8}$ M, and $1 \times 10^{-6}$ M. The cells were also incubated with the LDH-$NO_3$ at the equivalent LDH concentrations used with the AL-LDH above. At every predetermined time, the cells were washed with DPBS and the cell proliferation was assessed with CCK-8, following the manufacturer's instruction [89]. Briefly, 100 $\mu$l CCK-8 solution was added into each well and cultured for additional 3 h. Then, optical density of each well was measured at 450 nm on a microplate reader (Multiskan FC, Thermo Scientific, USA), and expressed in percentage based on optical density of negative control (only osteogenic medium was treated to the cells). The assay was performed at least three times for statistics.

### 3.3.5.4 Alkaline Phosphatase (ALP) Activity

MG63 cells were cultured in 6-well plates at a density of $1.5 \times 10^5$ cells/well and incubated overnight at 37° C under a 5% $CO_2$ atmosphere for 24 h. The cell medium in each well of the plate was completely substituted with the osteogenic medium containing LDH-$NO_3$, intact AL, or AL-LDH and treated under the same conditions

described above. At a given time, the adherent cells were scraped off and suspended in 3 ml of osteogenic medium, which was shaken at 4° C for 10 min and centrifuged at 2500 rpm for 10 min. The supernatant (50 $\mu$l) was then transferred to 96-well plate and pNPP solution (50 $\mu$l) was added [82]. The total amounts of released enzyme from the cells were spectrophotometrically measured by a microplate reader (Multiskan FC, Thermo Scientific, USA) at 405 nm. At least three times were tested for each sample type.

### 3.3.6 Statistical Analysis

A statistical analysis of the data from *in vitro* cell proliferation and ALP activity was applied in one-way ANOVA with $\alpha$ = 0.05 followed by pairwise comparisons using a Tukey's post hoc test (GraphPad Prism, version 5.01, USA). $p < 0.05$ was considered statistically significant.

## 3.4 Results and Dicussion

### 3.4.1 Powder X-ray Diffraction (PXRD) Analysis

In the previous work,[87] the intercalation of AL into LDH was attempted, but the AL-LDH nanohybrid was not successfully prepared. According to the X-ray analysis, no X-ray single phasic AL-LDH was synthesized due to the formation of thermodynamically stable carbonate ions intercalated LDH. Thus, I intended to find out synthetic conditions for the X-ray single phasic AL-LDH by taking into account the AL concentrations in a reaction solution with respect to AEC of LDH and the pH of the solution as well. According to the calculated molar fraction of AL depending on pH (Figure 3.1), AL may exist in the forms of $AL^{2-}$ = 0.49, $AL^{3-}$ = 0.49, and $AL^{4-}$ = 0.02 at pH 10.9, in which primary amine group in AL could be considered to be almost deprotonated. Thus, I set the pH of solution at 10.9 in order for the intercalative ion-exchange reaction of AL into LDH not to be disturbed by protonated primary amine in AL.

A 2.5-fold excess amount of AL was reacted with the prepared carbonate type of $Mg_2Al$ LDH ($Mg_2Al-CO_3$ LDH) and nitrate type of $Mg_2Al$ LDH ($Mg_2Al-NO_3$ LDH), respectively, at pH 10.9. As shown in Figures 3.2(a-b), AL molecules were not successfully intercalated into both LDHs. The XRD patterns of $Mg_2Al-CO_3$ LDH reacted with AL were not changed depending on reaction time, but determined as the same as that of the pristine $Mg_2Al-CO_3$ LDH. When the ion-exchange reaction of AL with $Mg_2Al-NO_3$ LDH was made for

24 h, however, two phases, AL intercalated LDH and unreacted $Mg_2Al-NO_3$ LDH, could be observed. On the other hand, AL was successfully intercalated into nitrate type of $Zn_2Al$ LDH (abbreviated as LDH-$NO_3$) showing an X-ray single phase (Figure 3.2(c)). While AL intercalated LDH and the LDH-$NO_3$ coexisted at 4 h and 8 h, the intercalation reaction of AL into the LDH-$NO_3$ was reached to an equilibrium beyond 12 h, where well-ordered (00*l*) reflections could be observed for AL-$Zn_2Al-NO_3$ LDH (abbreviated as AL-LDH).

As shown in Figure 3.3(A), after intercalation of AL into the LDH, the basal spacing was expanded to 11.3 Å from 8.7 Å (that of LDH-$NO_3$), which clearly demonstrated that AL molecules were well intercalated into the interlayer space of LDH lattice. The gallery height of AL-LDH was estimated to be 6.5 Å [11.3 Å – 4.8 Å (the thickness of LDH single layer)], which was smaller than the molecular dimension of AL as shown in Figures 3.4(A-B). It is, therefore, expected that AL molecules were likely to be stabilized with a monolayer arrangement as shown in Figure 3.4(C).

To confirm this configuration, I investigated the steric limitation between the intercalated AL molecules and positively charged sites of LDH layers, which can be explained by the equivalent area ($A_e$, area per positive unit charge of LDH) and demanded area ($A_c$, area per negative unit charge for intercalated single molecule). $A_e$ of the layered host lattice can be calculated from the following equation, $A_e = a \cdot b \cdot \sin\gamma / \xi$, where *a* and *b* are lattice parameters and $\xi$ is the layer charge per formula unit. On the basis

of the lattice parameters of the AL−LDH ($a$ = $b$ = 3.07 Å, $c$ = 33.78 Å, $\gamma$ = 120° and $\xi$ = 1/3e⁻), $A_e$ of LDH was 24.5 Å$^2$, which was larger than the demanded area ($A_c$) of AL (24.0 Å$^2$). In the range of $A_e > A_c$, the guest molecules could be incorporated between the LDH layers with parallel monolayer orientation along with the ab plane of LDH.

In order to gain further insight in the arrangement of intercalated AL molecules in the interlayer space of LDH, I compared relative intensity ($I_{rel}$) of the observed X−ray intensity ($I_{obs}$) to those of the calculated X−ray intensity ($I_{cal}$) from physicochemically possible structural models of the AL−LDH (Figure 3.5(A−C)) along the crystallographic c−axis. The structure factor (F(00$l$)) of the each structural model was obtained from the atomic scattering factor for each atom in the unit cell ($f_i$) and the position of atoms ($z_i$) along c−axis consisting of the structure by following the equation, $F(00l) = \sum_{i=0}^{N} f_i \cos(2\pi l z_i)$.[90] The integrated intensity of (00$l$) diffraction peak (I(00$l$)) was proportional to the square of F(00$l$) and to Lorentz−Polarization factor (LP($\theta$) = (1+ $\cos^2 2\theta$)/($\cos\theta \cdot \sin^2\theta$)).

Taking into account of steric limitation between the intercalated AL molecules and positively charged sites of the LDH layer, basal spacing of the AL−LDH, and molecular dimension of AL, I could expect three structural models of AL−LDH as follows; 1) two phosphate groups of AL molecule were electrostatically interacted with up and down sides of LDH layers as shown in Figure 3.5(A) and 2) two phosphate groups of AL molecule were electrostatically

interacted with one side (up or down side) of LDH layer as shown in Figures 3.5(B-C). Although it was not easy to refine the interlayer structure of the AL-LDH due to a limited number of (00*l*) diffractions, the interlayer structure of AL-LDH in Figure 3.5(C) would be highly probable among the three structure models: the $I_{cal}$ values from the model were close to the $I_{obs}$ values, as shown in Figure 3.5(D). In case of the structural model of AL-LDH depicted in Figure 3.4(A), $I_{cal}$ of (00*l*) became exponentially decayed with increasing *l* values, which was very different from the observed XRD intensity ($I_{obs}$).

### 3.4.2 High Resolution Transmission Electron Microscopy (HR-TEM) Study of the AL-LDH

Through cross-sectional HR-TEM image of AL-LDH as shown in Figure 3.3(B), I clearly confirmed a well-ordered two dimensional layered structure of the AL-LDH along the crystallographic c-axis. The length between the lattice fringes from the (00*l*) planes in the AL-LDH was observed to be approximately 11.3 Å, which was in excellent agreement with the basal spacing obtained from the PXRD pattern of the AL-LDH.

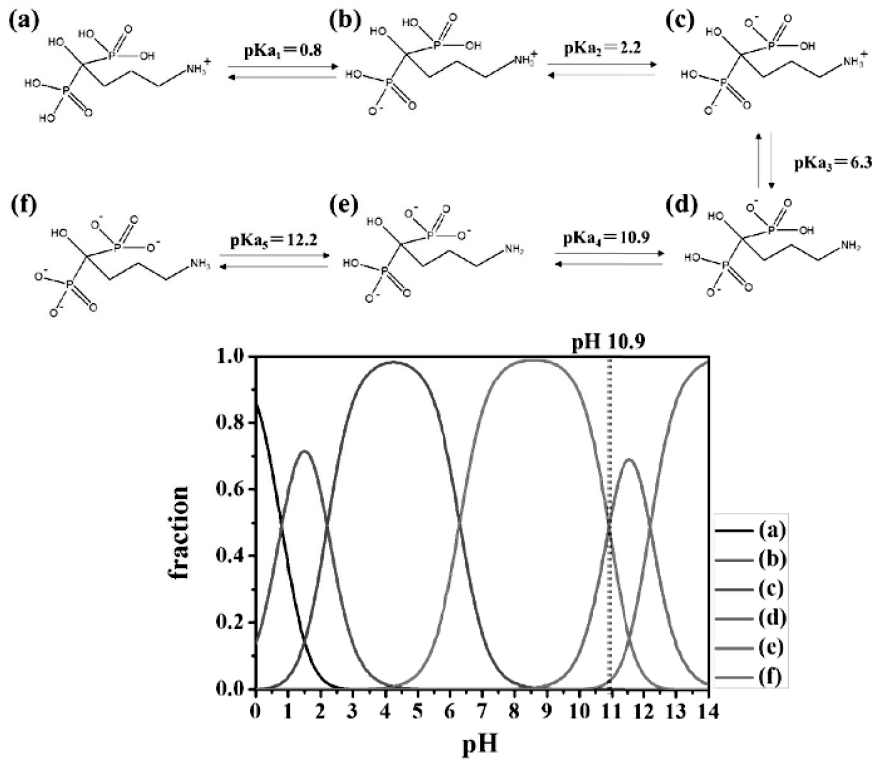


Figure 3.1. Chemical structures and dissociations of AL depending on the values of equilibrium dissociation constant (pKa) of AL. Molar fraction of AL calculated from its pKa values depending on pH.

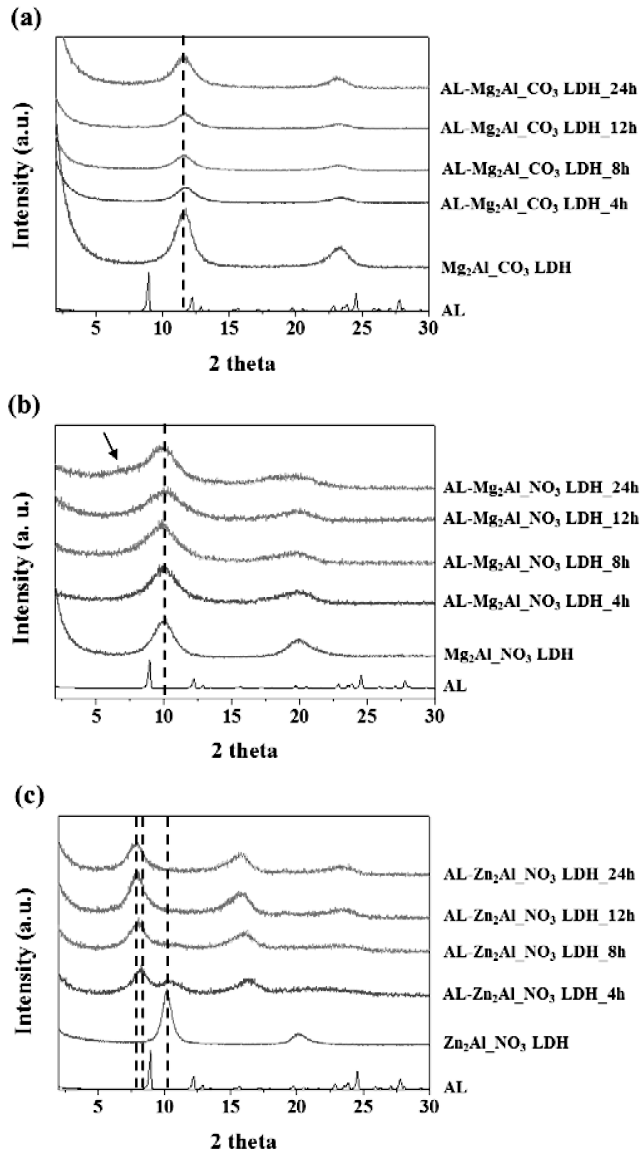


Figure 3.2. PXRD patterns of AL intercalated into (a) $Mg_2Al_CO_3$ LDH, (b) $Mg_2Al_NO_3$ LDH, and (c) $Zn_2Al_NO_3$ LDH nanohybrids.

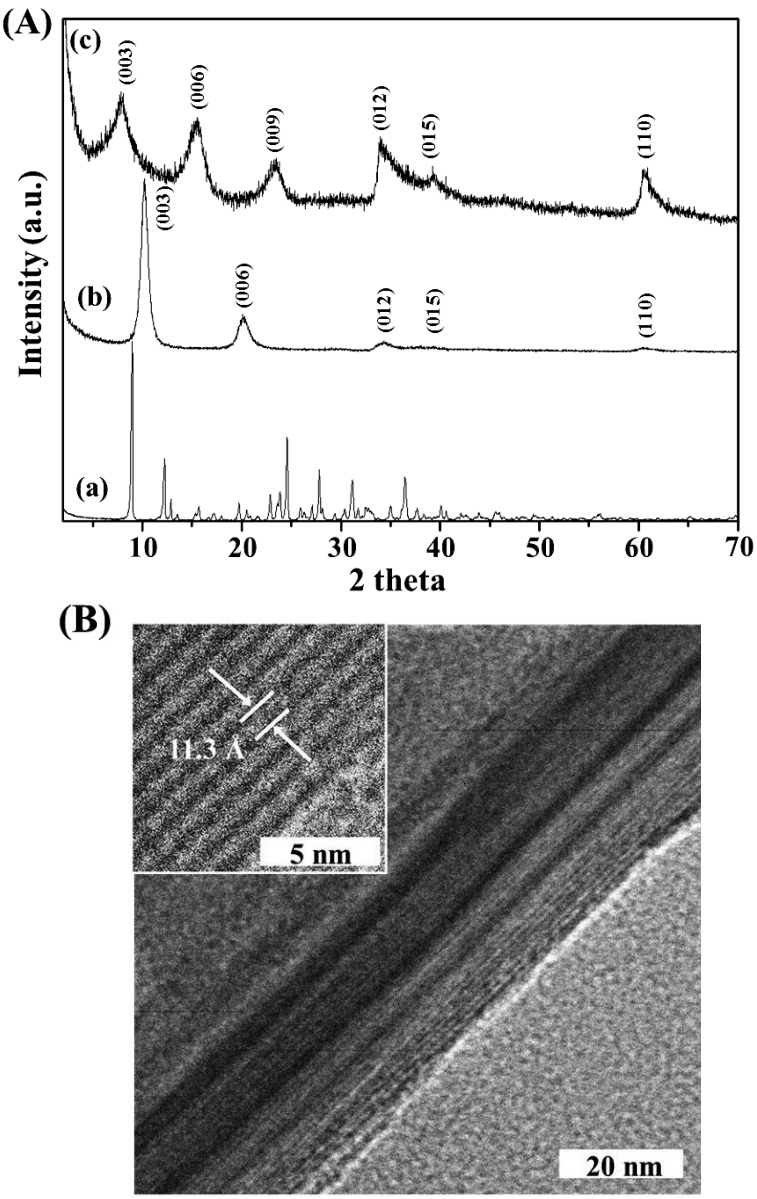


Figure 3.3. (A) PXRD patterns of (a) intact AL, (b) LDH−$NO_3$, and (c) AL−LDH. (B) HR−TEM image of AL−LDH with inset of higher magnification.

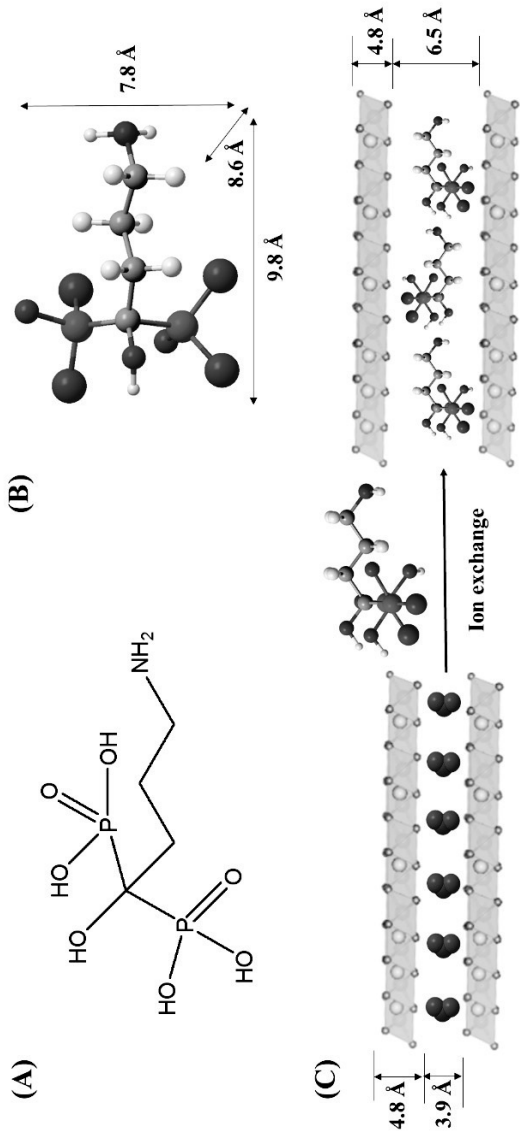


Figure 3.4. (A) Chemical structure and (B) 3-dimensional chemical structure of AL. (C) Schematic diagram of AL molecules intercalated in the LDH layer *via* intercalative ion-exchange reaction.

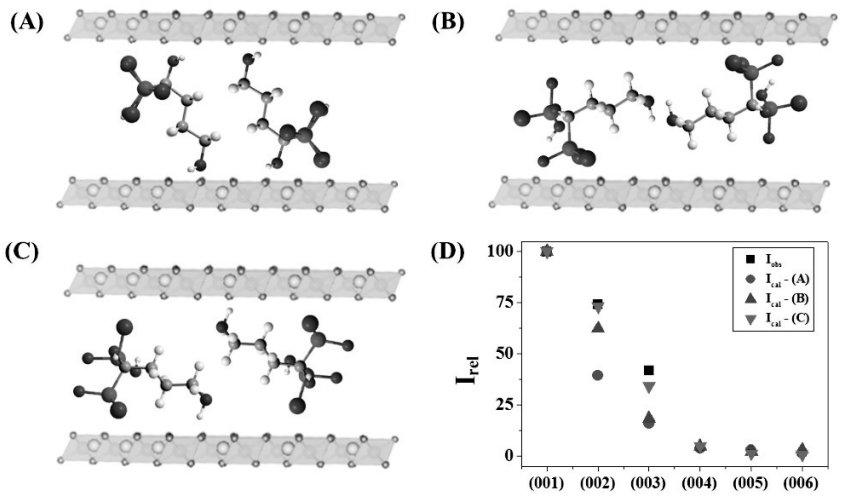


Figure 3.5. (A-C) Structural models for the AL-LDH along c-axis. (D) The relative X-ray intensity ($I_{rel}$) of the observed and calculated X-ray intensity of AL-LDH.

### 3.4.3 Fourier Transform Infrared (FT-IR) Analysis

The FT-IR spectrum of (c) AL-LDH was compared to those of (a) intact AL and (b) LDH-$NO_3$ (Figure 3.6). For intact AL, the characteristic infrared vibration bands, such as O-H of phosphate (3490 $cm^{-1}$), C-H (2965 $cm^{-1}$), N-H (1545 $cm^{-1}$), C-O-C (1119 $cm^{-1}$), P=O (1056 $cm^{-1}$), and P-O (960 $cm^{-1}$), were clearly observed.[91-93] For the LDH-$NO_3$, broad absorption bands at 3451 and 1642 $cm^{-1}$ were assigned as O-H stretching of the hydroxide layer vibration and interlayer water in LDH, respectively. The absorption bands found in the low frequency region below 800 $cm^{-1}$ were attributed to lattice vibration modes such as M-O and M-O-M vibrations. All characteristic bands from intact AL and LDH-$NO_3$ were overlapped within those of the AL-LDH. Notably, the nitrate absorption peak at 1382 $cm^{-1}$, which was seen in the LDH-$NO_3$, disappeared in the AL-LDH, implying that the nitrate ions were completely replaced with negatively charged AL molecules through the intercalative ion-exchange reaction. The broad peak between 1800 and 2700 $cm^{-1}$ corresponding to the OH stretching vibration in the O=P-OH group of AL,[94] disappeared in the AL-LDH due to the deprotonation of OH groups, which were electrostatically interacted with the LDH layers. Furthermore, C-C (1470 $cm^{-1}$) and C-N (1411 $cm^{-1}$) stretching bands of AL were redshifted to 1432 and 1367 $cm^{-1}$, respectively, because of the hybridization of AL and LDH.[95]

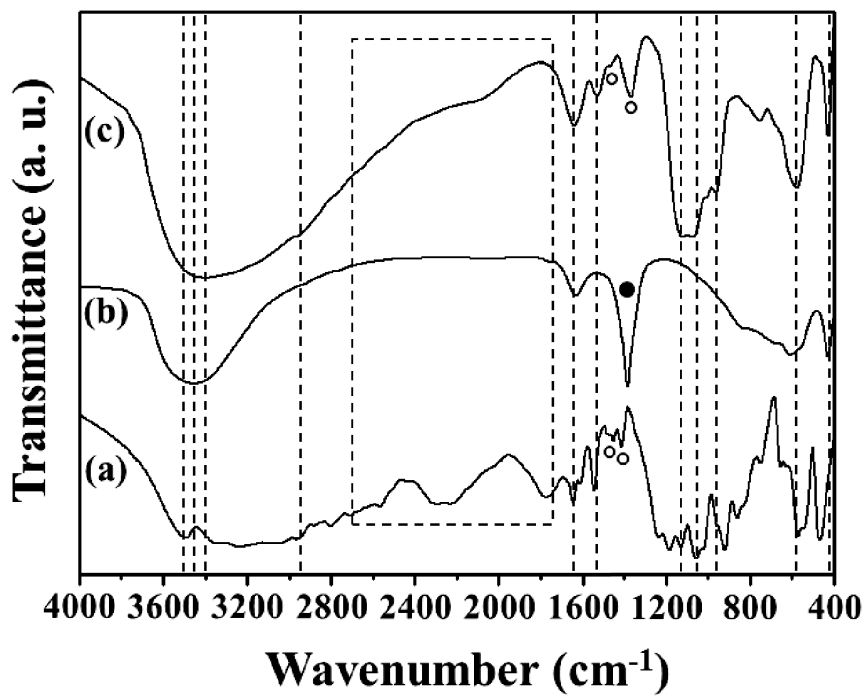


Figure 3.6. FT-IR spectra of (a) intact AL, (b) LDH-$NO_3$, and (c) AL-LDH.

### 3.4.4 Particle Analysis

FE-SEM images (Figures 3.7(A-B)) showed that both LDH-$NO_3$ and AL-LDH exhibited plate-like morphology with relatively homogeneous size of ~ 120 nm, indicating that the intercalative ion exchange reaction was successfully carried out without any change of morphology and particle size of LDH-$NO_3$. According to the DLS ananlysis (Figure 3.7(C)), the particle sizes were measured to be 118 ± 13 nm and 120 ± 11 nm for the LDH-$NO_3$ and AL-LDH, respectively, which were in good agreement with the FE-SEM data. Furthermore, as shown in Figure 3.7(D), the zeta potential of LDH-$NO_3$ was 35.1 ± 0.1 mV, indicating that LDH layers had a distinctive positive surface charge, but that of the AL-LDH was almost neutral (0.3 ± 0.15 mV). The positive surface charge of LDH layers were neutralized by the strong electrostatic interaction between the negatively charged AL and positively charged LDH layer.

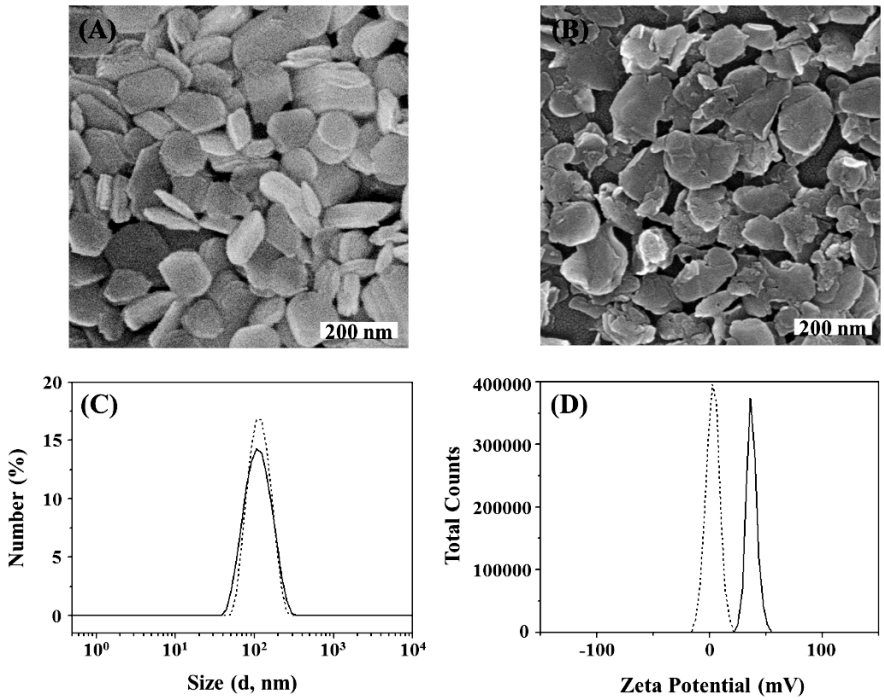


Figure 3.7. Particle analyses; FE-SEM images of (A) LDH-$NO_3$ and (B) AL-LDH. (C) Particle size distributions and (D) zeta potentials of LDH-$NO_3$ (solid line) and AL-LDH (dashed line), respectively.

### 3.4.5 UV-Vis Spectroscopy Analysis

The content of intercalated AL in the AL-LDH was determined through UV-Vis spectrophotometric analysis using $FeCl_3$ standard solution. Since AL do not possess an appreciable chromophore, AL was complexed with $Fe^{3+}$ ions under the acidic condition of 2 M $HClO_4$, in which the hydrolysis of $Fe^{3+}$ ions could be avoided.[88] The absorption spectra of base line (2 M $HClO_4$), intact AL, AL-LDH, $Fe^{3+}$ standard, and $Fe^{3+}$–AL complexes were recorded in the wavelength range from 200 to 400 nm (Figure 3.8(A)). There were no UV absorbances of intact AL and AL-LDH in the spectral region, while $Fe^{3+}$ standard and $Fe^{3+}$–AL complexes had the $\lambda_{max}$ absorption at 238 nm and at 260 nm, respectively. The absorbances of $Fe^{3+}$–AL complexes were read at 300 nm depending on the concentrations of AL to obtain a calibration curve of AL (Figure 3.8(B)). The content of intercalated AL in the AL-LDH was 26.5%, which was similar to theoretical AL content in the AL-LDH (26.3%). Briefly, it was determined on the basis of the net charge of AL (-2.54) calculated by its molar fractions ($AL^{2-}$ = 0.49 and $AL^{3-}$ = 0.49) at pH = 10.9, in which the AL-LDH was prepared. In addition, ICP-AES, and elemental CHN analysis were conducted in order to determine the chemical compositions of the LDH-$NO_3$ ($Zn_{0.67}Al_{0.33}(OH)_2(NO_3)_{0.33}\cdot 0.32H_2O$) and AL-LDH ($Zn_{0.68}Al_{0.32}(OH)_2AL_{0.13}\cdot 0.28H_2O$).

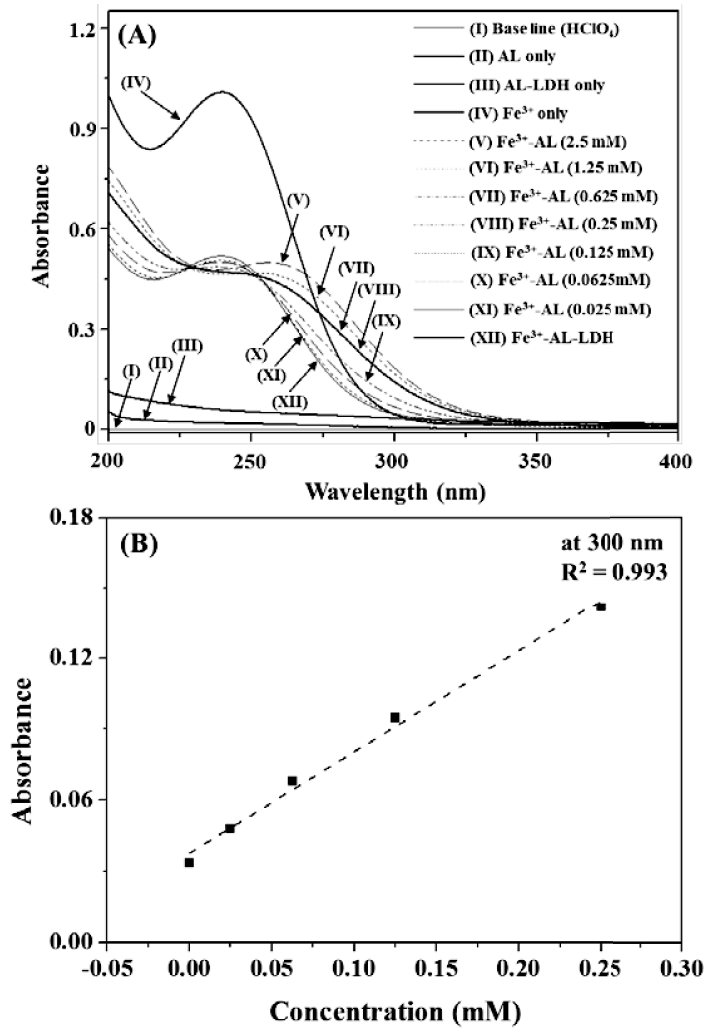


Figure 3.8. (A) Absorption spectra of (I) base line ($HClO_4$), (II) AL only, (III) AL−LDH only, (IV) standard $Fe^{3+}$ only, (V−XI) $Fe^{3+}$−AL complexes with different concentrations of AL, and (XII) $Fe^{3+}$−AL−LDH complex in 2.0 M $HClO_4$. (B) Absorbances of $Fe^{3+}$−AL complexes depending on the concentration of AL measured at 300 nm using UV−Vis spectroscopy.

### 3.4.6 *In vitro* Release Test

As shown in Figure 3.9, *in vitro* cumulative AL release profile of the AL-LDH in pH 7.4 PBS at 37° C showed substantially sustained release behavior of AL. At the initial stage, prevalent anions in PBS, such as anionic forms of phosphate and chloride, appeared to facilitate desorption of the adsorbed AL molecules on surface of the AL-LDH, resulting in slight initial burst release of AL. About 5% of AL was released out from the AL-LDH during first 2 days and another 4.5% of AL was very slowly released out until 100 days. More than 90% of AL still remained in the AL-LDH due to very strong electrostatic interaction between deprotonated AL molecules and LDH lattice.

The deprotonated phosphate group of AL molecules were stabilized on one side of LDH layers with strong electrostatic interaction, resulting in sustained release of AL from the AL-LDH. In addition, during ion-exchange of AL molecules at the layered edges with small anions in PBS, comparably smaller than AL molecules in size, zipping effect occurred and eventually retarded out-diffusion of intercalated AL molecules from the interlayer space of the AL-LDH.[17, 59]

In order to understand the release mechanism of AL from the AL-LDH, I fitted the observed release profile of AL-LDH to four kinetic models as shown in Figure 3.10. and the obtained rate constants ($k_d$) and $r^2$ values were summarized in Table 3.1. Among

the suggested release kinetic models, the first-order kinetic model, describing dissolution phenomena, showed poor $r^2$ value (0.66), which indicated that release of AL from the AL-LDH was not mainly dissolution determined process.[17] On the contrary, the parabolic diffusion model, modified Freundlich model, and Elovich model were well fitted to the observed release profile of AL with reliable $r^2$ values of more than 0.95. It is suggested that release process of AL from the AL-LDH is a kind of diffusion-controlled process or heterogeneous diffusion processes, including ion-exchange reaction between intercalated AL and anions in PBS medium.

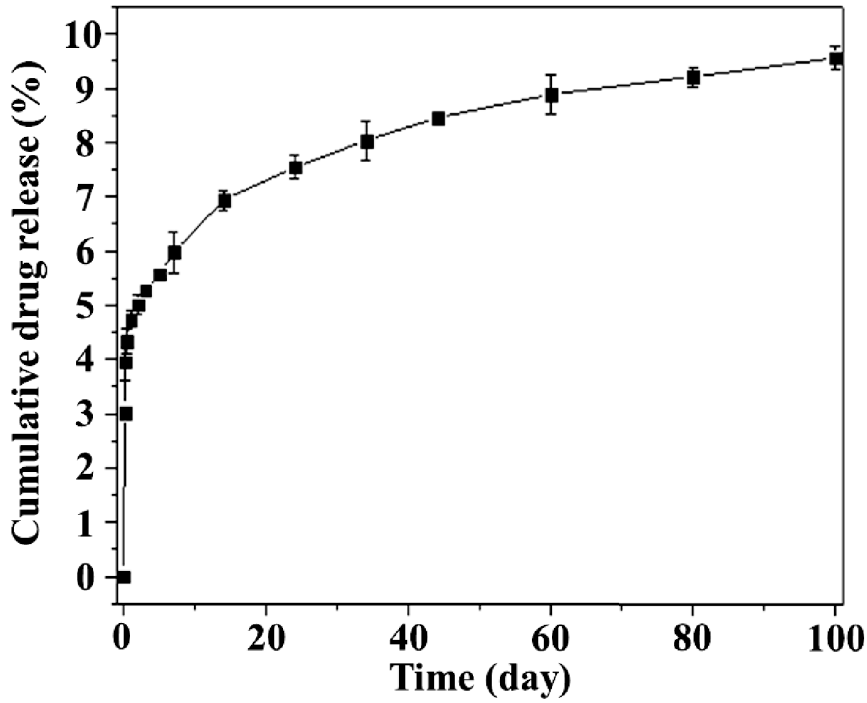


Figure 3.9. *In vitro* cumulative AL release profile of AL-LDH in pH 7.4 PBS

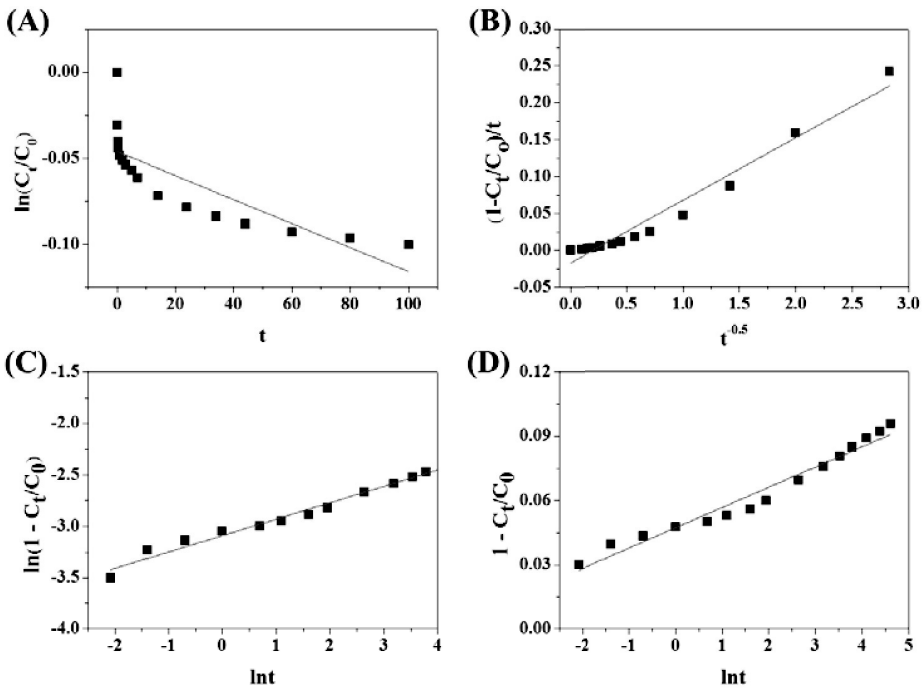


Figure 3.10. The plots of each kinetic equation based on (A) 1st order rate model, (B) parabolic diffusion model, (C) Freundlich model, and (D) Elovich model for the release of AL from the AL−LDH at pH 7.4 PBS media.

Table 3.1 Evaluated rate constants and $r^2$ coefficients based on the kinetic models.

| Constants | AL−LDH |
|---|---|
| First order : $\ln(C_t/C_0) = -k_d t$ | |
| $k_d$ | 0.0007 |
| $r^2$ | 0.6639 |
| Parabolic diffusion : $(1 - C_t/C_0)/t = k_d t^{-0.5} + a$ | |
| $k_d$ | 0.0863 |
| a | −0.0195 |
| $r^2$ | 0.9716 |
| Freundlich : $\ln(1 - C_t/C_0) = \ln(k_d) + a\ln t$ | |
| $k_d$ | 0.0456 |
| a | 0.1591 |
| $r^2$ | 0.9857 |
| Elovich : $1 - C_t/C_0 = a\ln t + b$ | |
| a | 0.0095 |
| b | 0.0471 |
| $r^2$ | 0.9641 |

$C_t$ = the amount of AL in the LDH at t min.
$C_0$ = the amount of AL in the LDH at 0 min.
$k_d$ = the rate constant of release, a, b, n = constant.

### 3.4.7 Cellular Uptake Studies

In order to verify efficient intracellular uptake behaviors of LDH, I quantified the accumulated concentrations of AL in MG63 cells depending on time. As shown in Figure 3.11, MG63 cells treated with the AL-LDH exhibited 10.6 times higher intracellular accumulation of AL than those treated with intact AL at incubation time of 1 h, indicating that LDH could facilitate permeation of AL into MG63 cells. Such improved intracellular uptake efficacy of AL with LDH was greatly superior to that with other AL delivery systems, such as chitosan coated polyethylene oxide microsphere and chitosan coated liposome, which showed approximately 3-fold and 2-fold increases, respectively.[3, 96] The concentration of AL in MG63 cells treated with the AL-LDH rapidly increased up to 1 h (11.16 μg/ml), which gradually decreased with time. Throughout all incubation periods, the AL-LDH exhibited much higher intracellular uptake efficacy than intact AL. From these results, I could expect that intact AL cannot be easily transferred into the cells due to repulsive interaction between the negatively charged membrane of the cell and anionic AL molecules, while the AL-LDH with a slightly positive charge can electrostatically interact with the cellular membranes, leading to favorable endocytosis *via* clathrin-mediated cellular uptake.[30, 32, 74] It is, therefore, LDH could act as an efficient drug delivery carrier to pass through the cell membrane.

Through CLSM images, I directly confirmed the penetration

of LDH into MG63 cells using FITC−LDH−$CO_3$. LDH−$CO_3$ was prepared by co−precipitation method and then labeled with FITC by surface adsorption to make FITC−LDH−$CO_3$. As shown Figure 3.12, PXRD patterns of (a) LDH−$CO_3$ and (b) FITC−LDH−$CO_3$ all exhibited a series of (00*l*) Bragg reflections, confirming the layered structure of LDH. The (003) Bragg reflection of FITC−LDH−$CO_3$ appeared at $2\theta$ = 11.6 corresponding to the basal spacing of 7.6 Å, which was identical to that of LDH−$CO_3$. Thus, it can be inferred that FITC was not intercalated into the interlayer space of LDH, but adsorbed on the surface of LDH. The full width at half maximum for each characteristic reflection of LDH−$CO_3$ and FITC−LDH−$CO_3$ was almost same, which suggested that there was no significant change in the crystallinity following adsorption of FITC onto LDH.

FE−SEM images in Figure 3.13(A) confirmed that the individual LDH−$CO_3$ was randomly dispersed and had average diameter of about 120 nm with a narrow particle size distribution. The image of FITC−LDH−$CO_3$ (Figure 3.13(B)) demonstrated a similar platelet size to that of LDH−$CO_3$ after adsorption of FITC. The average particle size (Figure 3.14(C)) measured by DLS was about 128 nm for LDH−$CO_3$, which then became 136 nm for FITC−LDH−$CO_3$, which was in good agreement with the FE−SEM data. As shown in Figure 3.13(D), the surface charge of FITC−LDH−$CO_3$ (5.25 ± 0.17 mV) was lowered by charge compensation between negatively charged FITC and LDH−$CO_3$ (34.1 ± 1.4 mV).

As shown in Figure 3.14(A), the green fluorescence was

observed throughout the cytoplasm of MG63 cells cultured with 20 μg/ml of the FITC−LDH−$CO_3$ for 1 h. On the contrary, the green fluorescence was not detected within the cells in the control experiment (Figure 3.14(B) and (c)), which was carried out with the centrifugal supernatant of the FITC−LDH−$CO_3$ and intact FITC solution, respectively. Given those, green fluorescence within the cells was not from the uptake of free FITC released from the FITC−LDH−$CO_3$, but from the uptake of the FITC−LDH−$CO_3$.

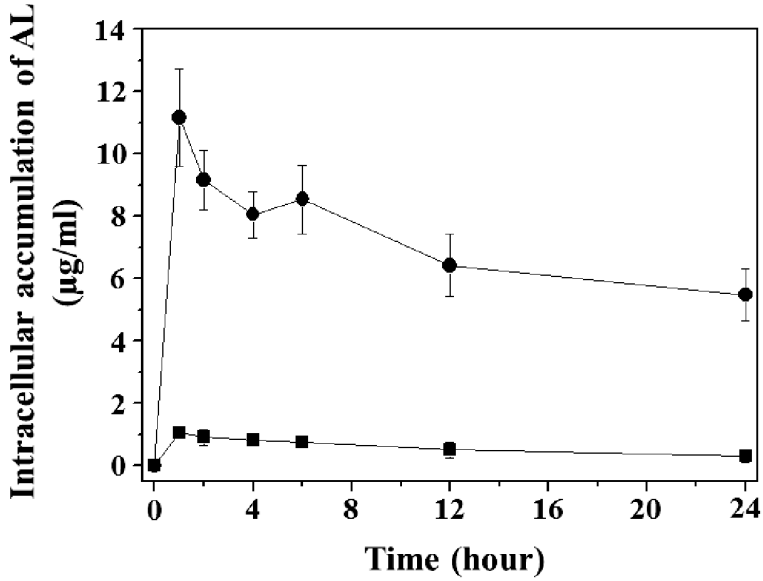


Figure 3.11. Cellular accumulation of AL molecules in MG63 cells treated with either AL (■) or AL−LDH (●).

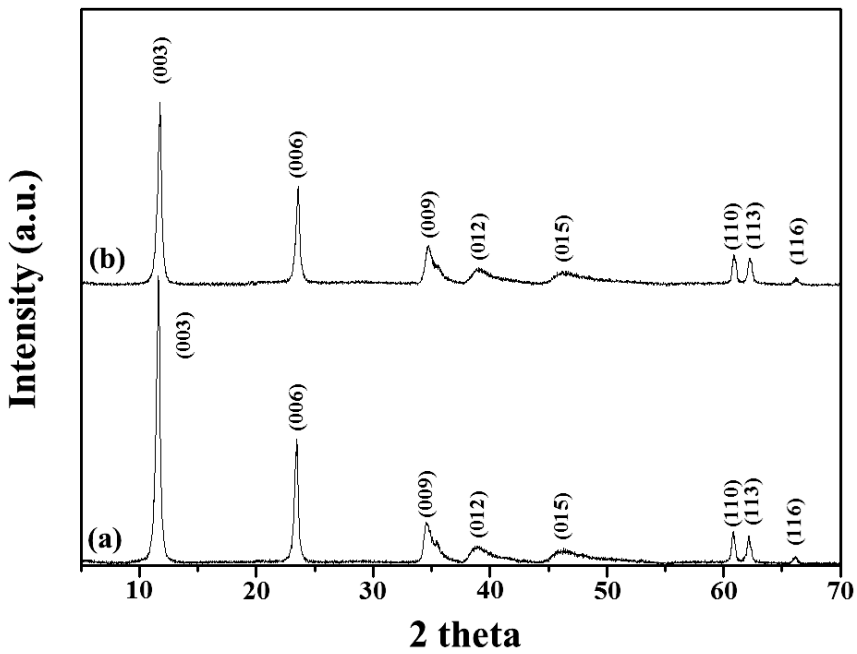


Figure 3.12. PXRD patterns of (a) LDH−$CO_3$ and (b) FITC−LDH−$CO_3$.

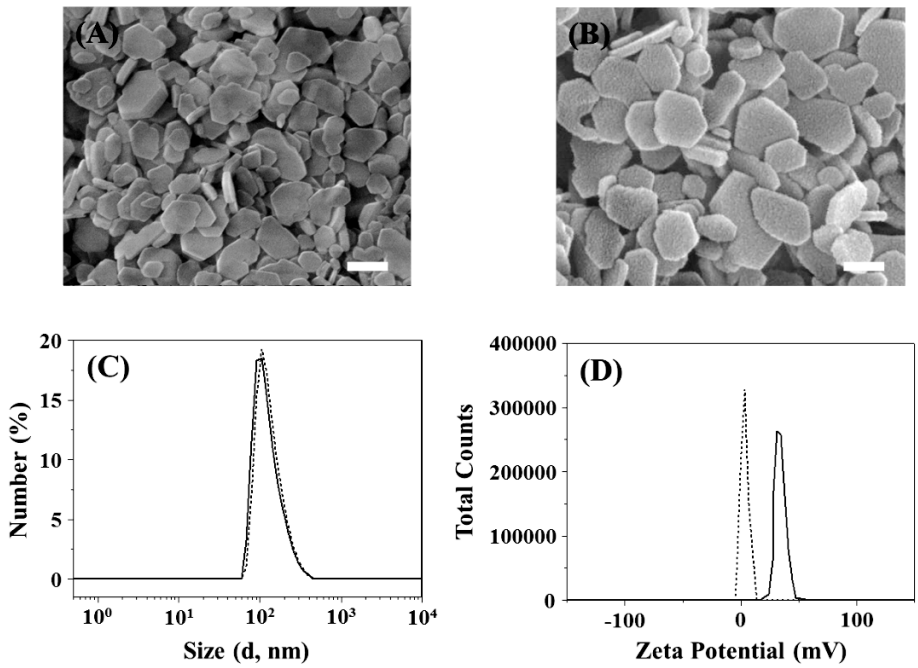


Figure 3.13. Particle analyses; FE-SEM images of (A) LDH-$CO_3$ and (B) FITC-LDH-$CO_3$. (C) Particle size distributions and (D) zeta potentials of LDH-$CO_3$ (solid line) and FITC-LDH-$CO_3$ (dashed line), respectively. The scale bars are 200 nm.

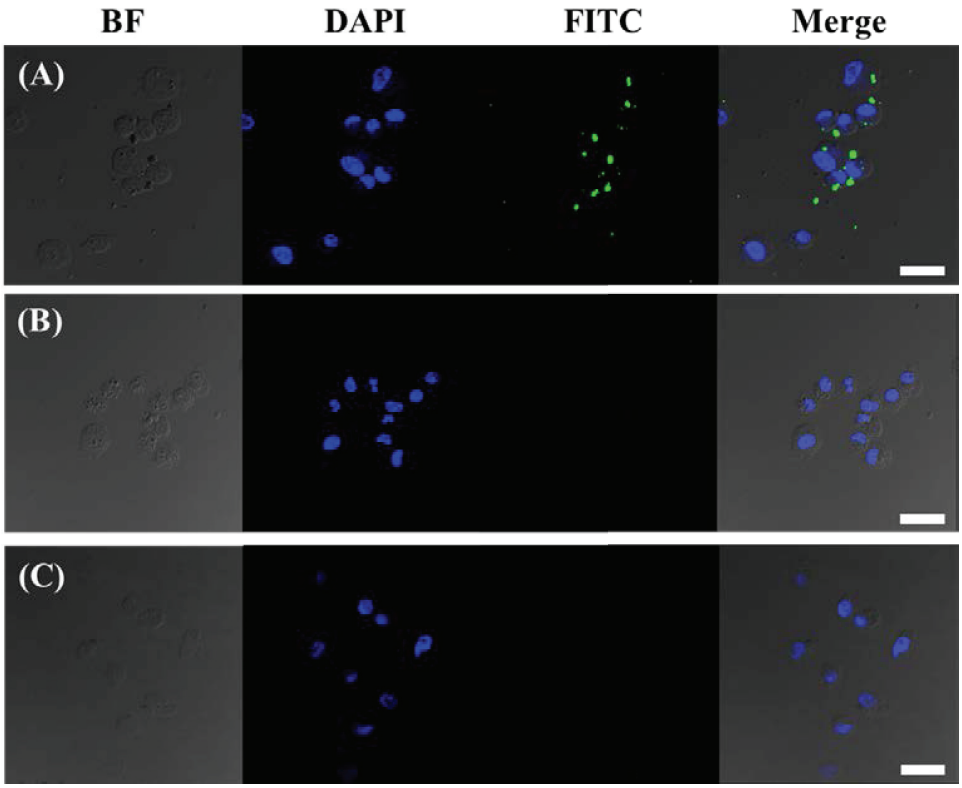


Figure 3.14. Confocal microscopic images of MG63 cells treated with (A) 20 μg/ml FITC-LDH-$CO_3$, (B) supernatant solution of 20 μg/ml FITC-LDH-$CO_3$, and (C) 20 μg/ml FITC.

### 3.4.8 *In vitro* Cell Proliferation and ALP Activity

I investigated effects of the AL-LDH on MG63 cells in terms of cell proliferation and osteogenic differentiation and compared the result with those from intact AL and LDH-$NO_3$. The cells treated with the osteogenic medium only were employed as control. It has been known that AL not only inhibits bone resorption [84], but also improves the recruitment, differentiation, and bone-remodelling activity of osteoblasts, thereby expediting bone repair.[83, 97]

*In vitro* proliferation level of MG63 cells was investigated using colorimetric CCK-8 assay, widely used for the determination of cell proliferation and cytotoxicity.[89] Both intact AL and AL-LDH showed higher proliferation of MG63 cells in all concentrations of AL during the whole tested periods, as compared to the LDH-$NO_3$ (Figure 3.15). The AL-LDH more enhanced proliferation than intact AL in all conditions. As shown in Figure 3.15(B), the highest cell proliferation was observed at $1\times10^{-8}$ M AL for both intact AL and AL-LDH, which were shown to be 29.8 and 59.8% above the negative control value, respectively. For the LDH-$NO_3$, no increase in cell proliferation was observed. For all tested samples, the cell proliferation was either increased or maintained, suggesting the AL-LDH be not cytotoxic, as well as the LDH-$NO_3$.

I also evaluated the efficacy of cell differentiation for the AL-LDH together with intact AL in terms of ALP activity, which is widely used as a marker for early differentiation of osteoblast-like cells to

demonstrate improved osteogenic activity.[82, 97] As can be seen in Figure 3.16, ALP activities of MG63 cells in the presence of LDH-$NO_3$, intact AL, or AL-LDH for 2, 3, and 4 days were evaluated. Both intact AL and AL-LDH showed higher ALP activities of MG63 cells than LDH-$NO_3$ and negative control in all conditions. Particularly, intact AL only at $10^{-8}$ M AL significantly increased ALP activities of MG63 cells on day 3 and 4, but the AL-LDH exhibited significant difference in ALP activity at any given concentrations of AL during whole tested periods as compared to LDH-$NO_3$ and negative control ($p < 0.05$). As shown in Figure 3.16(C), the highest increases in ALP activity of MG63 cells relative to that of negative control group were 12.4 and 29.1% at $10^{-8}$ M AL of intact AL and AL-LDH, respectively. Again, ALP activity did not appear to change much with LDH-$NO_3$, as well as with the control, at all concentrations.

When the same dose of AL was applied, both *in vitro* cell proliferation and ALP activity were more efficiently improved with the AL-LDH than intact AL. This could be ascribed to facilitated intracellular uptake of AL-LDH: unlike negatively charged AL molecules, the AL-LDH was positively charged (0.3 ± 0.15 mV), which could be attracted to negatively charged cellular membranes, leading to favorable endocytosis *via* clathrin-mediated cellular uptake.[32, 74] Although LDH-$NO_3$ itself had no effect on the cell proliferation and osteogenic differentiation, a combined entity of AL and LDH, AL intercalated LDH nanohybrid, could be considered as a novel drug delivery system for improving efficacy of AL.

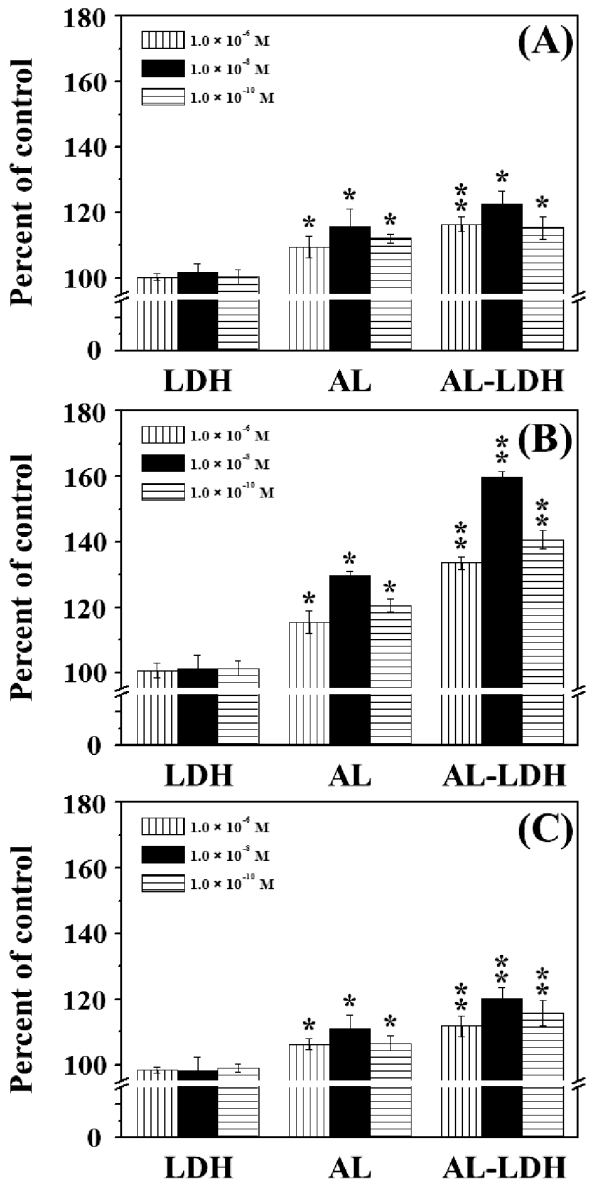


Figure 3.15. *In vitro* proliferation of MG63 cells treated with osteogenic media containing different concentrations of LDH−$NO_3$, intact AL, and AL−LDH for (A) 2, (B) 3, and (C) 4 days. All experiments were performed at least three times for statistics. *Intact AL or AL−LDH was significantly different from LDH−$NO_3$ ($p < 0.05$). **AL−LDH was significantly different from both LDH−$NO_3$ and intact AL ($p < 0.05$).

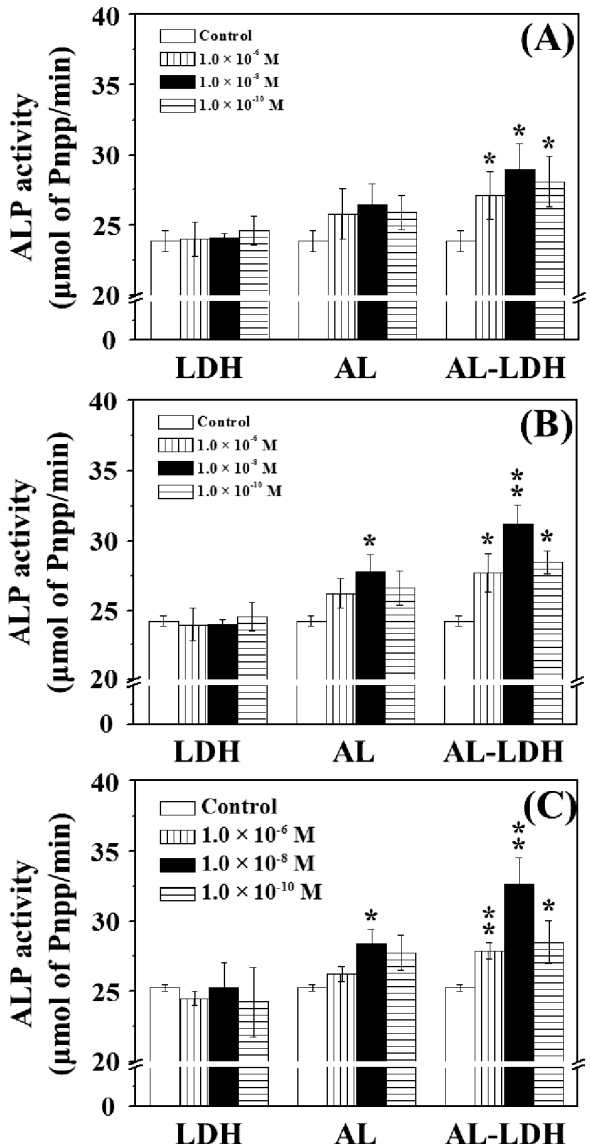


Figure 3.16. *In vitro* alkaline phosphatase activity (ALP) activity of MG63 cells treated with osteogenic media containing different concentrations of LDH−$NO_3$, intact AL, and AL−LDH for (A) 2, (B) 3, and (C) 4 days. All experiments were performed at least three times for statistics. *Intact AL or AL−LDH was significantly different from both negative control and LDH−$NO_3$ ($p < 0.05$). **AL−LDH was significantly different from the other groups ($p < 0.05$).

## 3.5 Conclusion

In this study, I have successfully synthesized the X-ray single phasic AL-LDH with nanosized plate-like morphology by ion-exchange reaction in order to enhance the efficacy of AL. According to the cellular uptake studies, the intracellular accumulation of AL in MG63 cells treated with the AL-LDH was 10.6-fold higher than that with intact AL for 1 h treatment. From the CLSM images, the ease of internalization of LDH was confirmed as the green fluorescence within the cells was not from the uptake of free FITC released from the FITC-LDH-$CO_3$, but from the uptake of the FITC-LDH-$CO_3$ itself. Furthermore, *in vitro* cell proliferation and ALP activity results showed that the incorporation of AL into LDH could enhance efficacy of AL compared to intact AL, although LDH itself had no effect on proliferation and osteogenic differentiation of MG63 cells. Therefore, the present AL-LDH could be considered as a promising drug delivery system for improving efficacy of AL.

# Part III.

# Layered Double Hydroxide Based Nanohybrid as Diagnostic Agent

# Chapter 4

## X-ray Visible Bioabsorbable Bone Fixation Plate *via* Various Layered Metal Hydroxides

### 4.1 Abstract

Biodegradable polymer plates can be clinically used as an alternative to metal plates (e.g., titanium) for internal fixation, which, however, are not visible with X-ray for post-operative diagnostics. Thus, in this study, to allow X-ray visibility, I separately prepared

radiopaque sheets and attached them onto a bioabsorbable bone plate approved for clinical use. The radiopaque sheets were each made of a fine powder of layered metal hydroxides (LMHs) as radiopaque agents and poly (lactic-co-glycolic acid) (PLGA) as a biodegradable binder material, which were physically mixed without any changes in their chemical structure. In this study, I employed LMHs such as Ca-Fe hydrocalumite, Mg-Al or Zn-Al layered double hydroxide, and Zn hydroxyl double salt in order to modulate the degree of X-ray visibility. All radiopaque plates herein were visible *via* X-ray and their radiopacity increased as metals with higher X-ray attenuation coefficients in LMHs were used. According to the *in vitro* X-ray visibility test, all radiopaque plates were discernible for 42 days and showed the decrease in visibility with time regardless of chemical compositions in LMHs. The PLGA incorporated into the radiopaque sheet caused swelling and degradation, leading to the release of LMH particles and the decrease of density of the sheet attached onto the fixation plate. The *in vivo* study with rats revealed that a discernible image of the radiopaque plate could be obtained by X-ray, also showing the overall biocompatibility at 42 days after implantation. Therefore, the radiopaque fixation plate, prepared in this work, is a promising fixation device enabled with X-ray visibility, biodegradability, and biocompatibility.

## 4.2 Introduction

Internal bone fixation devices are widely used in orthopedic clinical practices to avoid undesired motions of fractured bones until healing is complete.[99, 100] Therefore, metallic fixation devices are used to provide enough mechanical strength to hold the fractured bone in place.[101] However, the metallic fixation devices often need a secondary removal surgery, thereby causing low compliance to patients. In this respect, the fixation devices made of bioabsorbable polymers, such as poly(lactic-co-glycolic acid) (PLGA), poly(lactic acid), poly(glycolic acid), or poly(trimethylene carbonate),[99, 102-105] can replace the metallic ones to treat the injured bones where a high mechanical load is not required.[106, 107] The gradually lessened strength by biodegradation can minimize stress shielding, resulting in a formation of dense bone.

For successful treatment of fractured bone, adequate positioning of the fixation devices is mandatory to minimize gap formation within the bone fracture, which needs to be monitored after implantation not only to prevent undesired loosening and motion of those devices in the fractured bone position before completely bone healing, but also to avoid retarded healing and infection. This can be performed noninvasively by conventional X-ray imaging for the metallic devices, which, however, is not possible with the bioabsorbable device due to its inherent radiolucent property.[108, 109] Despite of diverse clinical advantages of biodegradable polymer

fixation plate, those biodegradable plates used for the fixation are not visible with X-ray imaging, which would hinder surgeons from verifying the proper positioning of the fixation devices.

For this reason, a bioabsorbable fixation device can be more beneficial when enabled with diagnostic functionality (i.e., X-ray visibility). Previously, in order to allow X-ray visibility, polymeric bone cements, plates, or dental resins were combined with traditional radiopaque additives, such as iodine[109, 110] and bismuth,[109, 111] but those devices often lose mechanical strength and toughness.[114] Additionally, those kinds of additives can cause toxicity if released into the body.[109, 111] Thus, currently, there are many attempts to minimize toxicity by combining biocompatible ceramic materials, such as $\beta$-tricalcium phosphate (TCP) and barium sulfate.[115, 116] Previously, I had separately prepared radiopaque sheets, each composed of TCP or barium sulfate and poly(lactic-co-glycolic acid) (PLGA), and attached to a biodegradable bone plate already in clinical use.[117, 118] The positioning of the plate could be monitored *via* X-ray for a period of clinical need, and the sheet was also able to gradually degrade without compromising the biocompatibility of the original bone plate. However, the discernibility of the TCP sheet *via* X-ray imaging *in vivo* was not satisfactory due to the relatively low X-ray attenuation coefficient of calcium in TCP. For the radiopaque sheet possessing barium sulfate with higher X-ray attenuation coefficient than TCP, X-ray visibility was highly enhanced, but there is still concern about

toxicity of barium sulfate when exposed inside the body.[119]

To address these shortcomings, I employ biodegradable and biocompatible layered metal hydroxides (LMHs) as alternative materials in order to prepare radiopaque sheets enabled with diagnostic advantages (i.e., X-ray imaging), which could be integrated with a bioabsorbable bone fixation device in clinical use, since metal hydroxide layers of LMHs are made of metals with high X-ray absorption. LMHs can be classified into three categories according to the structure and metal-ligand coordination type. One is hydrocalumite (HC) structure having chemical formula $[Ca_2M^{3+}(OH)_6]^+(A^{n-})_{1/n} \cdot mH_2O$ (M: trivalent metal, A: interlayer guest anion).[120] Upon characteristics of structural feature, the HC has distinctive structure resulted from relatively large size of $Ca^{2+}$ (~99 pm) in the structure; hepta-coordinated calcium hydroxide decahedrons and hexa-coordinated trivalent metal hydroxide octahedrons are arranged in 2-dimensional lattice by sharing edges. Another type is a layered double hydroxide (LDH) which can be represented by a general formula of $[M^{2+}_{1-x}M^{3+}_x(OH)_2]^{x+}(A^{n-})_{x/n} \cdot mH_2O$ ($M^{2+}$: divalent metal, $M^{3+}$: trivalent metal, A: interlayer guest anion, $0 < x < 1$, m and n are integers).[11, 15, 19, 26, 29] The divalent cations in a brucite-like lattice by sharing edges are isomorphously substituted by trivalent ones, resulting in positive layer charge, which is counter balanced by anions located in the interlayer region. The other one is hydroxy double salt (HDS), represented by a general chemical formula of $[(M_{1-x}M'_{1+x})(OH)_3]^+$

$(A^{n-}_{1/n}) \cdot mH_2O$ (M and M' : divalent metals, A: interlayer guest anion, $0 < x < 1$, m and n are integers).[17, 59] In this structure, edge-shared array of metal hydroxide octahedrons make periodic vacant sites, of which upper and down positions are occupied by metal hydroxide tetrahedrons to produce positively charged hydroxide layer. All those LMHs can work as radiopaque materials since di- and trivalent metals with higher X-ray attenuation coefficients, such as magnesium (0.1686 $cm^2/g$), aluminum (0.1704 $cm^2/g$), calcium (0.2571 $cm^2/g$), iron (0.3717 $cm^2/g$), and zinc (0.4973 $cm^2/g$), are located in LMH lattice than carbon (0.1514 $cm^2/g$), which is the main source of bioabsorbable polymeric plate.[23-25] In addition, the LMHs have been proven biodegradable and biocompatible to a large extent according to many previous studies.[33, 54, 55, 121]

In this work, I fabricated radiopaque bone plates containing LMHs, such as Ca-Fe hydrocalumite (CaFe-HC), Mg-Al or Zn-Al layered double hydroxide (MgAl-LDH or ZnAl-LDH, respectively), and Zn hydroxyl double salt (Zn-HDS) prepared by co-precipitation, in order to modulate the degree of X-ray visibility. I separately prepared radiopaque sheets made of a blend of LMHs and poly(lactic-co-glycolic acid) (PLGA), a binder material known to possess high biocompatibility[122] and degrade both by hydrolysis and enzymatic processes in the body[123]. Each sheet was then attached onto a biodegradable bone plate (PLT-1031, Inion, Finland) in clinical use.[117, 118] In such a way, the prepared plates could be

X-ray visible due to the presence of metals in LMH. PLGA in the sheet would be degraded to free LMHs, which would also allow gradual disappearance of the sheet like the bioabsorbable plate used herein.

The radiopaque bone plates containing LMHs were characterized by powder X-ray Diffraction (PXRD), Fourier transform infrared spectroscopy (FT-IR), field emission scanning electron microscopy (FE-SEM), and thermogravimetric analysis (TGA) in order to investigate its structural and physicochemical properties. I performed the *in vitro* immersion test in simulated physiological condition to examine the changes in X-ray visibility of the radiopaque plates with time. To examine cytotoxicity, the plates were assessed using L929 mouse fibroblasts. For *in vivo* evaluation, the plates were inserted into subpanniculus pockets of rats and imaged *via* X-ray at scheduled intervals for 42 days following implantation. For biocompatibility evaluation, the histopathologic analyses were performed using tissue samples around the plates obtained at 42 days after implantation.

## 4.3 Experimental Section

### 4.3.1 Materials

Magnesium chloride hexahydrate ($MgCl_2 \cdot 6H_2O$), aluminum chloride hexahydrate $AlCl_3 \cdot 6H_2O$), calcium chloride dehydrate ($CaCl_2 \cdot 2H_2O$), iron chloride ($FeCl_3$), zinc chloride ($ZnCl_2$), and sodium hydroxide (NaOH) were obtained from Sigma (MO, USA). PLGA (lactic acid:glycolic acid (50:50); average molecular weight 4.1 kDa; intrinsic viscosity = 0.08 dL/g) and dimethylformamide (DMF) were purchased from Lakeshore Biomaterials (AL, USA) and J.T. Baker (PA, USA), respectively. Bioabsorbable bone fixation plate (PLT-1031), composed of poly(trimethylene carbonate), polylactide, and polyglycolide, was obtained from Inion (Finland). PBS (pH 7.4) was supplied from Seoul National University Hospital Biomedical Research Institute (Korea). Roswell Park Memorial Institute (RPMI) medium, penicillin streptomycin, fetal bovine serum (FBS), 0.25% Trypsin-EDTA (1X), and Dulbecco's Phosphate-buffered saline (DPBS) were purchased from Gibco (Life Technologies, UK). A cell counting Kit-8 [89] (CCK-8, DOJINDO, Japan) was used following the manufactures' instruction. Zolazepam and tiletamine (Zoletil®) were supplied from Virbac (France) and xylazine (Rompun®) was from Bayer (Germany). The bioabsorbable suture (Vicryl 4-0) was supplied from Ethicon (Cornelia, GA, USA).

### 4.3.2 Preparation of LMHs

For CaFe-HC, 10 mM of $Ca(Cl)_2 \cdot 2H_2O$ and 5 mM of $FeCl_3$ were dissolved in 250 ml decarbonated water by vigorous agitation for 0.5 h until the solution became transparent. Then, the mixed metal solution was co-precipitated by adjusting pH to 12.5 with a 0.5 M NaOH solution. For MgAl-LDH and ZnAl-LDH, mixed metal solution of $M^{2+}/Al^{3+}$ ($M^{2+}$ ($Mg^{2+}$ or $Zn^{2+}$): 10 mM, $Al^{3+}$: 5 mM) in 250 ml decarbonated water was titrated with the NaOH solution and the pH of each metal solution was adjusted to 10.0 for MgAl-LDH and 8.0 for ZnAl-LDH, respectively. For Zn-HDS, 10 mM $ZnCl_2$ in 250 ml decarbonated water was coprecipitated by titrating with NaOH solution to pH 7.0. All coprecipitated LMHs were aged for 24 h at room temperature. The resulting precipitates was centrifuged, washed three times with decarbonated water to eliminate unreacted ions, and freeze-dried. All the reactions were performed under nitrogen atmosphere to avoid carbonate contamination.

### 4.3.3 Preparation of Radiopaque Bone Plates

I first fabricated bioabsorbable and radiopaque sheets containing LMHs following previous works.[117, 118] A sheet of poly(methyl methacrylate) (PMMA; EunSung Polytechnology, Korea), 2.0 mm in thickness, was cut into pieces to form a square-shaped frame (outer edge: 6.5 mm; side of a square hole: 1.0 mm), using a $CO_2$ laser (FC-200RA LASER Machinery, South Korea). The resulting piece was

used to make a substrate of polydimethylsiloxane (PDMS) (Sylgard®184, Dow Corning, MI). To prepare a LMH sheet, each fine powder of LMH (150 mg) was physically mixed with 100 $\mu$l of a PLGA solution in DMF (30% w/v), which was then densely packed into the wells in the PDMS substrate and lyophilized for 1 day. I fabricated four distinct sheets: a 2.0-mm thick CaFe-HC sheet, MgAl-LDH sheet, ZnAl-LDH sheet, and Zn-HDS sheet. For all sheets, the mass ratio of PLGA and LMH was 1:5.

To prepare a bone plate enabled with X-ray visible functionality, I attached the resulting each LMH sheet on the surface of a bioabsorbable Inion bone plate. In this work, a whole piece of an Inion bone plate was cut into 6.5 mm × 6.5 mm square-shaped pieces, each with a screw hole at the center. Then, PLGA solution in DMF (30% w/v) was sprayed on the top of the plate under the following condition: diameter of nozzle orifice: 0.5 mm, spraying pressure: 15 psi, spraying time: 2 s, spraying distance: 15 cm. Right after that, the each type of LMH layer was placed and bonded with the plate. The resulting functional plate was then lyophilized for 1 day to eliminate residual solvent. In this present work, I prepared five different types of the plates, as listed below:

(1) UP: unmodified bioabsorbable bone plate

(2) CaFe-HC_P: bioabsorbable bone plate attached with a 2.0-mm thick CaFe-HC sheet

(3) MgAl-LDH_ P: bioabsorbable bone plate attached with a 2.0-mm thick MgAl-LDH sheet

(4) ZnAl-LDH_P: bioabsorbable bone plate attached with a 2.0-mm thick ZnAl-LDH sheet

(5) Zn-HDS_P: bioabsorbable bone plate attached with a 2.0-mm thick Zn-HDS sheet

### 4.3.4 Characterizations

The structural analysis was carried out using PXRD (D/MAXRINT 2200-Ultima, Rigaku, Japan) equipped with Ni-filtered Cu-K$\alpha$ radiation ($\lambda$ = 1.5418 Å). FT-IR spectra were obtained by the potassium bromide pellet method using a spectrophotometer (JASCO FT-IR 6100, Japan). The images of the LMH plates were obtained *via* FE-SEM (JSM-6700F, JEOL, Japan). Before imaging, the sample was sputter-coated with platinum (208HR, Cressington Scientific, UK). The elemental analysis (EA1110, CE instrument, Italy) and inductively coupled plasma atomic emission spectroscopy (ICP-AES, Optima-4300 DV, PerkinElmer, USA) were carried out to assess the chemical compositions of LMHs.

### 4.3.5 *In vitro* X-ray Visibility Test

To evaluate X-ray visibility of functional plates herein, each of CaFe-HC_P, MgAl-LDH_P, ZnAl-LDH_P, and Zn-HDS_P was immersed in 10 ml PBS and then agitated at 125 rpm at 37° C in a shaking incubator. At scheduled times for 28 days, the sample was

imaged, using a mobile C-arm (BV Pulsera, Philips, Netherlands) with a charging voltage of 55 kV. For each image, densitometry measurement was carried out using ImageJ software (National Institutes of Health, MD, USA), as previously reported.[124] At least three batches were assessed for each sample type.

### 4.3.6 *In vitro* Cell Study

*In vitro* cell viability of LMHs was assessed on L929 mouse fibroblasts cells (Korean Cell Line Bank, Korea). The cells were grown in RPMI medium supplemented with 10% heat inactivated fetal bovine serum, 100 units/ml penicillin, and 100 μg/ml streptomycin. The cells were seeded onto 96-well plates with a density of $5.0 \times 10^3$ cells/well and incubated overnight at 37° C under 5% $CO_2$ atmosphere. The medium in a well was then replaced with the fresh cell medium containing LMHs. In order to evaluate the cell viability, the concentrations of LMHs were varied in the range of 1-500 μg/ml.

I also performed the extraction method to examine the cytotoxic effect of the dissolved metal ions and released LMH particles from the radiopaque LMH plates.[118] The CaFe-HC_P, MgAl-LDH_ P, ZnAl-LDH_P, and Zn-HDS_P were each placed in 2 mL of immersion medium (the same medium used for cell culture) and incubated with continuous shaking (125 rpm) at 37° C (SI-600R, Jeio Tech, Korea). All plates were sterilized prior to the test using ethylene oxide gas. Every 2 days, the entire 2 mL of immersion

medium was withdrawn to collect the extract medium, and an equal volume of the fresh medium was added back. For four types of plates, the extract media were obtained on days 1, 3, 7, 14, 21, 30, and 42 for cytotoxicity evaluation. L929 fibroblast cells were seeded at a density of $5.0 \times 10^3$ cells/well on a 96-well cell culture plate under the same incubation condition. Subsequently, the entire 100 μl of the culture medium from each well was replaced with an equal volume of the obtained extract medium and then the cells were incubated for another 24 h. The intact cell medium was used for negative control. Following treatments, *in vitro* cell viability was assessed using Cell Counting Kit-8 (CCK-8), following the manufacturer's instruction. Briefly, CCK solution (200 μl) was added to each well and further incubated for 3 h at 37° C. The optical absorbance of each well was recorded at 450 nm on a micro-plate reader (Multiskan FC, Thermo Scientific, USA), and expressed in percentage based on optical density of the negative control. The assay was performed at least five times for statistics.

### 4.3.7 *In vivo* Animal Study

For *in vivo* study, 8-week-old male Sprague-Dawley (SD) rats, weight 260-330 g (Koatech, Korea) were individually housed with free access to water and food during the entire experimental period. All experimental procedures were approved by the Institutional Animal Care and Use Committee (IACUC No. 13-0120)

at Seoul National University Hospital. For the LMH plates insertion, (a) the SD rats were each anesthetized using an intraperitoneal injection of a cocktail of Rompun® (0.1 ml/kg) and Zoletil® (0.3 ml/kg) (1:1, v./v.). Then, the hair on the dorsal area was shaved. (b) Before incision, the surgical site was marked with a surgical pen. (c) 3 cm of incision was made along the vertebra using a surgical scissor to obtain a pocket in subcutaneous tissue. (e) The each of LMH plates was inserted in the pocket. (f) The incision was closed with nylon 4-0 thread, and the surgical site was disinfected again with Betadine. At least four animals were assessed for each of the animal groups. In this work, I prepared five distinct animal groups.

(1) UP group: the animals implanted with the UP

(2) CaFe-HC_P group: the animals implanted with the CaFe-HC_P

(3) MgAl-LDH_ P group: the animals implanted with the MgAl-LDH_P

(4) ZnAl-LDH_P group: the animals implanted with the ZnAl-LDH_P

(5) Zn-HDS_P group: the animals implanted with the Zn-HDS_P

#### 4.3.7.1 *In vivo* X-ray Visibility

To evaluate *in vivo* X-ray visibility following the plate implantation, the marked surgical area of SD rats were imaged using a mobile C-arm (BV Pulsera, Philips, Netherlands) in manual mode with a charging voltage of 55 kV. For imaging, the rats were put under temporary anesthesia with intraperitoneal injection of a cocktail of Zoletil® and Rompun®. The images were obtained at scheduled times

of 1, 3, 7, 14, 21, 28, and 42 days after implantation. Each X-ray image was quantitatively analyzed with densitometry measurements, using ImageJ software (National Institutes of Health, MD, USA).[124]

#### 4.3.7.2 Histologic Evaluation

At 42 days after plate implantation, four rats per group were placed under deep anesthesia *via* intraperitoneal injection of Zoletil® (1 ml/kg) and sacrificed *via* intravenous injection of 10 ml of 15% w/v potassium chloride. Then, the tissues around the plates were biopsied in order to assess *in vivo* biocompatibility of the plates herein. The obtained tissue samples were each fixed in fresh 10% (v/v) buffered neutral formalin for 3 days and embedded within resin, which were then sectioned into 30-40 $\mu$m thick slides (BS-3000N, EXAKT, Germany). The slides were then stained with hematoxylin-eosin (H&E) and examined under an optical microscope (BX53F, OLYMPUS, Japan) with X100 magnification for histologic evaluation by a professional pathologist.

### 4.3.8 Statistical Analysis

*In vitro* cell viability, *in vitro* X-ray visibility, and *in vivo* X-ray visibility were statistically analyzed with one-way analysis of variance (ANOVA) with $\alpha = 0.05$ followed by pairwise comparisons using a Tukey's post hoc test (GraphPad Prism, version 5.01, USA). $p < 0.05$ was considered statistically significant.

## 4.4 Results and Disucussion

### 4.4.1 Structural and Element Analysis of LMHs

According to the PXRD shown in Figure 4.1, the diffraction patterns of all synthesized LMHs have the characteristic reflections corresponding to well crystalline layered phases exhibiting well developed (00*l*) diffractions patterns. According to the Bragg' s equation, (002) peak of CaFe-HC at 11.2 in 2 $\theta$ and (003) peaks of MgAl-LDH, ZnAl-LDH, and Zn-HDS at 11.3 in 2$\theta$ indicate the d-spacing of 7.9 Å for CaFe-HC and 7.8 Å for the other LMHs, respectively, which were well consistent with the previous reports.[19, 38, 50, 59] In addition, ICP-AES, elemental CHN analysis, and TGA were conducted in order to determine the chemical compositions of CaFe-HC ($Ca_{0.67}Fe_{0.33}(OH)_2(Cl)_{0.33}\cdot 0.34H_2O$) and MgAl-LDH ($Mg_{0.67}Al_{0.33}(OH)_2(Cl)_{0.33}\cdot 0.19H_2O$), ZnAl-LDH ($Zn_{0.67}Al_{0.33}(OH)_2(Cl)_{0.33}\cdot 0.42H_2O$), and Zn-HDS ($Zn_{5.0}(OH)_8(Cl)_{2.0}\cdot 1.71H_2O$).

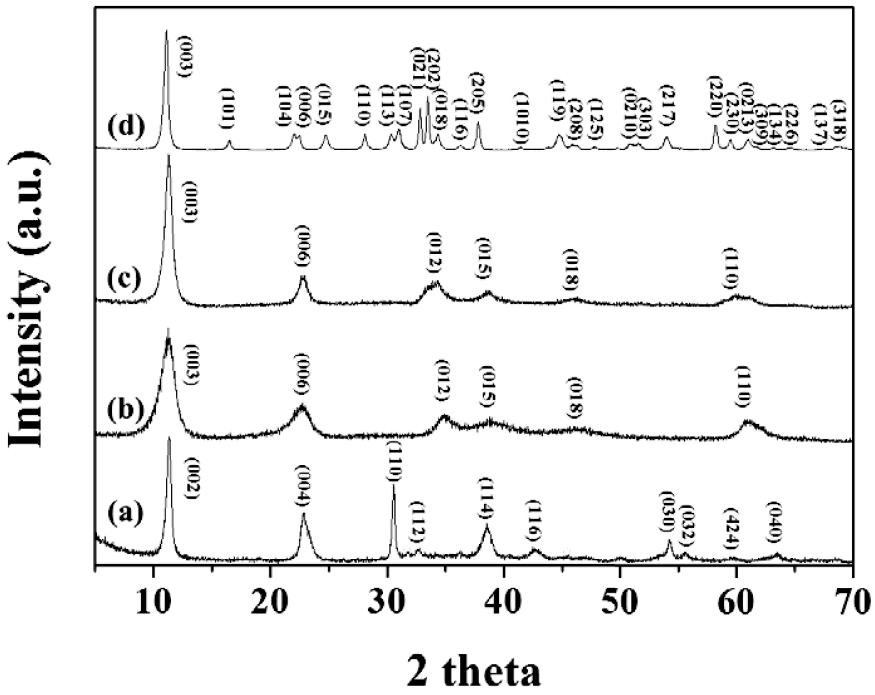


Figure 4.1. (A) PXRD patterns of (a) CaFe-HC, (b) MgAl-LDH, (c) ZnAl-LDH, and (d) Zn-HDS.

### 4.4.2 Characterization of the Radiopaque LMH Sheets

In this work, to vary the degree of X-ray visibility, I prepared four distinct radiopaque sheets: a 2.0-mm thick CaFe-HC sheet, MgAl-LDH sheet, ZnAl-LDH sheet, and Zn-HDS sheet. For all sheets, the mass ratio of PLGA and each type of LMH was 1:5, confirmed by TGA in Figure 4.2. The difference of weight loss (%) at 800℃ between each type of LMH and LMH sheet bound with PLGA was approximately 16.6 %, which was well consistent with the feeding mass ratio. Figure 4.3(A) depicts an whole intact bioabsorbable bone plate (PLT-1031, Inion, Finland) used in this work and Figure 4.3(B) shows its piece (6.5 mm × 6.5 mm).

On the top of this plate, I attached the radiopaque LMH layer, composed of PLGA and each type of LMH [Figure 4.3(B)(b-e)]. The sheet was designed to possess a frame shape with a square hole at the center in order to leave the screw hole already present in the original bone plate undisturbed. Through FE-SEM images as shown in Figure 4.4, the LMH particles in the radiopaque layers were observed to be bound with PLGA with fairly homogeneous distribution. I clearly confirmed that LMH possessed plate-like morphology with primary particle size of several hundred nanometers ((100-200 nm)) for the CaFe-HC, MgAl-LDH, and ZnAl-LDH or several micrometers for Zn-HDS (1-5 μm).

I performed PXRD and FTIR analyses on the radiopaque LMH layers. As displayed in Figure 4.5, the intact PLGA exhibited no

PXRD peaks due to its amorphous structure[125, 126] and the characteristic PXRD peaks from the LMH itself were also observed in each type of LMH sheet. This result indicated the presence of crystalline LMHs in the radiopaque layer.

As I examined the FTIR spectra (Figure 4.6), the intact PLGA exhibited a strong band at 1750 $cm^{-1}$ from the C=O stretching in carbonyl group, bands at 2955 and 2998 $cm^{-1}$ from the C−H stretching in $-CH_2$ group, and the band at 3743 $cm^{-1}$ from O−H stretching vibration.[126] The absorption bands at 1270 and 1176 $cm^{-1}$ were associated with the C–O stretching of the ester group and at 1395–1455 $cm^{-1}$ was ascribed to C−H bending vibrations. The pristine LMH displayed characteristic peaks ranging from 3400 to 3500 $cm^{-1}$ and from 1600 to 1650 $cm^{-1}$ due to O−H stretching of the hydroxide layer vibration and interlayer water in LMH, respectively. The absorption bands observed in the low frequency region below 800 $cm^{-1}$ were attributed to lattice vibration modes such as M−O and M−O−M (M: metals, such as Mg, Al, Ca, Fe, and Zn) vibrations. All of the characteristic bands from PLGA and each pristine LMH were overlapped within those from each LMH layer, revealing that the composing materials, LMH and PLGA, were physically mixed to form a layer without changing their individual chemical properties.

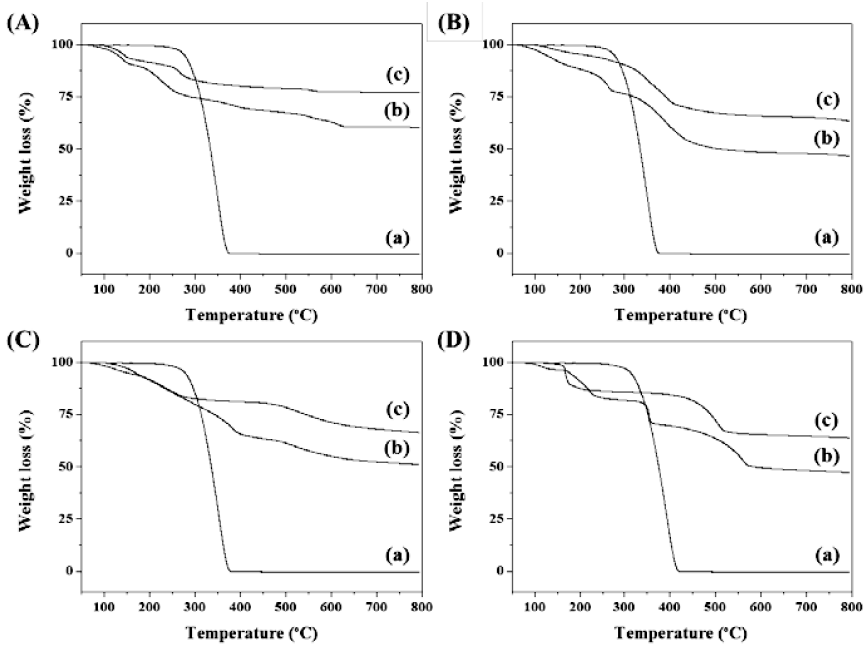


Figure 4.2. TGA curves of (a) PLGA, (b) LMH sheet, and (c) LMH of (A) CaFe-HC, (B) MgAl-LDH, (C) ZnAl-LDH, and (D) Zn-HDS.

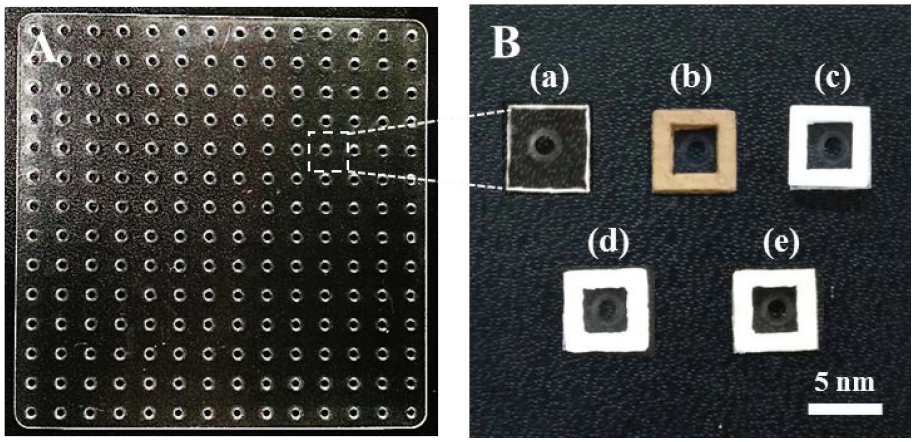


Figure 4.3. (A) Optical image of a whole Inion bone plate (PLT-1031). (B) Optical images of the 6.5 mm × 6.5 mm square-shaped piece of the plate (a) without and with a radiopaque (b) CaFe-HC, (c) MgAl-LDH, (d) ZnAl-LDH, and (e) Zn-HDS sheet. Scale bar represents 5.0 mm.

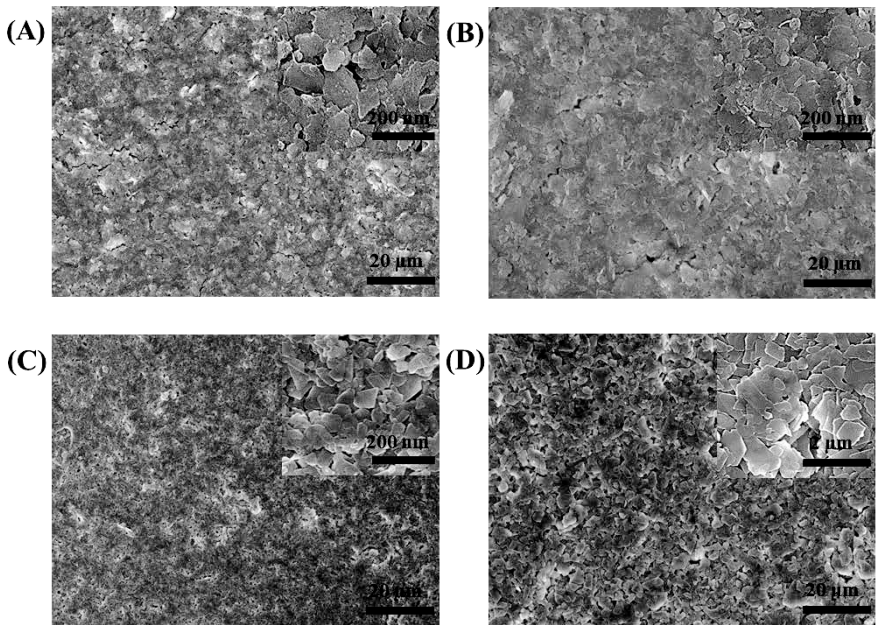


Figure 4.4. FE-SEM images of (A) CaFe-HC, (B) MgAl-LDH, (C) ZnAl-LDH, and (D) Zn-HDS sheet with inset of higher magnification.

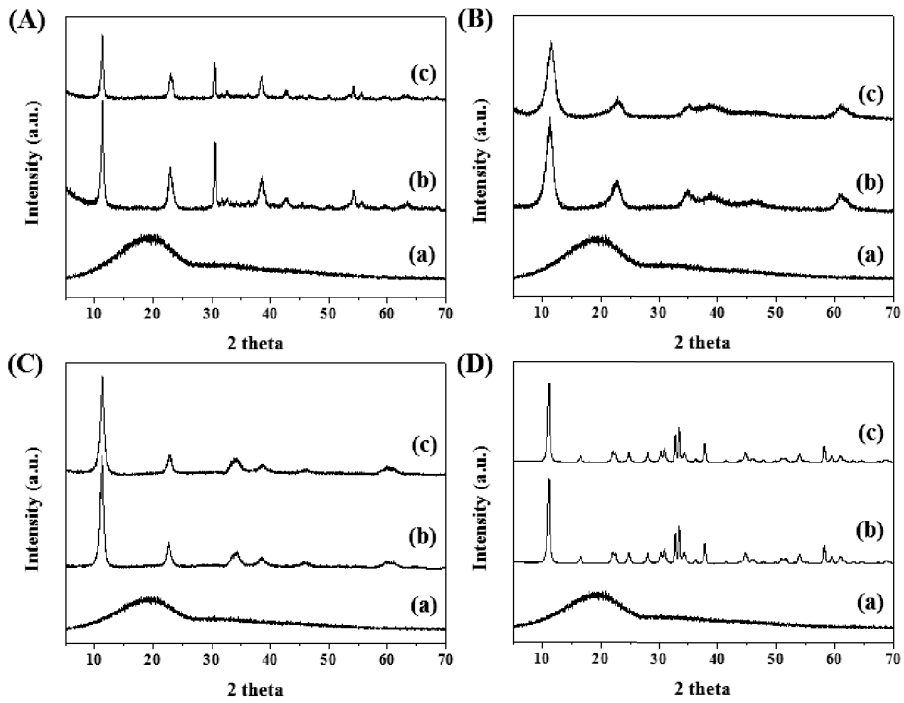


Figure 4.5. PXRD patterns of (a) PLGA, (b) LMH sheet, and (c) LMH of (A) CaFe−HC, (B) MgAl−LDH, (C) ZnAl−LDH, and (D) Zn−HDS.

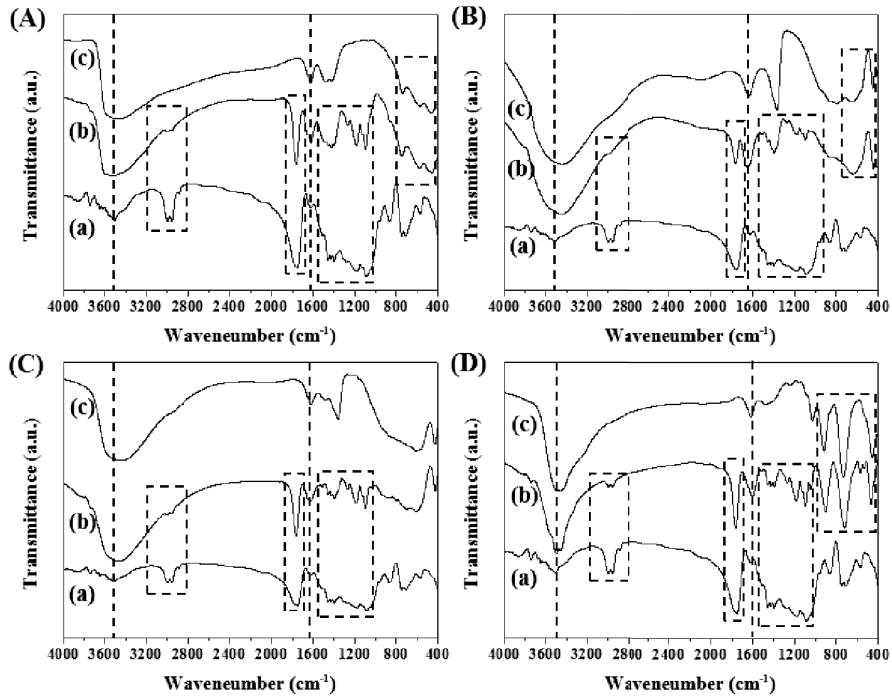


Figure 4.6. FT-IR spectra of (a) PLGA, (b) LMH sheet, and (c) LMH of (A) CaFe-HC, (B) MgAl-LDH, (C) ZnAl-LDH, and (D) Zn-HDS.

### 4.4.3 *In vitro* X-ray Visibility

To examine the longevity of radiopaque property (i.e., *in vitro* X-ray visibility), the 2.0-mm thick CaFe-HC sheet, MgAl-LDH sheet, ZnAl-LDH sheet, and Zn-HDS sheet attached plates were each immersed in PBS at pH 7.4 at 37℃, and their X-ray images were obtained using a mobile C-arm at predetermined schedules for 28 days. Figure 4.7 shows the representative *in vitro* X-ray images of the LMH plates, where a distinctive square frame shape was observed with all plates herein during the whole tested period. On the basis of X-ray attenuation coefficients and contents of metals in LMHs, I could modulate X-ray visibility of LMH plates by controlling metal compositions of LMH. The degrees of X-ray visibility for each LMH plate was in the order of Zn-HDS_P, ZnAl-LDH_P, CaFe-HC_P, and MgAl-LDH_P, as expected. For all plates, as the time elapsed, the visibility became lower and the edge of the layer became less distinctive, which could be ascribed to the swelling of the binder material, PLGA, and its degradation to free the LMH particles from the radiopaque sheets. Moreover, according to the theoretically calculated solubility diagrams of metal hydroxides depending on pH values (Figure 4.8),[127, 128] metal hydroxide layers of LMHs could be dissolved in the simulated physiological condition.

To further confirm this, I quantitatively analyzed the images using densitometry measurements and plotted versus time as shown in Figure 4.7(B). CaFe-HC_P exhibited a statistically significantly

higher densitometry values than the MgAl-LDH_P until 14 days (*$p$ < 0.05) and ZnAl-LDH_P showed statistically significantly higher densitometry values than CaFe-HC_P and MgAl-LDH_P during the whole tested period (**$p$ < 0.05). Moreover, Zn-HDS_P presented statistically significantly higher densitometry values than the other plates during the whole tested period (***$p$ < 0.05). For all plates, the densitometry values decreased with time, which was in good agreement with the X-ray images shown in Figure 4.7(A).

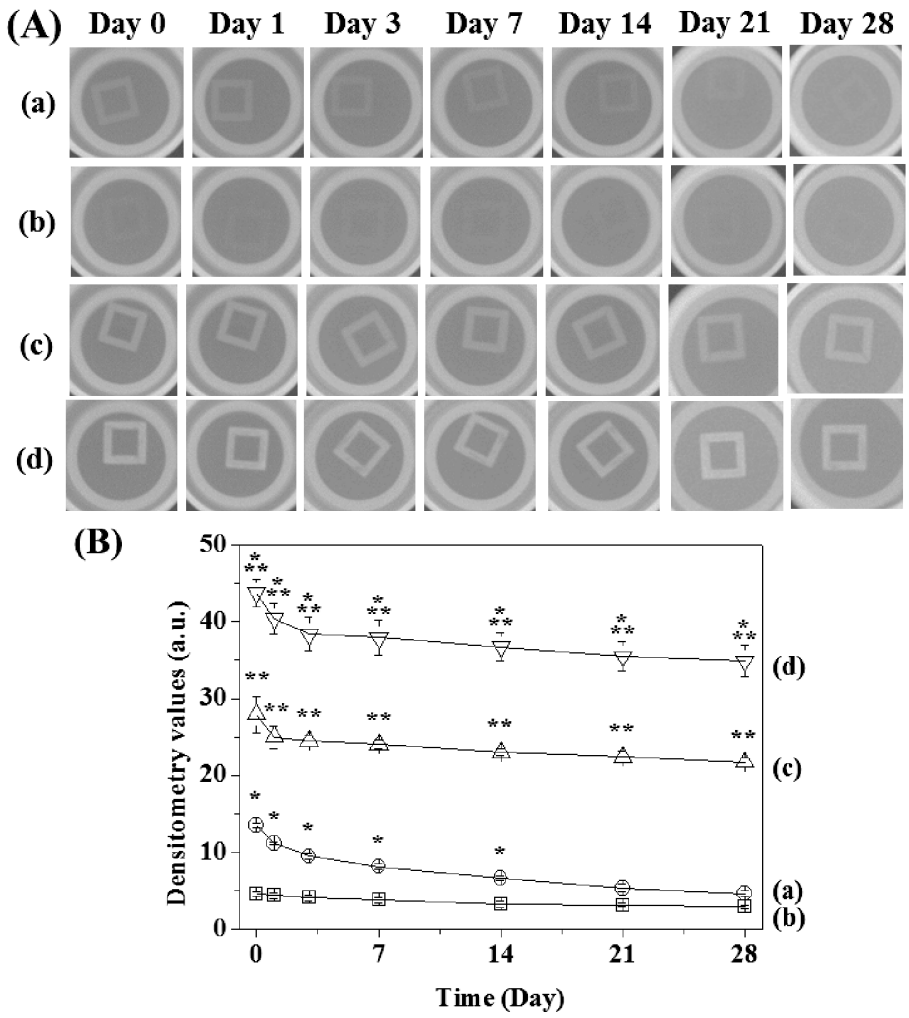


Figure 4.7. (A) Representative *in vitro* X-ray images and (B) densitometry measurements of the CaFe-HC_P, (b) MgAl-LDH_P, (c) ZnAl-LDH_P, and (d) Zn-HDS_P for a period of 28 days. *The CaFe-HC_P was statistically significantly different from MgAl-LDH_P ($p < 0.05$). **The ZnAl-LDH_P was statistically significantly different from both CaFe-HC_P and MgAl-LDH_P ($p < 0.05$). ***The Zn-HDS_P was statistically significantly different from all other radiopaque plates ($p < 0.05$).

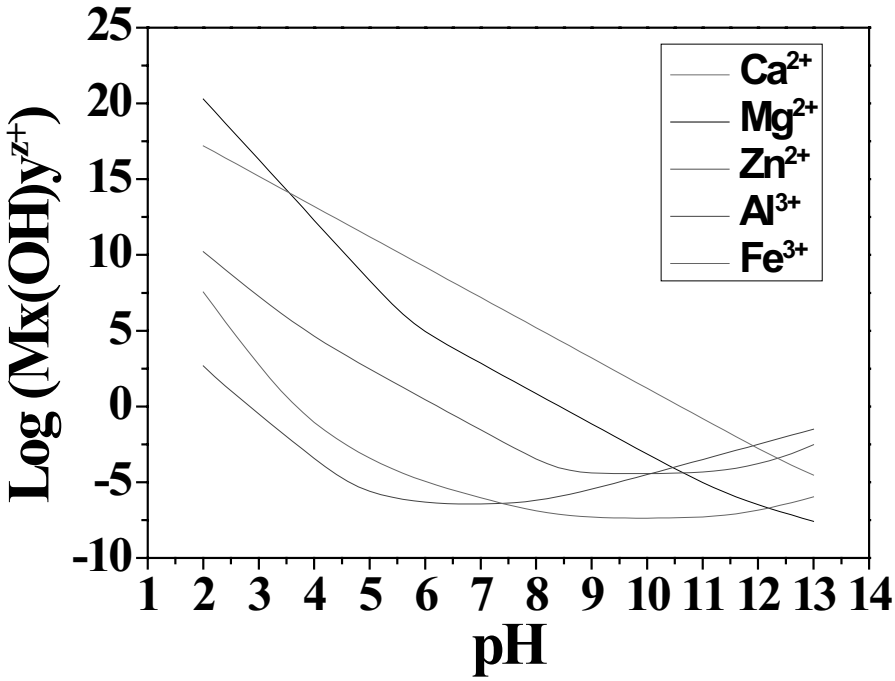


Figure 4.8. The theoretically calculated solubility diagrams of metal hydroxides depending on pH values.

### 4.4.4 *In vitro* Cell Viability

In order to ultimately apply LMHs as radiopaque materials to practical X-ray diagnosis, the LMHs should be confirmed whether they are biocompatible or not. Thus, I simply carried out *in vitro* cytotoxicity test of pristine LMHs on L929 murine fibroblasts. As shown in Figure 4.9(A), CaFe-HC and MgAl-LDH did not influence the cell viability, demonstrating that both exhibited good cytocompatibility, but Zn containing LMHs (i.e., ZnAl-LDH and Zn-HDS) exhibited apparent cytotoxicity under the concentrations tested in this work. The cell viability treated with ZnAl-LDH and Zn-HDS was statistically significantly lower ($p < 0.05$) than those treated with the CaFe-HC and MgAl-LDH at the concentration above 31.25 and 15.62 μg/ml, respectively. Cell viability continuously decreased as concentration of ZnAl-LDH and Zn-HDS increased up to 500 μg/ml. A large amounts of ZnAl-LDH and Zn-HDS treated into L929 cells at once led to cell death initially, followed by lower proliferation of the remaining viable cells than that of negative control. As reported in previous studies, Zn-containing LMHs have been reported to be cytotoxic above a certain threshold.[35, 129, 130] Since, however, the radiopaque LMH sheets bound with PLGA were designed to slowly release LMH particles and to be decomposed, concurrently with the intact Inion bone plate, *in vitro* cytotoxicity of LMHs could be reduced and minimized. With this aim, I prepared a controlled *in vitro* environment in which 2 mL of immersion medium

containing the plate was fully replaced with fresh medium, and the collected media were used to evaluate cell viability, where *in vivo* clearance of the LMH particles was assumed. As shown in Figure 4.9(B), neither the CaFe-HC_P nor MgAl-LDH_P exhibited any statistically significant difference in cytotoxicity at the sampled times over 42 days when compared with the non-treated cell groups. Although dissolved $Zn^{2+}$ and released Zn-containing particles from the ZnAl-LDH sheet and Zn-HDS sheet had an effect on the cell viability until 21 and 28 days, respectively, after those days, those plates exhibited good cytocompatibility.

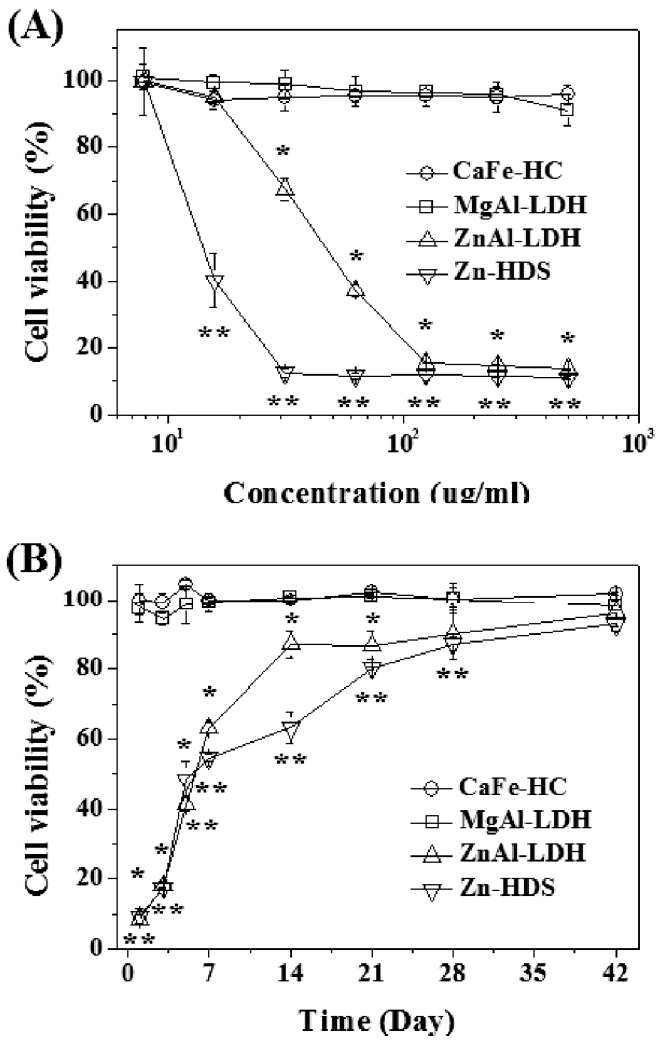


Figure 4.9. *In vitro* cell viability of of L929 cells treated with (A) the powder of LMH and (B) the collected extract medium from the immersion medium where the radiopaque plates were each immersed in the cell culture medium at 37℃ for 42 days. The immersion medium was withdrawn to give the extract medium and an equal volume of the fresh medium was added back every 2 days. *The ZnAl-LDH was significantly different from both CaFe-HC and MgAl-LDH ($p < 0.05$). **The Zn-HDS_P was significantly different from all other LMHs ($p < 0.05$).

### 4.4.5 *In vivo* X-ray Visibility

I examined *in vivo* X-ray visibility of the radiopaque plates for 42 days following their insertion into the subpanniculus pocket of the SD rat. As depicted in Figure 4.9(A), radiopaque MgAl-LDH_P, ZnAl-LDH_P, and Zn-HDS_P were discernible *via* X-ray for the entire period of the *in vivo* experiment and showed the decreases in visibility with time, which was consistent with the results from the *in vitro* immersion test (Figure 4.7). That was because LMHs were decomposed and PLGA incorporated into the sheet caused swelling and degradation in physiological condition, leading to the release of LMH particles. However, CaFe-HC_P could show discernible image *via* X-ray up to 1 day after implantation (Figure 4.10). According to the theoretically calculated solubility diagram of metal hydroxide depending on various pH values (Figure 4.8),[127, 128] the solubility of calcium hydroxide is relatively higher than other metal hydroxides, such as magnesium hydroxide, zinc hydroxide, aluminum hydroxide, and iron hydroxide under physiological condition of subcutaneous tissue ranging from pH 7.3 to 7.6,[131] in which the layer structure of CaFe-HC could not be maintained.

As shown in Figure 4.9(B), Zn-HDS_P exhibited better defined images than the ZnAl-LDH_P and MgAl-LDH_P throughout the testing period of 42 days ($p < 0.05$), which could be ascribed to the higher X-ray attenuation coefficients and contents of metals in Zn-HDS than those of ZnAl-LDH and MgAl-LDH. The densitometry

values of radiopaque LMH plates continuously decreased as the time elapsed. In the case of MgAl-LDH_P, its densitometry value became undetectably low from 42 days. However, the radiopaque LMH plates herein were X-ray visible in an acceptable level for up to 4 weeks, which could be considered sufficiently long to diagnose the possible loosening of a bone plate in clinical conditions.[108, 132, 133]

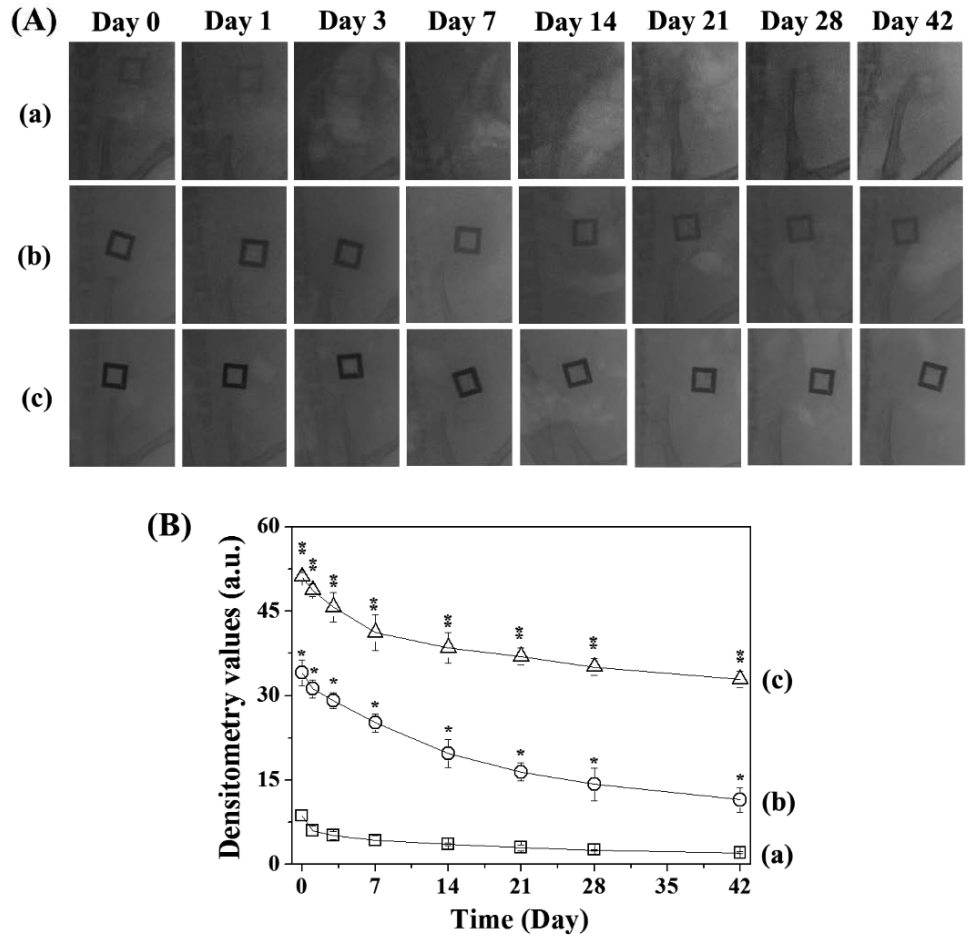


Figure 4.10. (A) Representative *in vivo* X-ray images and (B) densitometry measurements of the (a) MgAl-LDH_P, (b) ZnAl-LDH_P, and (c) Zn-HDS_P inserted on subcutaneous tissue in rats for a period of 42 days. *The ZnAl-LDH_P was significantly different from MgAl-LDH_P ($p < 0.05$). **The Zn-HDS_P was significantly different from both MgAl-LDH_P and ZnAl-LDH_P ($p < 0.05$).

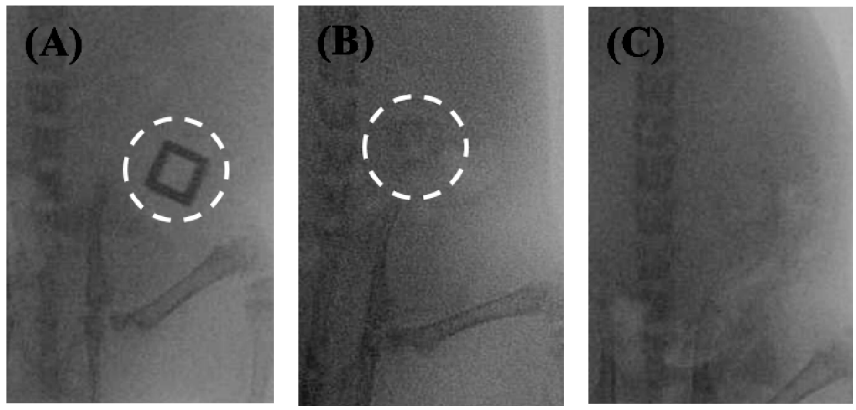


Figure 4.11. Representative *in vivo* X-ray images of the CaFe-HC_P inserted on subcutaneous tissue in rats at (A) day 0, (B) day 1, and (C) day 3.

### 4.4.6 *In vivo* Histological Analysis

To assess the *in vivo* biocompatibility, I performed a histological analysis of the tissues around the radiopaque LMH plates and compared them with the original plate in clinical use. As shown the images of biopsied tissues on H&E staining in Figure 4.11, for all groups, lymphocytes, neutrophils, and other active inflammatory components were barely observed and no sign of necrosis and abscess was seen within the surgical site for implantation of LMH plates. A few pigment laden macrophages were observed along the surface of the LMH plates. Overall, upon microscopic evaluation, there appeared to be no significant difference in inflammation degree between the plate already approved in clinical use and the other radiopaque LMH layer loaded plates. This result implied good *in vivo* biocompatibility of the radiopaque LMH plates prepared in this work.

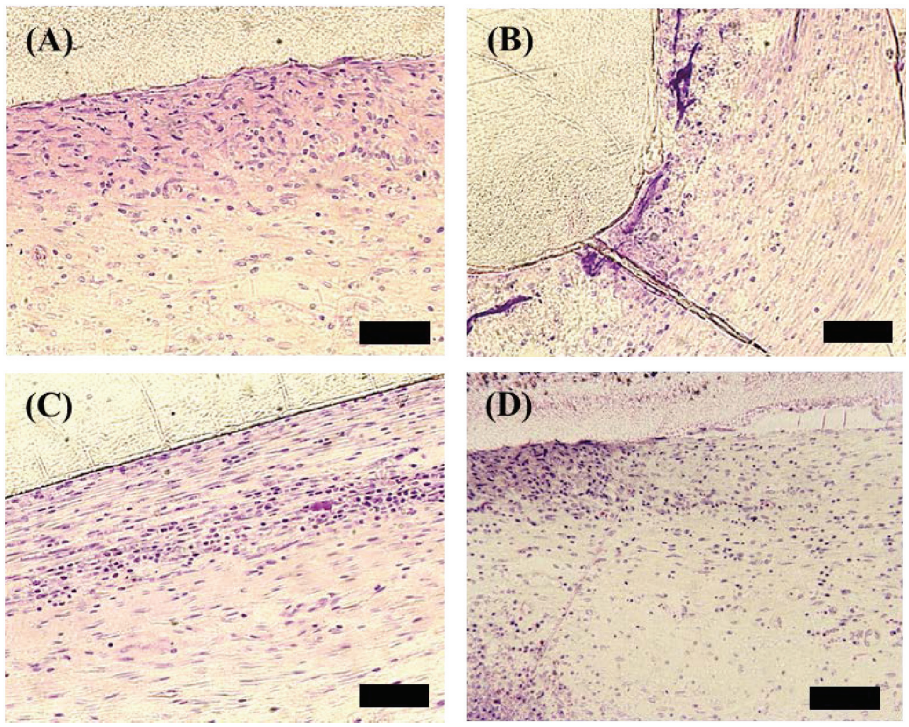


Figure 4.12. Histological images from the tissues around surgical area obtained at 42 days after plate implantation of (A) UP, (B) MgAl-LDH_P, (C) ZnAl-LDH_P, and (D) Zn-HDS_P.

## 4.5 Conclusion

Biodegradable bone fixation devices present challenges in X-ray imaging, which is often needed to monitor their proper positioning after fixation, due to their radiolucent properties. Thus, in order to endow X-ray visibility, I developed a bioabsorbable bone plate in combined with a radiopaque sheet, which was composed of LMH and PLGA as radiopaque and binder materials, respectively. The degree of X-ray visibility could be varied depending on the metal compositions of LMHs in the radiopaque sheets, and the sheet could be degraded and disappeared gradually along with the original Inion plate. The release of LMH particles during degradation of radiopaque sheet could be modulated to avoid or minimize possible toxicity. In this work, the *in vivo* X-ray images from the Zn-HDS_P was more discernible than those from the MgAl-LDH_P and ZnAl-LDH_P during the whole tested period since the higher X-ray attenuation coefficients and contents of metals in Zn-HDS than those of ZnAl-LDH and MgAl-LDH. According to the *in vivo* experiments with rats, the radiopaque LMH plates exhibited good biocompatibility, similar to that of the Inion plate already in clinical use. Therefore, I concluded that a biodegradable bone plate assembled with a LMH-based, radiopaque sheet has a great potential to be used as an orthopaedic fixation system to enable X-ray imaging diagnosis.

# Part IV.

# Layered Double Hydroxide Based Nanohybrid as Theranostic Agent

# Chapter 5

## Theranostic Bioabsorbable Bone Fixation Plate with Drug–Layered Double Hydroxide Nanohybrids

### 5.1 Abstract

I propose a bioabsorbable polymeric bone plate enabled with both diagnostic and therapeutic functionalities (radiopacity and sustained drug release, respectively). To this end, I examine a drug–inorganic nanohybrid (RS–LDH) as a theranostic agent by intercalating an anti–resorptive bone remodeling drug, risedronate (RS) into a layered double hydroxide (LDH) *via* an ion–exchange

reaction. The RS-LDH is prepared as a sheet with a biodegradable polymer, poly(lactic-co-glycolic acid) (PLGA), and is then attached onto the clinically approved bioabsorbable bone plate to produce the theranostic plate. Because of the presence of the metals in the LDH, the theranostic plate resulted in discernible *in vivo* X-ray images for up to 4 weeks after implantation. Concurrently, bone regeneration is also significantly improved compared with the other control groups, likely because of this material's sustained drug-release property. The theranostic plate is also largely biocompatible, similar to the plate already approved for clinical use. I conclude that the combination of a biodegradable bone plate with RS-LDH nanohybrids can constitute a promising system with theranostic ability in both X-ray diagnosis and expedited bone repair.

## 5.2 Introduction

Internal bone fixation devices are used in orthopedic clinical practices to prevent undesired motions of fractured bones until healing is complete.[99, 134] Therefore, many fixation devices are made of metals to provide enough mechanical strength to hold the fractured bone in place. However, the metallic fixation devices often need a secondary removal surgery, thereby causing low compliance to patients.[135] In this respect, the fixation devices made of bioabsorbable polymers, such as poly(lactic-co-glycolic acid) (PLGA), poly(lactic acid), poly(glycolic acid), or poly(trimethylene carbonate),[102, 103, 136, 137] can replace the metallic ones to treat the injured bones where a high mechanical load is not required.[106, 107] Moreover, the gradually lessened strength by biodegradation can minimize stress shielding, resulting in a formation of dense bone.

For successful treatment of fractured bone, adequate positioning of the fixation devices is important to minimize gap formation within the bone fracture, which needs to be monitored after implantation to avoid retarded healing and infection. This can be performed noninvasively by conventional X-ray imaging for the metallic devices, which, however, is not possible with the bioabsorbable polymer device due to its inherent radiolucent property.[111, 117, 118] Another consideration is proper bone regeneration in gaps and voids at the injured sites. In case of

osteoporosis-related bone fractures, bone formation is often delayed. Moreover, there is a high chance of loosening of fixation devices due to pathologically low bone density.[138, 139]

For those reasons, a bioabsorbable fixation device can be more advantageous when enabled with both diagnostic and therapeutic functionalities, i.e., X-ray visibility and delivery of a bone-forming agent, respectively. Previously, polymeric bone cements, plates or dental resins were combined with radiopaque materials, such as iodine, bismuth and biocompatible ceramics.[109, 111, 117, 118] To aid bone healing, the therapeutic agents, such as bisphosphonate drugs and bone morphogenetic proteins, were also incorporated with implantable polymer devices.[139-149] However, those studies addressed only a single aspect of unmet clinical needs, i.e., either diagnostic or therapeutic inability.

In this present work, therefore, I propose a bioabsorbable bone plate enabled with dual functionalities of both diagnostic and therapeutic abilities. For this purpose, I employ a drug intercalated layered double hydroxide (LDH) nanohybrid as a theranostic agent to be integrated with a bioabsorbable bone fixation device in clinical use. LDH-based nanohybrids have been receiving many attentions due to their extraordinarily high synergetic effects and complementary behaviors by nanohydridization.[6, 8, 18] In particular, LDH, a synthetic anionic clay, has been known as a promising drug delivery carrier.[11, 15, 19, 26, 29, 38] Isomorphous substitutions of the divalent $M^{2+}$ in layers by trivalent $M^{3+}$ give

positively-charged layers, which can be balanced with charge compensating drug molecules in the interlayer region of LDH. At the same time, LDH can work as a radiopaque material due to higher X-ray attenuation coefficients of di- and trivalent metals, such as Zn and Al, respectively, in LDH lattice.[23-25] In addition, the LDH has been proven biocompatible to a large extent according to many previous studies.[33, 54, 55]

In this work, I prepared a theranostic nanohybrid (i.e., RS-LDH) by intercalating risedronate (RS), an anti-resorptive and bone-remodeling drug already approved in clinical use for treatment of osteoporosis,[150, 151] into LDH by ion-exchange reaction and for the first time to our knowledge, I proposed a combined entity of a bioabsorbable bone plate and the RS-LDH to be enabled with both X-ray imaging and sustained, local drug release for expedited bone repair. To prepare a proof-of-principle prototype, I separately prepared a theranostic sheet, where the RS-LDH particles were bound with a biodegradable polymer, PLGA and attached it to the Inion bone fixation plate approved in clinical use (PLT-1031, Inion, Finland). In such a way, the sheet could be X-ray visible due to the presence of metals in RS-LDH and at the same time, RS could be released in a sustained manner *via* deintercalation from the lattices of LDH. PLGA in the sheet would be degraded to free RS-LDH, which would also allow gradual disappearance of the sheet like the bioabsorbable plate used herein.

## 5.3 Experimental Section

### 5.3.1 Materials

Zinc nitrate hexahydrate ($Zn(NO_3)_2 \cdot 6H_2O$), aluminum nitrate nonahydrate ($Al(NO_3)_3 \cdot 9H_2O$), risedronate sodium hemi-pentahydrate (RS, $C_7H_{10}NO_7P_2Na \cdot 2.5H_2O$), sodium hydroxide (NaOH), and hydrogen chloride (HCl) were obtained from Sigma (MO, USA). PLGA (lactic acid:glycolic acid (50:50); average molecular weight 4.1 kDa; intrinsic viscosity = 0.08 dL/g) and dimethylformamide (DMF) were purchased from Lakeshore Biomaterials (AL, USA) and J.T. Baker (PA, USA), respectively. Bioabsorbable bone fixation plate (PLT-1031), composed of poly(trimethylene carbonate), polylactide, and polyglycolide, was obtained from Inion (Finland). PBS (pH 7.4) was supplied from Seoul National University Hospital Biomedical Research Institute (Korea). Dulbecco's modified Eagle's essential medium (DMEM), penicillin streptomycin, fetal bovine serum (FBS), 0.25% Trypsin-EDTA (1X), and Dulbeccos Phosphate-buffered saline (DPBS) were purchased from Gibco (Life Technologies, UK). β-Glycerophosphate, dexamethasone, L-ascorbic acid, and dimethyl sulfoxide (DMSO) were purchased from Sigma (MO, USA). A cell counting Kit-8[89] (CCK-8, DOJINDO, Japan) and p-nitrophenyl phosphate (pNPP) ALP assay kit[82] (AnaSpec, CA, USA) were used following the manufactures' instruction. Zolazepam and tiletamine (Zoletil®) were supplied from Virbac (France) and xylazine (Rompun®) was from

Bayer (Germany). The bioabsorbable sutures (Vicryl 3-0 and 5-0) were supplied from Ethicon (NJ, USA). Trephine burr and Betadine® were obtained from OSUNG (TPHB-B8, Korea) and Hyundai Pharmacy (Korea), respectively.

### 5.3.2 Preparation of Pristine LDH and RS-LDH

To prepare pristine LDH, a solution of 10 mM $Zn(NO_3)_2 \cdot 6H_2O$ and 5 mM $Al(NO_3)_3 \cdot 9H_2O$ in 250 ml decarbonated water was stirred for 0.5 h until it became transparent. Then, it was precipitated by adjusting pH to 8.0 with a 0.5 M NaOH solution and aged for 24 h at room temperature. The resulting precipitates were centrifuged, washed three times with decarbonated water to eliminate unreacted ions, and freeze-dried. Then, I prepared RS-LDH by ion-exchange reaction. Briefly, a 0.05 M solution of RS in 100 ml of decarbonated water was titrated to pH 8.0 with a 0.5 M NaOH solution. The pristine LDH (1.5 g) was then dispersed in 100 ml decarbonated water, which was then added into the 100 ml RS solution. After the mixture was stirred at room temperature for 24 h, the RS-LDH was centrifuged, thoroughly washed with decarbonated water, and freeze-dried. All the reactions were performed under nitrogen atmosphere to avoid carbonate contamination.

### 5.3.3 Preparation of Functional Bone Plates

I first fabricated a bioabsorbable sheet containing LDH or

RS-LDH, as depicted in Scheme 1. For this, a sheet of poly(methyl methacrylate) (PMMA; EunSung Polytechnology, Korea) with 1.0 mm or 2.0 mm in thickness was cut into pieces to form a square-shaped frame (outer edge: 6.5 mm; side of a square hole: 2.5 mm), using a $CO_2$ laser (FC-200RA LASER Machinery, South Korea). The resulting piece was used to make a substrate of polydimethylsiloxane (PDMS) (Sylgard®184, Dow Corning, MI). To prepare a LDH or RS-LDH sheet, a fine powder of 150 mg pristine LDH or RS-LDH, respectively, was homogeneously mixed with 100 $\mu$l of a PLGA solution in DMF (30% w/v). The wells in the PDMS substrate were then densely packed with the resulting paste and lyophilized for 1 day to obtain the sheets. In this work, I prepared three distinct sheets: a 2.0-mm thick LDH sheet, 1.0-mm thick RS-LDH sheet and 2.0-mm thick RS-LDH sheet. For all sheets prepared in this work, the mass ratio of PLGA and LDH or RS-LDH was 1:5. To prepare a functional bone plate, I attached the resulting sheet on the surface of a bioabsorbable Inion bone plate. In this work, a whole piece of an Inion bone plate was cut into 6.5 mm × 6.5 mm square-shaped pieces, each with a screw hole at the center (Figure 5.1). Then, a PLGA solution in DMF (30% w/v) was sprayed on the top of the plate under the following condition: diameter of nozzle orifice: 0.5 mm, spraying pressure: 15 psi, spraying time: 2 s, spraying distance: 15 cm. Right after that, the LDH or RS-LDH sheet was placed and bonded with the plate, as shown in Scheme 1(D). The resulting functional plate was then lyophilized for 1 day to eliminate residual solvent. In this

present work, I prepared four different types of the plates, as listed below:

(1) UP: unmodified bioabsorbable bone plate

(2) LDH_P2: bioabsorbable bone plate attached with a 2.0-mm thick LDH sheet

(3) RS-LDH_P1: bioabsorbable bone plate attached with a 1.0-mm thick RS-LDH sheet

(4) RS-LDH_P2: bioabsorbable bone plate attached with a 2.0-mm thick RS-LDH sheet

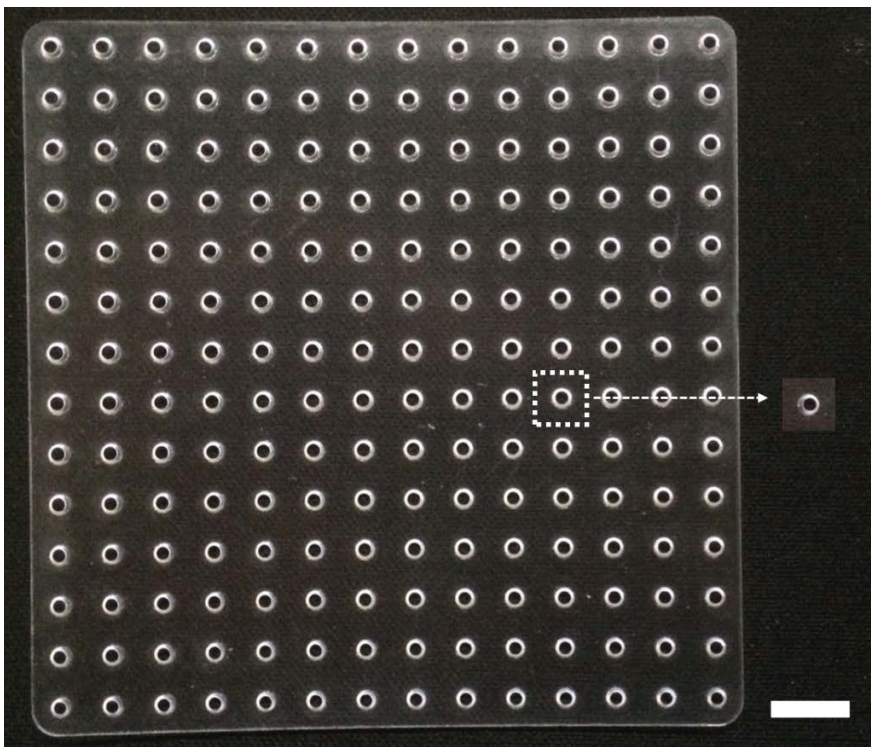

Figure 5.1. Optical image of a whole Inion bone plate (PLT-1031). To prepare the experimental samples, I cut a whole plate into pieces, each of 6.5 mm x 6.5 mm square shape with a screw hole at the center. The scale bar represents 1 cm.

### 5.3.4 Characterizations

The structural analysis was carried out using powder X-ray Diffraction (PXRD) (D/MAXRINT 2200-Ultima, Rigaku, Japan) equipped with Ni-filtered Cu-K$\alpha$ radiation ($\lambda$ = 1.5418 Å). Fourier transform infrared spectroscopy (FT-IR) spectra were obtained by the potassium bromide pellet method using a spectrophotometer (JASCO FT-IR 6100, Japan). The images of the pristine LDH, RS-LDH, and plates were obtained *via* field emission scanning electron microscopy (FE-SEM, JSM-6700F, JEOL, Japan). Before imaging, the sample was sputter-coated with platinum (208HR, Cressington Scientific, UK). The particle size distribution and surface charge were measured with a zetasizer (Nano ZS, Malvern, UK), where the samples were suspended in deionized (DI) water. The elemental analysis (EA1110, CE instrument, Italy) and inductively coupled plasma atomic emission spectroscopy (ICP-AES, Optima-4300 DV, PerkinElmer, USA) were also carried out to assess the chemical compositions of pristine LDH and RS-LDH.

### 5.3.5 Measurement of Drug-Loading Amount

In order to determine the amount of intercalated RS, 25 mg RS-LDH was dispersed in 100 ml of a 2 M HCl solution, which was sonicated for 10 min to completely dissolve both RS and LDH. The resulting solution was filtered with a Nylon syringe filter (pore size: 0.45 $\mu$m; Millipore, USA), where the aliquot was measured using a

UV-Vis spectrophotometer (Perkin-Elmer Lambda 35). To determine the RS amount in the sheet, the RS-LDH_P1 and RS-LDH_P2 were each added into a 50 ml DMF solution, which was vigorously stirred to completely dissolve PLGA in the sheet. The resulting suspension was then centrifuged at 14,000 rpm and the aliquot of DMF was obtained. The remaining DMF solution was then completely removed to collect the RS-LDH, which was dissolved in a 2 M HCl solution and treated as described above to obtain the aliquot of HCl. Both aliquots of DMF and HCl were measured with a UV-Vis spectrophotometer to obtain the loading amount of RS in the sheet.

### 5.3.6 *In vitro* Cell Study

#### 5.3.6.1 Cell Culture

The human osteoblast-like cell line (MG63) was obtained from Korean Cell Line Bank. The cells were grown in the culture medium, i.e., the DMEM medium supplemented with 10% FBS, 100 units/ml penicillin, and 100 μg/ml streptomycin, under a humidified atmosphere (5% $CO_2$ and 95% air) at 37° C. At 80 ~ 90% confluence, the cells were isolated from the culture dishes by trypsinization with Trypsin-EDTA and washed with DPBS. In this work, all tested samples were sterilized using ethylene oxide (EO) gas prior to *in vitro* cell study.

### 5.3.6.2 Cell Proliferation Study

MG63 cells were placed on 96-well microplates at a density of $2.0 \times 10^4$ cells/well and incubated overnight at 37° C under a 5% $CO_2$ atmosphere for 24 h. The cell medium in each well of the plate was completely substituted with osteogenic medium containing intact RS, pristine LDH, and RS-LDH and the cells were cultured for 3 days to examine their proliferation. I prepared the osteogenic medium by adding L-glutamine (2 mM), $\beta$-glycerophosphate (10 mM), and L-ascorbic acid (50 ng/ml) into the culture medium. The cells were incubated with intact RS or RS-LDH at the equivalent RS concentrations of $1.0 \times 10^{-10}$ M, $1.0 \times 10^{-8}$ M, and $1.0 \times 10^{-6}$ M. The cells were also incubated with the pristine LDH at the equivalent LDH concentrations used with the RS-LDH above. After incubation for 3 days, the wells were washed with DPBS and then, a 100 $\mu$l of CCK-8 solution was added into each well, which was incubated for additional 3 h. CCK-8 allows sensitive colorimetric assays for the determination of cell viability in cell proliferation assay.[89] Optical density (OD) of each well was recorded at 450 nm on a microplate reader (Multiskan FC, Thermo Scientific, USA). Cell proliferation was expressed as the percentage of $(OD_{test} - OD_{blank})/(OD_{control} - OD_{blank})$, where $OD_{test}$ is from the wells containing the cells treated with the sample, $OD_{control}$ is from the wells containing the cells treated with the osteogenic medium only, and $OD_{blank}$ is from the blank wells without cells and medium. At least three batches were tested for each sample type.

#### 5.3.6.3 Alkaline Phosphatase (ALP) Activity

MG63 cells were placed on 6-well microplates at a density of $1.5 \times 10^5$ cells/well and incubated overnight at 37° C under a 5% $CO_2$ atmosphere for 24 h in order to measure ALP activity, which is widely used as a marker for early differentiation of osteoblast-like cells.[82] The cell medium in each well of the plate was completely substituted with the osteogenic medium containing intact RS, pristine LDH, or RS-LDH and treated under the same conditions described above. After incubation for 3 days, the adherent cells in each well were scraped off and collected in a micro-centrifuge tube. The cell suspension was incubated at 4° C for 10 min with agitation and then centrifuged at 2500 rpm for 10 min. The supernatant (50 $\mu$l) was transferred to a well of a 96-well plate and a pNPP solution (50 $\mu$l) was added, where colorimetric changes were measured by a microplate reader (Multiskan FC, Thermo Scientific, USA) at 405 nm to quantitatively analyze the amount of enzyme released from the cells. At least three batches were tested for each sample type.

### 5.3.7 *In vitro* Drug Release Study

To examine *in vitro* drug release profiles, intact RS (6.75 mg), RS-LDH (30.0 mg), and the sheets of the RS-LDH_P1 and RS-LDH_P2 were each immersed in 10 ml of pH 7.4 PBS at 37° C, which was continuously agitated at 125 rpm in a shaking incubator (SI-300, JEIO TECH, Korea). At scheduled times for 42 days, the aliquot was

collected and the same amount of fresh PBS was added back. The sampled aliquot was filtered with a Nylon syringe filter (pore size: 0.45 $\mu$m; Millipore, USA) and then measured using a UV-Vis spectrophotometer (Perkin-Elmer Lambda 35, USA). For each sample type, at least three batches were tested for statistics.

### 5.3.8 *In vitro* X-ray Visibility Test

To evaluate X-ray visibility of functional plates herein, each of the LDH_P2, RS-LDH_P1, and RS-LDH_P2 was immersed in 10 ml PBS and then agitated at 125 rpm at 37° C in a shaking incubator. At scheduled times for 42 days, the sample was imaged, using a mobile C-arm (BV Pulsera, Philips, Netherlands) with a charging voltage of 55 kV. For each image, densitometry measurement was carried out using ImageJ software (National Institutes of Health, MD, USA), as previously reported.[124] At least three batches were assessed for each sample type.

### 5.3.9 *In vivo* Animal Study

For *in vivo* study, 9-week-old male Sprague-Dawley (SD) rats, weight: 260-330 g (Koatech, Korea) were individually housed and fed without any restriction. All experimental procedures were approved by the Institutional Animal Care and Use Committee (IACUC No. 13-0140) at Seoul National University Hospital. In this work, I prepared a critical size cranial defect model, following the

previously reported protocol.[139] Briefly, a cocktail of Rompun® (0.1 ml/kg) and Zoletil® (0.3 ml/kg) was intramuscularly injected. After that, the hair on the head was shaved and cleaned with betadine®. The cranial bone was exposed through a skin incision, 5.0 cm in length and the bone defect, 8.0 mm in diameter, was made with a trephine (TPHB-B8, Osung, Korea). I made two additional suture holes by drilling, which were 12 mm apart from each other and 2.0 mm apart from the edge of the defect. After sterilization with EO gas, the plate was placed on the area of cranial bone defect with the functional sheet facing toward the defect. The plate was then fixed by suturing through the two holes using a bioabsorbable suture. The incised skin was stitched up and treated with betadine®. In this work, I prepared five distinct animal groups.

(1) No treatment group: the animals without the plate
(2) UP group: the animals implanted with the UP
(3) LDH_P2 group: the animals implanted with the LDH_P2
(4) RS-LDH_P1 group: the animals implanted with the RS-LDH_P1
(5) RS-LDH_P2 group: the animals implanted with the RS-LDH_P2

For each of the animal groups, five animals were involved at first. Except for the no treatment group, one animal in each group died during the experiment from undeterminable causes and thus was excluded for data analysis. Therefore, at least four animals were assessed for each of the animal groups.

#### 5.3.9.1 *In vivo* X-ray visibility

To evaluate the longevity of *in vivo* X-ray visibility following the plate implantation, the heads of SD rats were imaged using a mobile C-arm (BV Pulsera, Philips, Netherlands) in manual mode with a charging voltage of 55 kV. For imaging, the rats were put under temporary anesthesia with intramuscular injection of a cocktail of Zoletil® and Rompun®. The images were obtained at scheduled times of 1, 2, 4, and 8 weeks after implantation. Each image was analyzed with densitometry measurements, using ImageJ software (National Institutes of Health, MD, USA), as previously reported.[124]

#### 5.3.9.2 *In vivo* Micro-Computed Tomography ($\mu$CT) Analysis

To examine new bone formation, the bone defect was imaged *via* $\mu$CT (NFR Ploaries-G90, NanoFocusRay, Korea) at 1, 2, 4, 8, and 12 weeks after plate implantation. At each time for imaging, the rats were scanned at an isotropic voxel size of 9 $\mu$m with a voltage of 55 kV and an X-ray tube current of 180 $\mu$A while being sedated with intramuscular injection of Zoletil® (0.3 ml/kg). From each $\mu$CT image, the regions of interest were defined on the basis of a cylindrical shape of cranial defect. The gray threshold level was set at 200 to determine new bone formation. I calculated the new bone volume percent by dividing the volume of newly formed bone by that of the initially created defect, using the AMIRA software (Version 5.4, ZIB & Visage Imaging, Germany).

#### 5.3.9.3 Histologic and Histomorphometric Evaluation

At 12 weeks after plate implantation, four rats per group were placed under deep anesthesia *via* intramuscular injection of Zoletil® (1 ml/kg) and sacrificed *via* intravenous injection of 10 ml of 15% (w/v) potassium chloride. Then, the tissues around the plates were biopsied to assess new bone formation and *in vivo* biocompatibility of plates. The obtained tissue samples were each fixed in fresh 10% (v/v) buffered neutral formalin for 3 days and embedded within resin, which were then sectioned into 30-40 $\mu$m thick slides (BS-3000N, EXAKT, Germany). The slides were then stained with hematoxylin-eosin (H&E) and examined using an optical microscope (BX53F, OLYMPUS, Japan) for histologic evaluation by a board certified professional pathologist. The histomorphometric analysis on each image were carried out by using the Image J software. The new bone area percent was calculated by dividing the area of newly formed bone by that of initially formed defect.

### 5.3.10 Statistical Analysis

*In vitro* cell proliferation, *in vitro* ALP activity, *in vivo* new bone volume percent, and *in vivo* normalized new bone area percent were each statistically analyzed with one-way analysis of variance (ANOVA) with $\alpha$ = 0.05 followed by pairwise comparisons using a Tukey's post hoc test (GraphPad Prism, version 5.01, USA). $p < 0.05$ was considered statistically significant.

## 5.4 Results and Discussion

### 5.4.1 Particle Analysis

The powder X-ray Diffraction (PXRD) patterns of intact RS, pristine LDH, and RS-LDH are shown in Figure 5.2(A). A nitrate form of pristine LDH exhibited two well-ordered (00*l*) reflections at the 2 theta angles of 10.2° and 20.4° to give basal spacing of 8.7 Å. However, after intercalative ion exchange reaction of RS molecules into pristine LDH, the basal spacing of RS-LDH was determined to be 11.2 Å, showing well-ordered (00*l*) reflections. Given the layer thickness of LDH (4.8 Å),[17] the gallery height of RS-LDH could be determined to be 6.4 Å, which was smaller than the molecular dimension of RS (Figure 5.3(A)). Therefore, it can be expected that the RS molecules were intercalated with a monolayer arrangement.

To confirm molecular arrangement of intercalated RS in RS-LDH, I investigated the steric limitation between the intercalated RS molecules and positively charged sites of LDH layer, which can be explained by the equivalent area ($A_e$, area per positive unit charge of LDH) and demanded area ($A_c$, area per negative unit charge for intercalated single molecule). $A_e$ of the layered host lattice can be calculated from the following equation, $A_e = a \cdot b \cdot \sin\gamma/\xi$, where $a$ and $b$ are lattice parameters and $\xi$ is the layer charge per formula unit. On the basis of the lattice parameters of the RS-LDH ($a = b = 3.07$ Å, $c = 33.54$ Å, $\gamma = 120°$ and $\xi = 1/3e^-$), $A_e$ of LDH was 24.5Å$^2$, which was larger than the demanded area ($A_c$) of RS (24.3 Å$^2$). In the case

of $A_e > A_c$, the guest molecules could be incorporated between the LDH layers with parallel monolayer orientation along with the ab plane of LDH.[17]

I compared relative intensity ($I_{rel}$) of the observed X-ray intensity ($I_{obs}$) to those of the calculated X-ray intensity ($I_{cal}$) from physicochemically possible structural models of RS-LDH as follows; two phosphate groups of RS were electrostatically interacted with each side of LDH layers (Figure 5.3(B)) and two phosphate groups of RS were electrostatically interacted with one side of LDH layer (Figure 5.3(C-D). The structure factor (F(00*l*)) of the each structural model was obtained from the atomic scattering factor for each atom in the unit cell ($f_i$) and the position of atoms ($z_i$) along c-axis consisting of the structure, by following the equation, $\boldsymbol{F(00l) = \sum_{i=0}^{N} f_i \cos(2\pi l z_i)}$. The integrated intensity of (00*l*) diffraction peak (I(00*l*)) was proportional to the square of structure factor (F(00*l*)) and to Lorentz-Polarization factor ($LP(\theta) = (1+\cos^2 2\theta)/(\cos\theta \cdot \sin^2\theta)$). Although it was not easy to refine the interlayer structure of the RS-LDH due to a limited number of (00*l*) diffractions, the interlayer structure in Figure 5.3(D) would be highly probable: the calculated X-ray intensity values from the structural model were close to the observed ones (Figure 5.3(E)).

Through cross-sectional high-resolution transmission electron microscopy (HR-TEM) images (Figure 5.2(B)), I clearly confirmed a well-ordered two dimensional layered structure of the RS-LDH along the crystallographic c-axis. The length between the

lattice fringes from the (00*l*) planes in the RS-LDH was observed to be 11.2 Å, which was in excellent agreement with the basal spacing obtained from the PXRD pattern of RS-LDH.

I also imaged the pristine LDH and RS-LDH *via* field emission scanning electron microscopy (FE-SEM) to assess their morphology. As shown in Figure 5.2(C-D), both pristine LDH and RS-LDH showed plate-like morphology. According to the dynamic light scattering (DLS) analysis (Figure 5.2(E)), the particle sizes were measured to be 120.2 ± 13 nm for pristine LDH and 153.3 ± 11 nm for RS-LDH, respectively. As shown in Figure 5.2(F), the pristine LDH exhibited a distinctive positive surface charge (35.1 ± 0.1 mV), as previously reported.[19] This was lowered to 6.4 ± 0.2 mV with the RS-LDH due to the charge compensation upon intercalation of negatively charged RS. According to the inductively coupled plasma atomic emission spectroscopy and elemental CHN analyses, the chemical compositions of pristine LDH and RS-LDH were $Zn_{0.67}Al_{0.33}(OH)_2(NO_3)_{0.33}\cdot 0.3H_2O$ and $Zn_{0.67}Al_{0.33}(OH)_2(RS)_{0.094}\cdot 0.25H_2O$, respectively. The content of intercalated RS in the RS-LDH was determined to be 22.5 ± 0.1 wt%, which was identical to the theoretically calculated value (Figure 5.4).

According to Fourier transform infrared spectroscopy (FT-IR) spectra (Figure 5.5), the characteristic infrared vibration bands of the intact RS, such as O-H (3567, 3396, and 3295 $cm^{-1}$) , P=O (1111 and 1051 $cm^{-1}$), P-O (981 $cm^{-1}$) were clearly observed, as previously reported.[152, 153] For the pristine LDH, the absorption

bands at 3451 and 1647 $cm^{-1}$ were assigned as O−H stretching of the hydroxide layer vibration and $H_2O$ bending, respectively. The absorption bands observed in the low frequency region below 800 $cm^{-1}$ were attributed to lattice vibration modes, such as M−O and M−O−M (M: metals, such as Zn and Al) vibrations. All characteristic bands from each of the constituent RS and pristine LDH were overlapped in the RS−LDH. Notably, the nitrate absorption peak at 1382 $cm^{-1}$ in the pristine LDH is absent in the RS−LDH, implying that the nitrate ions were completely replaced with negatively charged RS molecules after intercalative ion exchange reaction. The broad band corresponding to the OH stretching, associated with the O=P−OH group of RS observed between 1800 and 2700 $cm^{-1}$, disappeared in the RS−LDH due to the deprotonation of those OH groups and the binding with the layer of LDH.[94, 154] Furthermore, C−C (1562 and 1470 $cm^{-1}$) and C−N (1384 $cm^{-1}$) stretching bands of RS were red−shifted to 1487, 1432, and 1366 $cm^{-1}$, respectively, because of the hybridization of RS with LDH. Upon the comparison of FT−IR spectra among intact RS, pristine LDH, and RS−LDH, it is clear that RS molecules in form of deprotonated phosphonate would be bound to the positively charged surface of LDH by electrostatic interaction.

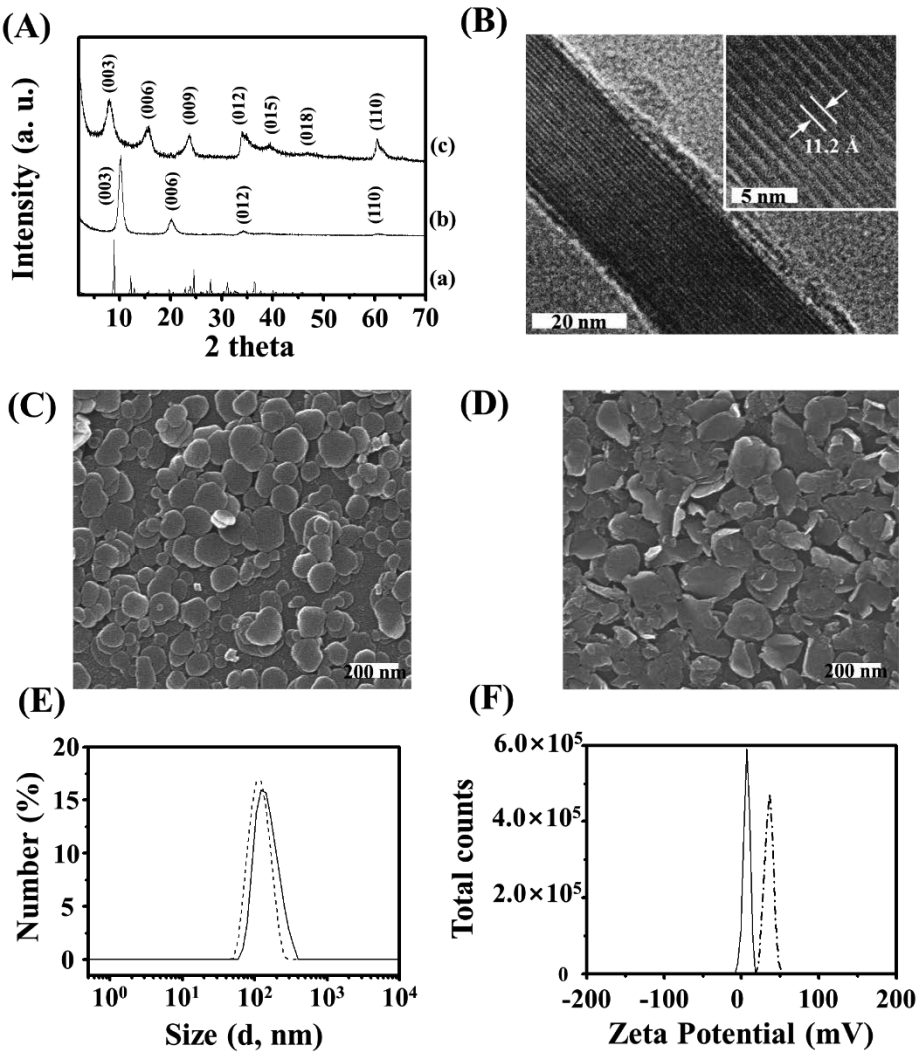


Figure 5.2. (A) PXRD patterns of (a) intact RS, (b) pristine LDH, and (c) RS-LDH. (B) HR-TEM image of RS-LDH with inset of higher magnification. FE-SEM images of (C) pristine LDH and (D) RS-LDH. (E) Particle size distributions and (F) zeta potentials of the pristine LDH (dashed line) and RS-LDH (solid line).

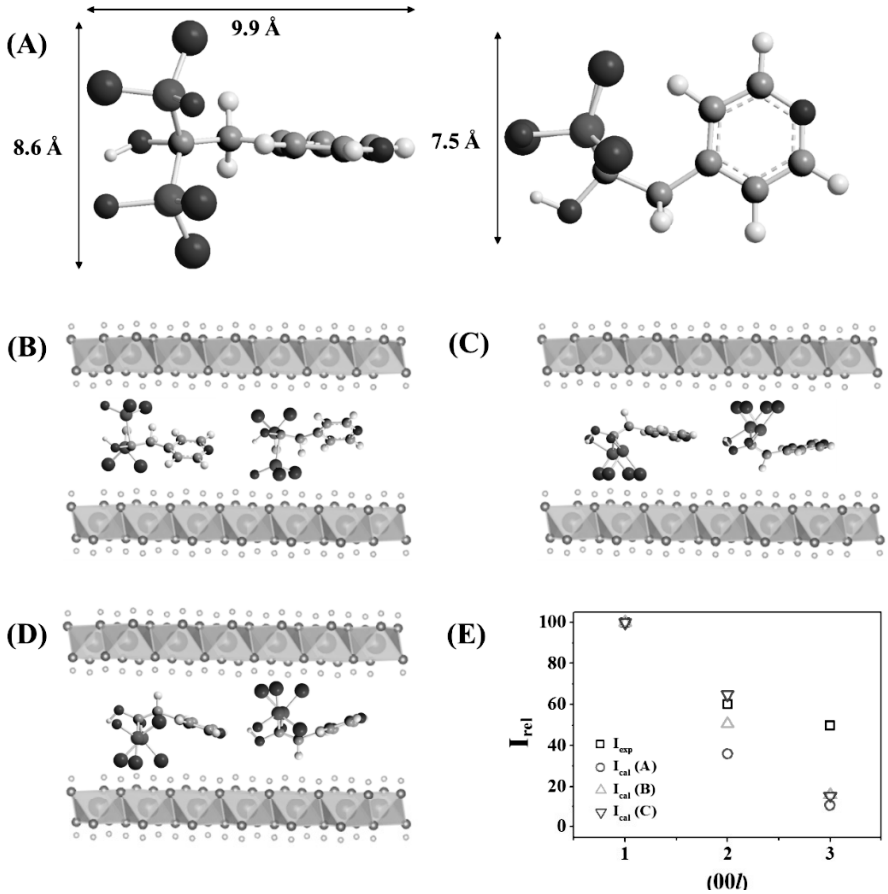


Figure 5.3. (A) Molcular dimension of RS and (B–D) structural models of the RS–LDH along the crystallographic c–axis. (E) The relative X–ray intensity ($I_{rel}$) of observed intensity ($I_{obs}$) obtained from PXRD of the RS–LDH and calculated intensity ($I_{cal}$) corresponding to three different structural models of RS–LDH.

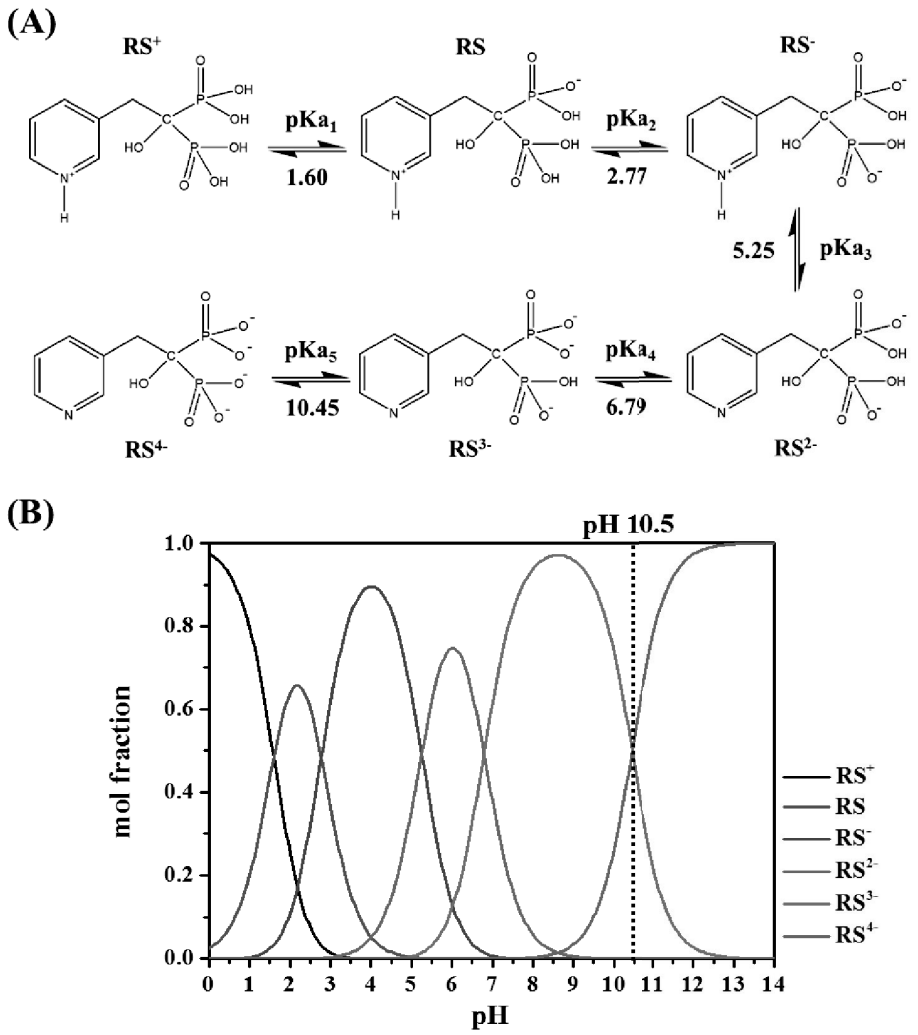


Figure 5.4. (A) Chemical structures and dissociations of RS depending on the values of equilibrium dissociation constant (pKa) of RS.[94] (B) Speciation curves calculated from the pKa values of RS.[155] The theoretical contents of RS intercalated in RS–LDH was 22.5 wt%.[156] Briefly, it was determined on the basis of the net charge of RS (−3.53) calculated by its mole fractions ($RS^{3-}$ = 0.47 and $RS^{4-}$ = 0.53) at pH = 10.5, in which RS–LDH was formed during ion exchange reaction.

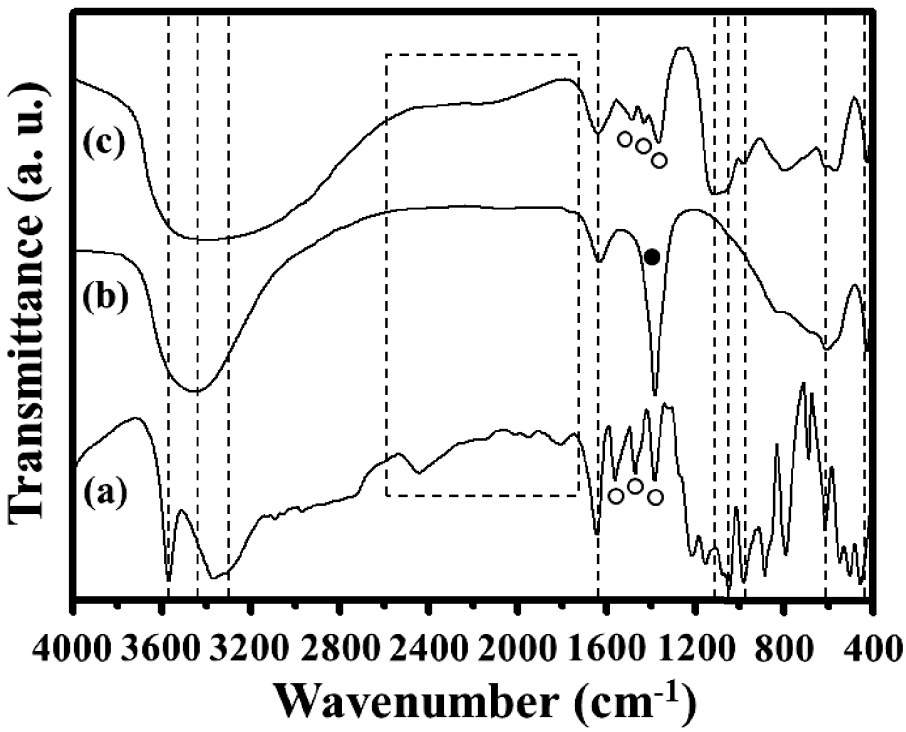


Figure 5.5. FT-IR spectra of (a) intact RS, (b) pristine LDH, and (c) RS-LDH.

### 5.4.2 *In vitro* Proliferation and ALP Activity

According to *in vitro* experiment with MG63 cells (Figure 5.6), when the same dose of RS was applied, both cell proliferation and alkaline phosphatase (ALP) activity were statistically significantly improved with the RS-LDH as compared with intact RS ($p < 0.05$). This could be ascribed to facilitated intracellular uptake of the drug-LDH nanohybrids[32, 74]: unlike negatively charged RS molecules, the RS-LDH was positively charged, which could be attracted to negatively charged cellular membranes, leading to favorable endocytosis *via* clathrin-mediated cellular uptake. The endocytosed RS-LDH should be degraded due to low pH of endosome (pH 4.5-5.5) in cells,[26, 74, 157] releasing the intercalated RS molecules. Under the conditions employed in this work, the RS-LDH were observed to be not cytotoxic.

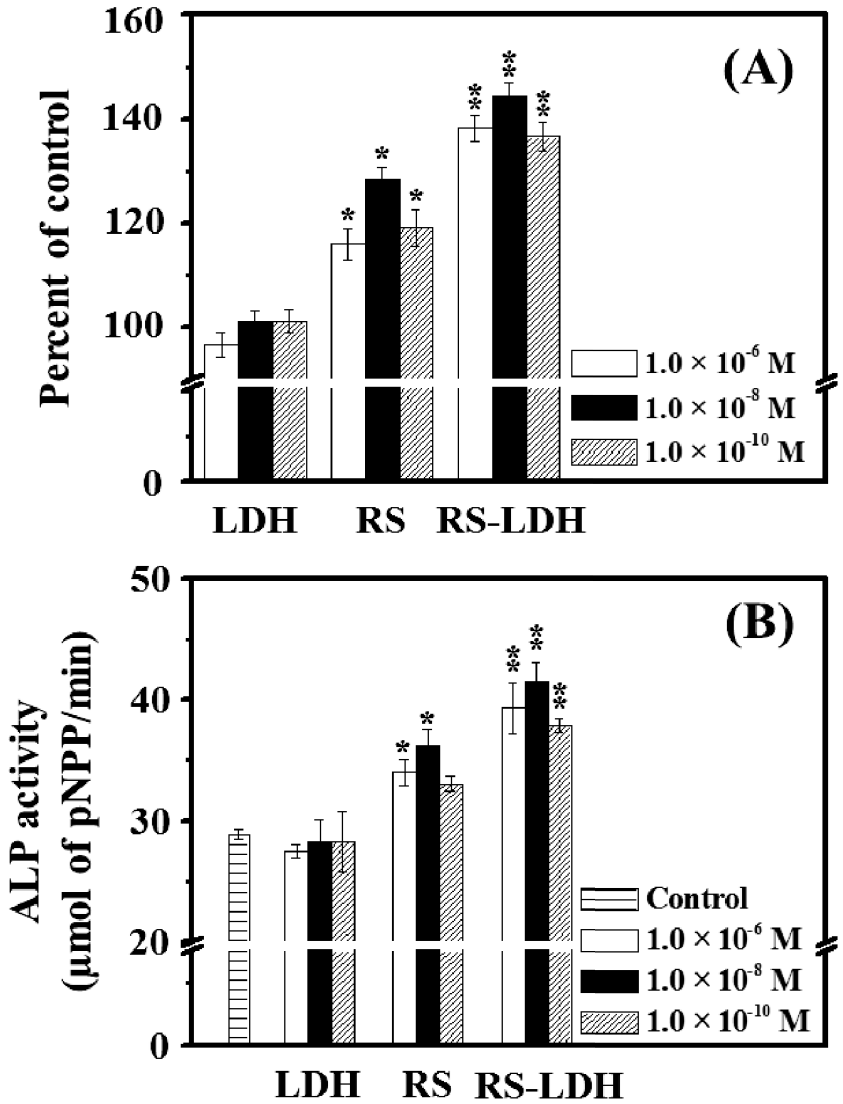


Figure 5.6. (A) *In vitro* proliferation and (B) ALP activity of MG63 cells treated with osteogenic media containing different concentrations of the pristine LDH, intact RS and RS–LDH for 3 days. For each sample type, at least three experiments were performed for statistics. *Intact RS was statistically significantly different from pristine LDH ($p < 0.05$). **RS–LDH was statistically significantly different from both pristine LDH and intact RS ($p < 0.05$).

### 5.4.3 Analysis of Theranostic Plates

As shown in Figure 5.7(A–D), I fabricated three distinct sheets: a 2.0–mm thick LDH sheet, 1.0–mm thick RS–LDH sheet, and 2.0–mm thick RS–LDH sheet, each formulated with a 1:5 mass ratio of PLGA and pristine LDH or RS–LDH, which were then attached on the top of the unmodified bioabsorbable bone plate (UP) to prepare the plates of LDH_P2 (i.e., the plate attached with the sheet containing pristine LDH without RS), RS–LDH_P1, and RS–LDH_P2, respectively. In this work, I cut a small piece out of a whole piece of the Inion plate in clinical use to prepare the UP (Figure 5.1). I shaped the sheets into a square–shaped frame with a hole at the center in order to not block the screw hole formed in the UP. Figure 5.7(E) depict optical images of the bioabsorbable plates without and with a theranostic RS–LDH sheet, respectively. As shown in the FE–SEM image of the RS–LDH sheet (Figure 5.7(F)), the RS–LDH nanoparticles were seen to be densely packed with being bound with PLGA. The loading amounts of RS were measured to be 6.61 ± 0.12 mg and 13.15 ± 0.16 mg per plate with the RS–LDH_P1 and RS–LDH_P2, respectively. The RS–LDH_P2 contained more RS than the RS–LDH_P1 as the sheet thickness increased from 1.0 mm to 2.0 mm.

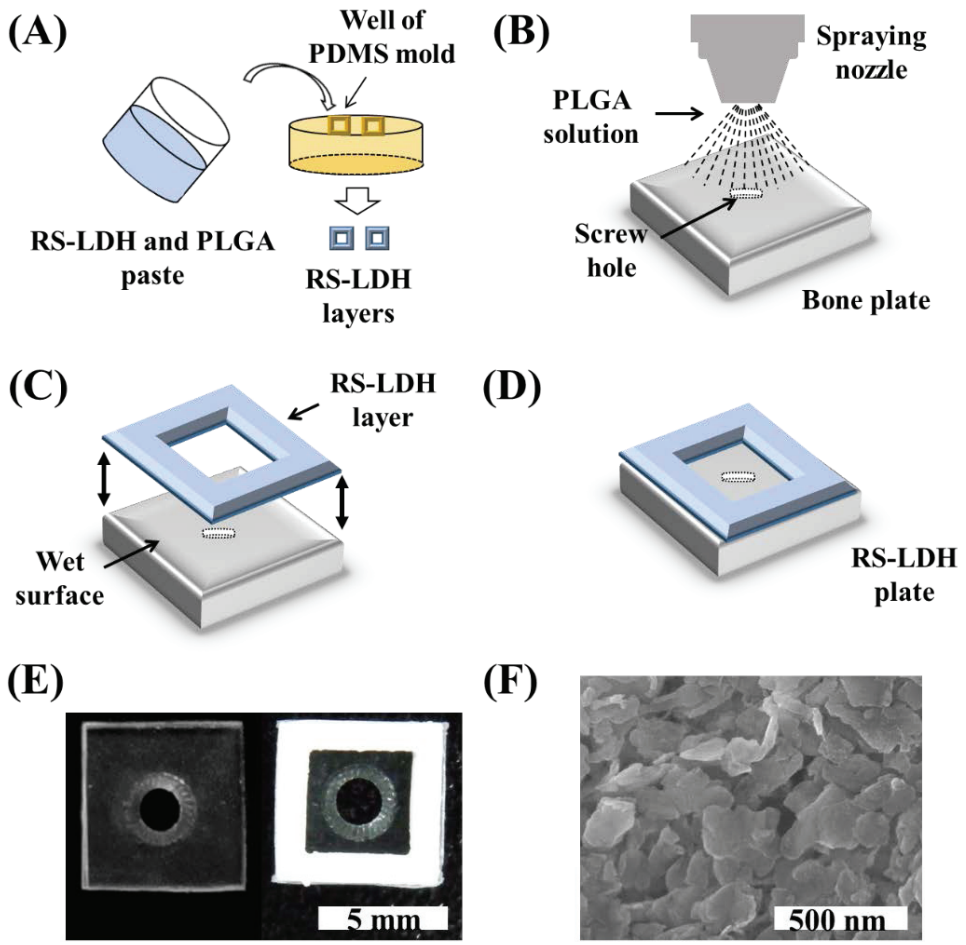


Figure 5.7. Schematic process for preparation of a theranostic plate. (A) RS-LDH sheets were separately prepared from the polydimethylsiloxane molds of square-shaped frame filled with a paste of RS-LDH and PLGA (5:1, w/w). (B) PLGA solution was sprayed on the surface of a bone plate and (C) the RS-LDH sheet was attached on top of it to finally give (D) a theranostic bone plate. (E) Optical images of the bioabsorbable bone fixation plates without and with a theranostic RS-LDH sheet. (F) FE-SEM image of the surface of a theranostic RS-LDH sheet.

### 5.4.4 *In vitro* Drug Release Study

Figure 5.8(A) shows the *in vitro* dissolution profiles of intact RS, RS-LDH, RS-LDH_P1, and RS-LDH_P2 in PBS at pH 7.4. With intact RS, it dissolved completely within 1 day due to its high aqueous solubility.[158] However, the drug was released in a sustained manner with the RS-LDH. About 2.5% RS was released during the first 3 days and after that, it was continously discharged at an average rate of 0.13%/day. This could be ascribed to the fact that the anions in PBS (chloride and phosphate ions), replaced the intercalated RS molecules. However, this mostly occurred at the edge of the LDH layers, which became narrow as the replacing anions in PBS were smller than the intercalated RS molecule to cause the zipping effect.[59] For this reason, the drug intercalated in the core of the LDH layers became more difficult to be freed, hence very slow drug release. With the theranostic plates, drug release was more retarded. The sheets were made of a blend of RS-LDH and PLGA, where the latter served as an additional diffusion barrier. From each theranostic plate, drug was released at a similar percent rate for 42 days, since the same composition ratio of RS-LDH and PLGA were employed to prepare both distinct types of the plates herein. However, the rate of drug release amount was higher with the RS-LDH_P2 (9.36 μg/day) than with the RS-LDH_P1 (6.00 μg/day) as more RS-LDH was contained in the thicker sheet of the RS-LDH_P2 (Figure 5.8(B)).

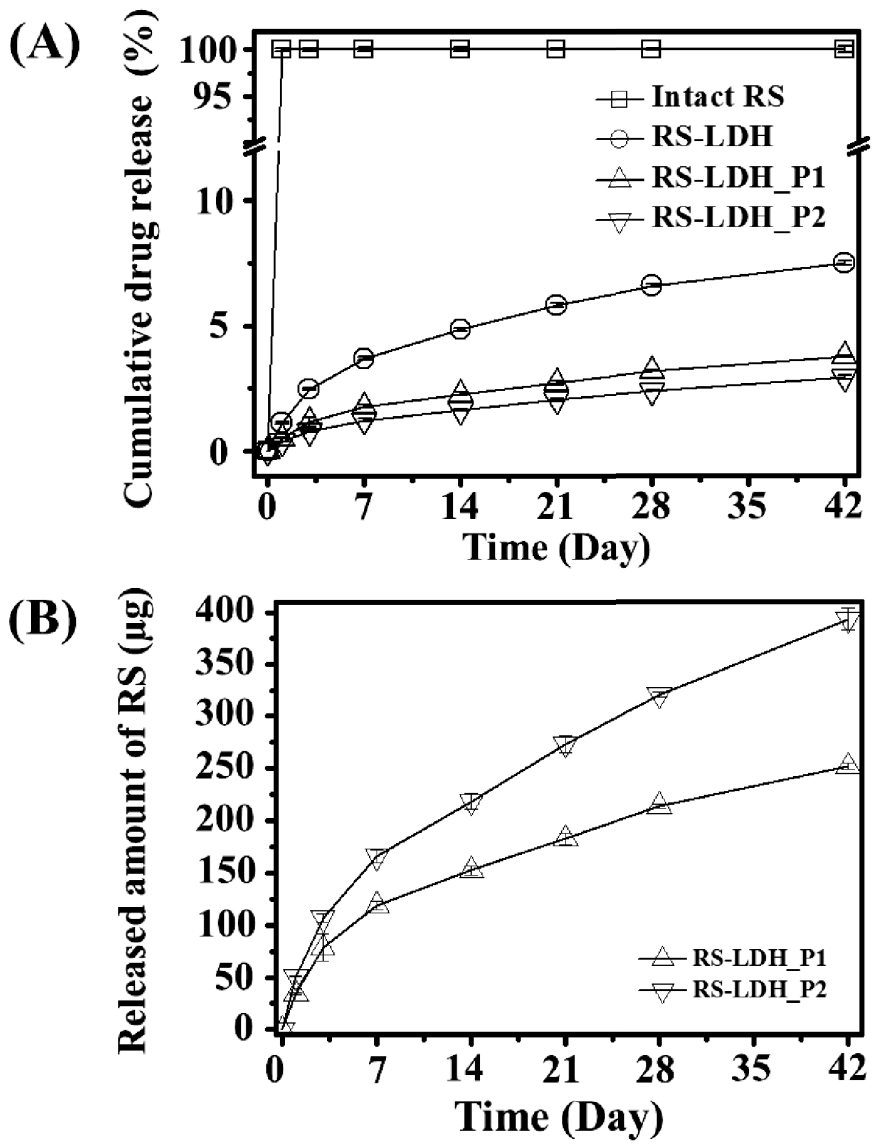


Figure 5.8. (A) *In vitro* drug release profiles of the intact RS, RS-LDH, RS-LDH_P1, and RS-LDH_P2 in pH 7.4 PBS for 42 days. (B) *In vitro* drug release profiles plotted in amounts with the RS-LDH_P1 and RS-LDH_P2 in pH 7.4 PBS for 42 days.

### 5.4.5 *In vitro* X-ray Visibility

To examine the X-ray visibility and its longevity, the RS-LDH_P1 and RS-LDH_P2, as well as the LDH_P2, were each immersed in pH 7.4 PBS at 37℃, and their X-ray images were obtained using a mobile C-arm at predetermined schedules for 42 days. Figure 5.9(A) shows the representative *in vitro* X-ray images of the LDH_P2, RS-LDH_P1, and RS-LDH_P2, where a distinctive square frame shape was observed with all plates during the whole tested period. Both LDH_P2 and RS-LDH_P2 showed a higher X-ray visibility than the RS-LDH_P1 due to a larger amount of the metal-containing LDH entrapped in the sheet. For all plates, as the time elapsed, the visibility became lower and the edge of the sheet became less distinctive, which could be ascribed to the swelling of the binder material, PLGA and its degradation to free the particles of LDH or RS-LDH. To confirm this, I quantitatively analyzed the images using densitometry measurements. Both LDH_P2 and RS-LDH_P2 exhibited statistically significantly higher densitometry values than the RS-LDH_P1 during the whole tested period ($p < 0.05$) (Figure 5.9(B)). The densitometry values were similar between the LDH_P2 and RS-LDH_P2 as the same amount of the LDH was used to prepare the X-ray visible sheet on the plate. For all plates, the densitometry values decreased with time, which is in good agreement with the images shown in Figure 5.9(A).

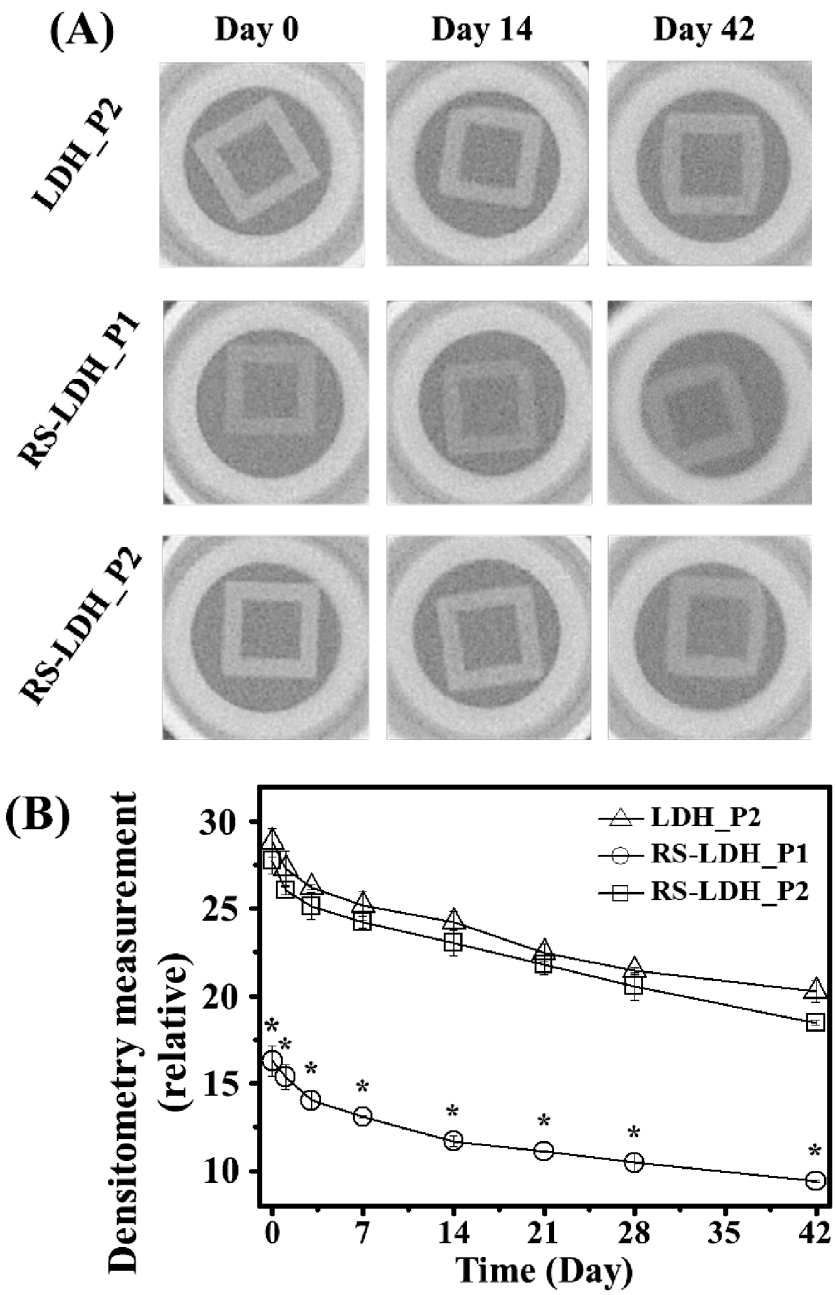


Figure 5.9. (A) Representative *in vitro* X-ray images and (B) densitometry measurements of the LDH_P2, RS-LDH_P1 and RS-LDH_P2 for a period of 42 days. *RS-LDH_P1 was statistically significantly different from both LDH_P2 and RS-LDH_P2 ($p < 0.05$).

### 5.4.6 *In vivo* X-ray Visibility

To evaluate *in vivo* radiopaque property, the plates prepared in this work were each fixed on a critically defected cranial bone sites of living animals and imaged *via* X-ray after 1, 2, 4, and 8 weeks. As shown in Figure 5.10(A), the RS-LDH_P1 and RS-LDH_P2, as well as the LDH_P2, showed a discernible image *via* X-ray. With the no treatment group, the plate was not visible as expected. In the UP group, i.e., the animal group fixed with an intact Inion plate, although the plate was present, it was not visible during a whole tested period due to the radiolucent property of the bioabsorbable polymeric plate. In this work, I also pursued that the prepared sheets be biodegradable, as designed with the original bone plate. At 1 week, a square-framed shape of the radiopaque sheet was highly discernible for all plates with the radiopaque sheet. As the time elapsed, the visibility continuously decreased until 4 weeks and the plates became not visible from 8 weeks. According to the densitometry measurements (Figure 5.10(B)), the LDH_P2 and RS-LDH_P2 showed statistically significantly higher value than the RS-LDH_P1 at 1 week ($p < 0.05$), ascribed to the thicker sheet on the LDH_P2 and RS-LDH_P2, i.e., more LDH with metals. The densitometry values also continuously decreased as the time elapsed, which became undetectably low from 8 weeks. The decrease in X-ray visibility could be ascribed again to swelling and degradation of PLGA, which freed the LDH or RS-LDH particles from the sheet. However, the theranostic plates herein were

X-ray visible in an acceptable level for up to 4 weeks, which could be considered sufficiently long to diagnose the possible loosening of a bone plate in clinical conditions.[108, 132, 133]

### 5.4.7 *In vivo* New Bone Formation

In order to evaluate the therapeutic effect, I analyzed a degree of *in vivo* new bone formation within the cranial bone defect treated with the plates herein using micro-computed tomography (μCT), as shown in Figure 5.11. For all groups, the new bone volume percent in defect continuously increased with time. Until 4 weeks after implantation, new bone volume percent was not very different among the groups. The RS-LDH_P2 group exhibited a higher new bone volume percent than the other groups, which, however, was not statistically significantly different. Notably, the effect of the RS-LDH on new bone formation became more evident from 8 weeks. At 8 and 12 weeks, the RS-LDH_P1 showed a higher new bone volume percent than the no treatment, UP and LDH_P2 groups and this was statistically significantly different from that of the no treatment group ($p < 0.05$). The best efficacy was observed with the RS-LDH_P2 group, where the new bone volume percent was statistically significantly higher than those of all other groups ($p < 0.05$). At 8 and 12 weeks, the RS-LDH_P2 group exhibited that new bone was formed in more than a half volume of an original defect (50.50 ± 6.37% and 61.90±8.11%, respectively), which was 2.6-times more

effective as compared with the no treatment group (16.13 ± 3.17% and 23.47 ± 7.14% at 8 and 12 weeks, respectively). From 8 weeks, due to the increase in RS-LDH amount, new bone volume percent of the RS-LDH_P2 was also evidently higher than that of the RS-LDH_P1 and the difference was statistically significant ($p < 0.05$).

The RS-LDH can release the intercalated drug in a sustained manner (Figure 5.8(A)) and thus, RS, a drug known to promote new bone formation,[82-84, 97, 159] could be exposed in a bone defect continuously during a period of healing process. The RS-LDH_P2 showed sustained release of RS for 42 days at an average rate of approximately 9.36 μg/day (Figure 5.8(B)), the daily dose of which was reported to effectively promote bone regeneration and be also safe to a large extent.[145, 160, 161] Moreover, the RS-LDH nanoparticles, when freed from the theranostic plate, were expected to further improve the efficacy of RS. According to our *in vitro* experiment with MG63 cells (Figure 5.6), when the same dose of RS was applied, both cell proliferation and ALP activity were improved with the RS-LDH as compared with intact RS. As a result, the RS-LDH_P2 exhibited significantly higher efficacy in new bone formation under the *in vivo* experimental conditions employed in this work.

To further confirm the therapeutic effect of the plates, I biopsied tissues of the cranial defect around the plates at 12 weeks after implantation and examined them on H&E staining, as shown in Figure 5.12(A). For the no treatment, UP and LDH_P2 groups, a small area of newly formed bone was observed mostly near the edge of the

cranial bone defect. In the RS-LDH_P1 group, more new bone tissues were observed, which, however, were still found mostly near both edges of the cranial bone defect. In the RS-LDH_P2 group, new bone formation was prominently observed within center of the defect, hence bridging both edges of the defected area. I also performed histomorphometric analysis to quantitatively assess new bone formation. As shown in Figure 5.12(B), the RS-LDH_P2 again exhibited the highest new bone area percent, which was statistically significantly different as compared with all other groups ($p < 0.05$).

### 5.4.8 Biocompatibility Evaluation

To assess the biocompatibility, I examined the images of biopsied tissues on H&E staining (Figure 5.12(A)). For all groups, lymphocytes, neutrophils, and other active inflammatory components were barely observed and no sign of necrosis and abscess was seen within the site of cranial bone defect. For the groups implanted with the plate, fibrous tissues were formed around the plate with thickness, ranging from 10 to 50 μm and prominent neovascularization was seen to reach into the area of muscle and over it. A few pigment laden macrophages were found along the surface of the plate. Overall, upon microscopic evaluation, there appeared to be no significant difference in inflammation degree between the RS-LDH loaded plates and the UP. This result implied good *in vivo* biocompatibility of the theranostic plates prepared in this work.

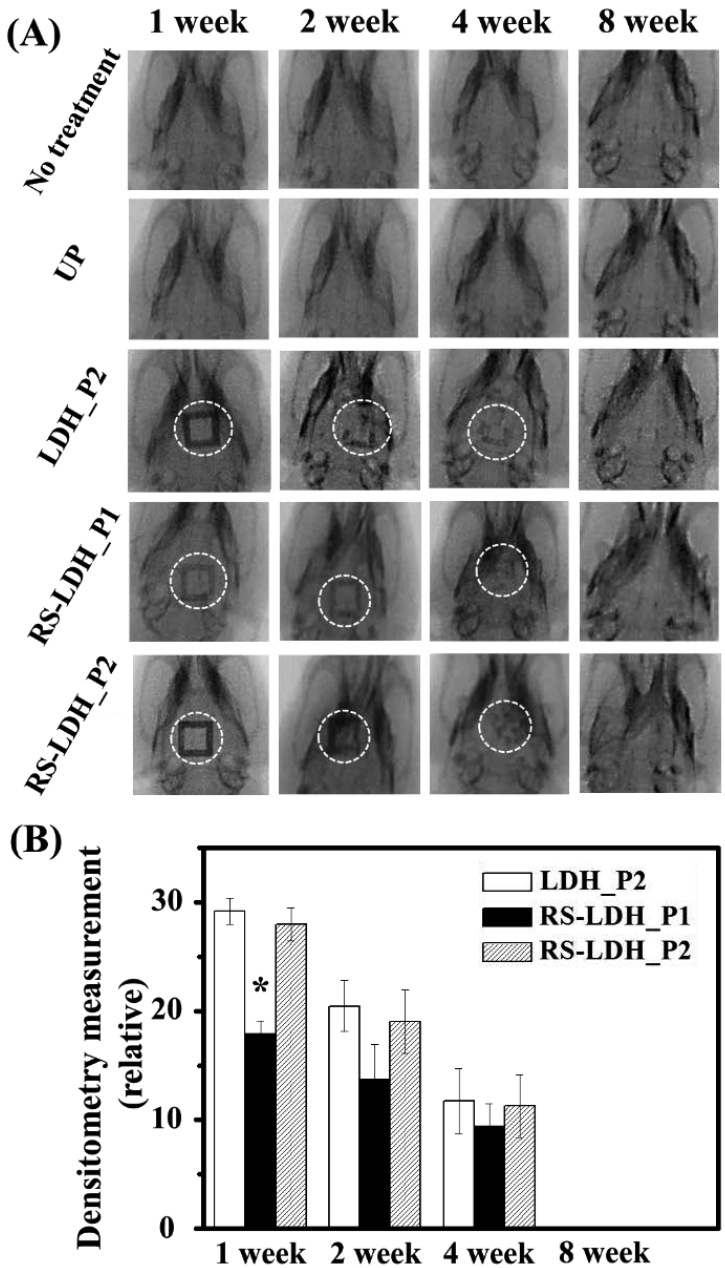


Figure 5.10. (A) Representative *in vivo* X-ray images and (B) densitometry measurements of the UP, LDH_P2, RS-LDH_P1 and RS-LDH_P2 implanted on a cranial bone defect in rats. The no treatment group was also imaged as control. *The RS-LDH_P1 group was statistically significantly different from both LDH_P2 and RS-LDH_P2 groups ($p < 0.05$).

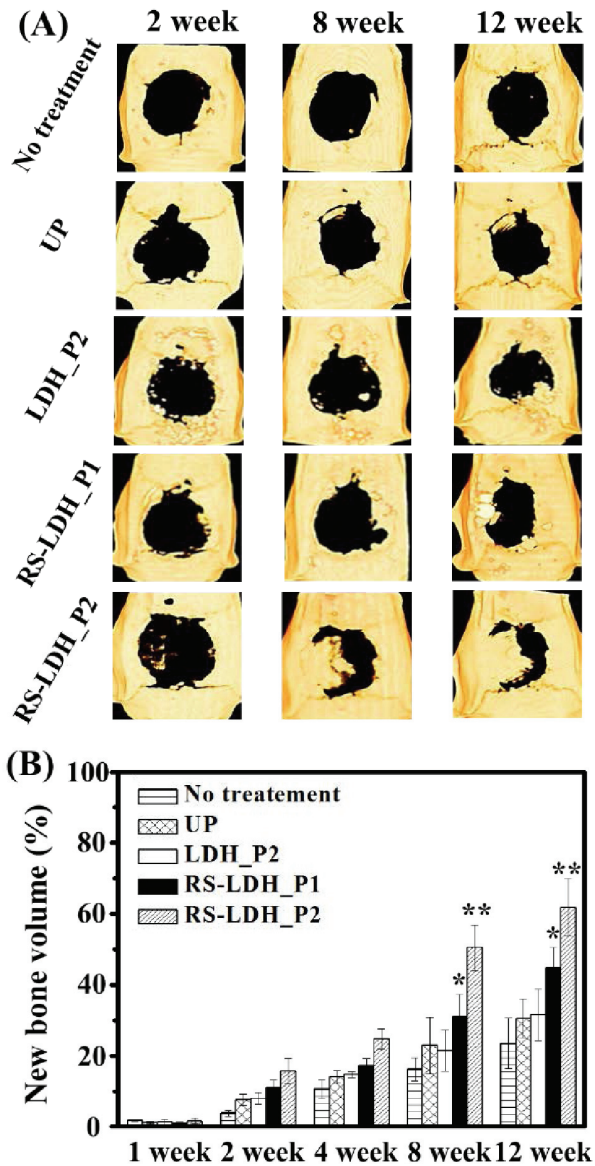


Figure 5.11. (A) Representative *in vivo* μCT images and (B) new bone volume percent in cranial bone defects treated with the UP, LDH_P2, RS-LDH_P1 and RS-LDH_P2. The no treatment group was also imaged as control. At 8 and 12 weeks, *The RS-LDH_P1 group was statistically significantly different from no treatment group ($p < 0.05$). **The RS-LDH_P2 group was statistically significantly different from all other different groups ($p < 0.05$).

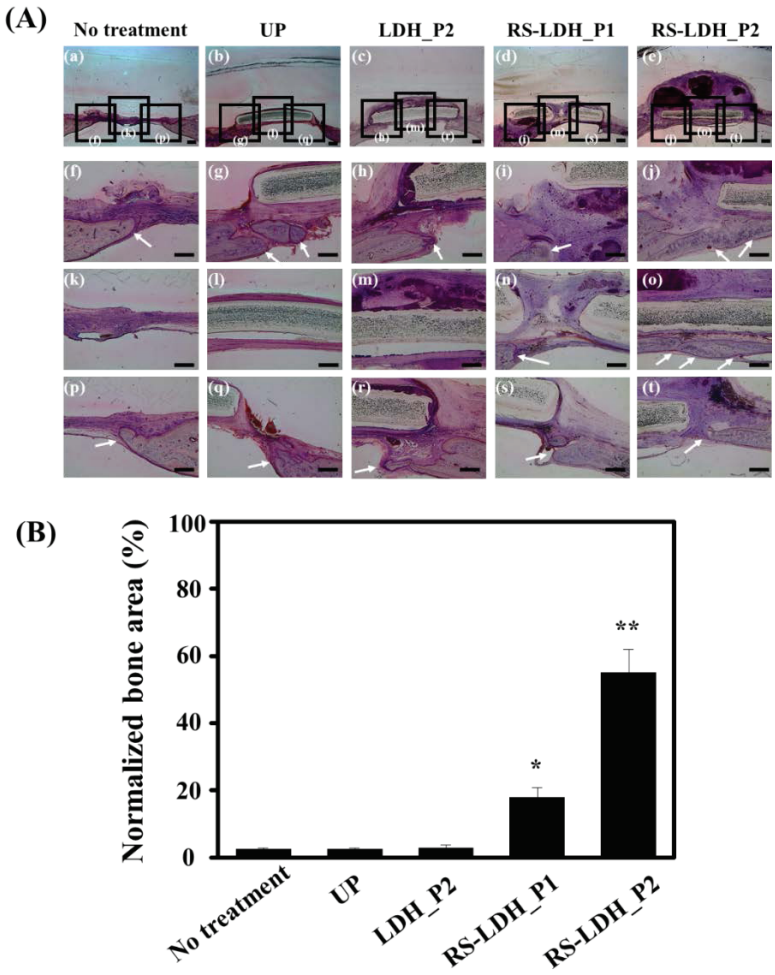


Figure 5.12. (A) Histological images from the tissues around the cranial bone defect obtained at 12 weeks after plate implantation. The arrows indicate the specific locations of new bone formation. The scale bars represent 100 μm. (B) Histomorphometric analysis on new bone formation in cranial defects of the animal groups with no treatment and the ones fixed with the UP, LDH_P2, RS-LDH_P1, and RS-LDH_P2 at 12 weeks after implantation. *The RS-LDH_P1 group was statistically significantly different from the no treatment, UP, and LDH_P2 groups. ** The RS-LDH_P2 group was statistically significantly different from all other different groups ($p < 0.05$).

## 5.5 Conclusion

In this study, I suggest a bioabsorbable polymeric bone plate enabled with both diagnostic and therapeutic functionalities by allowing both radiopaque and sustained drug release properties, respectively. For this, I proposed the RS-LDH nanohybrid as a theranostic agent, where a drug, RS, was intercalated into inorganic LDH *via* ion exchange reaction. In this work, the RS-LDH was prepared in form of a sheet with a biodegradable polymer, PLGA, which was then attached onto the clinically approved Inion bone plate to give the theranostic plate herein. Due to the presence of the metals in LDH, the theranostic plate provided with discernible *in vivo* images *via* X-ray for up to 4 weeks after implantation. Concurrently, bone regeneration was also significantly improved compared with the other control groups, which could be ascribed to a sustained drug release property of the theranostic plate herein. The theranostic plate was also proven to be biocompatible to a large extent, which was comparable to the Inion plate already approved in clinical use. Therefore, I conclude that a biodegradable bone plate in combined with the RS-LDH nanohybrids could be a promising system for theranostic ability in both X-ray diagnosis and expedited bone repair.

# Part V.

# Conclusion

# Chapter 6

## Conclusion and Perspectives

Many attempts have been made to develop effective diagnosis and therapy at the desired site of action, which is highly required for the treatment of diseases. However, this is often challenging due to low bioavailability, unwanted systemic exposure, and adverse side effects of a therapeutic agent or due to poor sensitivity and biocompatibility of a diagnostic agent. In this thesis, to address these shortcomings, I described novel multifunctional LDH based nanohybrids for highly effective diagnosis, therapy, and even theranosis.

In part 2, I examined drug intercalated LDH nanohybrids as therapeutic agent with controlled/sustained release properties and intracellular drug delivery behaviors, which thus improved drug

bioavailability. In chapter 2, I suggest a formulation of the drug–inorganic nanohybrid for transdermal controlled drug delivery. As I prepared the nanohybrid (i.e., FB–LDH) by intercalating a transdermal model drug, FB, into the LDH, the drug molecules could be well stabilized in the LDH layers. The nanohybrid can release the drug in a sustained manner, which can be better controlled with the presence of a macromolecule, possessing the same polarity comparable to the incorporated drug. According to the *in vitro* release experiments with the FB–LDH, the drug release could be facilitated with the presence of an anionic macromolecule, Eudragit® S–100, in the release media by expediting deintercalation of FB in the LDH lattices. The gel suspension of the nanohybrid can deliver the drug across the skin in a controlled manner, depending on the amount of an aqueous solution of an anionic macromolecule mixed with the gel suspension. As a result, an average lag time and steady state flux of the drug could be varied from 12.8 h and $\approx$ 3.28 $\mu g\ cm^{-2}\ h^{-1}$ to less than 1 h and $\approx$ 14.57 $\mu g\ cm^{-2}\ h^{-1}$, respectively. Therefore, I conclude that a gel suspension of the nanohybrid containing a tailored amount of an aqueous solution of macromolecules is a novel formulation for controlled delivery of a transdermal drug.

In chapter 3, I have successfully synthesized the X–ray single phasic AL–LDH with nanosized plate–like morphology by ion–exchange reaction in order to enhance the efficacy of AL. According to the cellular uptake studies, the intracellular accumulation of AL in MG63 cells treated with the AL–LDH was 10.6–fold higher than that

with intact AL for 1 h treatment. From the CLSM images, the ease of internalization of LDH was confirmed as the green fluorescence within the cells was not from the uptake of free FITC released from the FITC−LDH−$CO_3$, but from the uptake of the FITC−LDH−$CO_3$ itself. Furthermore, *in vitro* cell proliferation and ALP activity results showed that the incorporation of AL into LDH could enhance efficacy of AL compared to intact AL, although LDH itself had no effect on proliferation and osteogenic differentiation of MG63 cells. Therefore, the present AL−LDH could be considered as a promising drug delivery system for improving efficacy of AL.

In part 3, I developed a bioabsorbable bone plate in combined with a radiopaque sheet, which was composed of LMH and PLGA as radiopaque and binder materials, respectively, since the bone plate present challenges in X−ray imaging, which is often needed to monitor their proper positioning after fixation, due to its radiolucent property. The degree of X−ray visibility could be varied depending on the metal compositions of LMHs in the radiopaque sheets, and the sheet could be degraded and disappeared gradually along with the original Inion plate. The release of LMH particles during degradation of radiopaque sheet could be modulated to avoid or minimize possible toxicity. In this work, the *in vivo* X−ray images from the Zn−HDS_P was more discernible than those from the MgAl−LDH_P and ZnAl−LDH_P during the whole tested period since the higher X−ray attenuation coefficients and contents of metals in Zn−HDS than those of ZnAl−LDH and MgAl−LDH. According to the *in vivo* experiments

with rats, the radiopaque LMH plates exhibited good biocompatibility, similar to that of the Inion plate already in clinical use. Therefore, I concluded that a biodegradable bone plate assembled with a LMH-based, radiopaque sheet has a great potential to be used as an orthopaedic fixation system to enable X-ray imaging diagnosis.

In part 4, I suggest a bioabsorbable polymeric bone plate enabled with both diagnostic and therapeutic functionalities by allowing both radiopaque and sustained drug release properties, respectively. For this, I proposed the RS-LDH nanohybrid as a theranostic agent, where a drug, RS, was intercalated into inorganic LDH *via* ion exchange reaction. In this work, the RS-LDH was prepared in form of a sheet with a biodegradable polymer, PLGA, which was then attached onto the clinically approved Inion bone plate to give the theranostic plate herein. Due to the presence of the metals in LDH, the theranostic plate provided with discernible *in vivo* images *via* X-ray for up to 4 weeks after implantation. Concurrently, bone regeneration was also significantly improved compared with the other control groups, which could be ascribed to a sustained drug release property of the theranostic plate herein. The theranostic plate was also proven to be biocompatible to a large extent, which was comparable to the Inion plate already approved in clinical use. Therefore, I conclude that a biodegradable bone plate in combined with the RS-LDH nanohybrids could be a promising system for theranostic ability in both X-ray diagnosis and expedited bone repair.

According to the obtained results, LDH based nanohybrids

have many unique features, such as controlled/sustained drug release property, intracellular uptake behaviour, radiopaque property, and biocompatibility, which could be used as efficient diagnostic, therapeutic, and theranostic agents. These chemically well-defined LDH based nanohybrids can have initiated new interdisciplinary developments on biomedical applications. It is expected that the biomedical applications using LDH based nanohybrids will continuously increase and prompt to exchange ideas, which ultimately leading to further developments. Moreover, innovative designs of the new LDH based hybrid systems with will take a step forward to clinical use and consequently open new drug delivery markets in the near future. In this regard, I hope that this study contributes to a research on the development of an LDH based nanohybrid system to expand its applications in biomedical fields, such as regenerative tissue engineering, theranosis, personalized medicine, pharmaceutics, implants, etc., for the better treatment of various diseases, thereby improving quality of life.

# References

[1] R. Esfand, D.A. Tomalia, Poly (amidoamine)(PAMAM) dendrimers: from biomimicry to drug delivery and biomedical applications, Drug discovery today, 6 (2001) 427-436.
[2] Y.J. Jun, M.K. Park, V.B. Jadhav, J.H. Song, S.W. Chae, H.J. Lee, K.S. Park, B. Jeong, J.H. Choy, Y.S. Sohn, Tripodal amphiphiles tunable for self-assembly to polymersomes, Journal of Controlled Release, 142 (2010) 132-137.
[3] H.K. Han, H.J. Shin, D.H. Ha, Improved oral bioavailability of alendronate via the mucoadhesive liposomal delivery system, European Journal of Pharmaceutical Sciences, 46 (2012) 500-507.
[4] A.K. Gupta, M. Gupta, Synthesis and surface engineering of iron oxide nanoparticles for biomedical applications, Biomaterials, 26 (2005) 3995-4021.
[5] H. Otsuka, Y. Nagasaki, K. Kataoka, PEGylated nanoparticles for biological and pharmaceutical applications, Adv Drug Deliver Rev, 64 (2012) 246-255.
[6] Q. Wang, D. O'Hare, Recent Advances in the Synthesis and Application of Layered Double Hydroxide (LDH) Nanosheets, Chem Rev, 112 (2012) 4124-4155.
[7] J. Portier, J.H. Choy, M.A. Subramanian, Inoganic-organic-hybrids as precursors to functional materials, Int J Inorg Mater, 3 (2001) 581-592.
[8] S.M. Paek, J.M. Oh, J.H. Choy, A Lattice-Engineering Route to Heterostructured Functional Nanohybrids, Chem-Asian J, 6 (2011) 324-338.
[9] J.M. Oh, T.T. Biswick, J.H. Choy, Layered nanomaterials for green materials, J Mater Chem, 19 (2009) 2553-2563.
[10] F. Leroux, C. Taviot-Gueho, Fine tuning between organic and inorganic host structure: new trends in layered double hydroxide hybrid assemblies, J Mater Chem, 15 (2005) 3628-3642.
[11] W.M. Kriven, S.Y. Kwak, M.A. Wallig, J.H. Choy, Bio-resorbable nanoceramics for gene and drug delivery, Mrs Bull, 29 (2004) 33-37.
[12] P. Hagenmuller, Intercalation chemistry and chemical bonding, J Phys Chem Solids, 59 (1998) 503-506.
[13] J.H. Choy, Intercalative route to heterostructured nanohybrid, J Phys Chem Solids, 65 (2004) 373-383.
[14] J.H. Choy, J.S. Park, S.Y. Kwak, Y.J. Jeong, Y.S. Han, Layered double hydroxide as gene reservoir, Mol Cryst Liq Cryst, 341 (2000) 1229-1233.
[15] J.H. Choy, S.Y. Kwak, J.S. Park, Y.J. Jeong, J. Portier, Intercalative nanohybrids of nucleoside monophosphates and DNA in layered metal hydroxide, J Am Chem Soc, 121 (1999) 1399-1400.
[16] E. Ruiz-Hitzky, P. Aranda, M. Darder, G. Rytwo, Hybrid materials based on clays for environmental and biomedical applications, J Mater Chem, 20 (2010) 9306-9321.
[17] J.H. Yang, Y.S. Han, M. Park, T. Park, S.J. Hwang, J.H. Choy, New inorganic-based drug delivery system of indole-3-acetic acid-layered metal

hydroxide nanohybrids with controlled release rate, Chem Mater, 19 (2007) 2679-2685.
[18] D.H. Park, S.J. Hwang, J.M. Oh, J.H. Yang, J.H. Choy, Polymer-inorganic supramolecular nanohybrids for red, white, green, and blue applications, Prog Polym Sci, 38 (2013) 1442-1486.
[19] M.H. Kim, D.H. Park, J.H. Yang, Y.B. Choy, J.H. Choy, Drug-inorganic-polymer nanohybrid for transdermal delivery, Int J Pharmaceut, 444 (2013) 120-127.
[20] K.M. Kim, J.H. Kang, A. Vinu, J.H. Choy, J.M. Oh, Inorganic Nanomedicines and their Labeling for Biological Imaging, Curr Top Med Chem, 13 (2013) 488-503.
[21] D.H. Park, G. Choi, J.H. Choy, Bio-Layered Double Hydroxides Nanohybrids for Theranostics Applications, Struct Bond, 166 (2015) 137-175.
[22] J.M. Oh, D.H. Park, S.J. Choi, J.H. Choy, LDH Nanocontainers as Bio-Reservoirs and Drug Delivery Carriers, Recent Pat Nanotech, 6 (2012) 200-217.
[23] J.H. Hubbell, S.M. Seltzer, Tables of X-ray mass attenuation coefficients and mass energy-absorption coefficients 1 keV to 20 MeV for elements Z= 1 to 92 and 48 additional substances of dosimetric interest, in, National Inst. of Standards and Technology-PL, Gaithersburg, MD (United States). Ionizing Radiation Div., 1995.
[24] S.B. Yu, A.D. Watson, Metal-based X-ray contrast media, Chem Rev, 99 (1999) 2353-2377.
[25] L.J. Wang, H.Y. Xing, S.J. Zhang, Q.G. Ren, L.M. Pan, K. Zhang, W.B. Bu, X.P. Zheng, L.P. Zhou, W.J. Peng, Y.Q. Hua, J.L. Shi, A Gd-doped Mg-Al-LDH/Au nanocomposite for CT/MR bimodal imagings and simultaneous drug delivery, Biomaterials, 34 (2013) 3390-3401.
[26] J.H. Choy, S.Y. Kwak, Y.J. Jeong, J.S. Park, Inorganic layered double hydroxides as nonviral vectors, Angew Chem Int Edit, 39 (2000) 4042-4045.
[27] A.U. Kura, M.Z. Hussein, S. Fakurazi, P. Arulselvan, Layered double hydroxide nanocomposite for drug delivery systems; bio-distribution, toxicity and drug activity enhancement, Chem Cent J, 8 (2014).
[28] J.M. Oh, S.Y. Kwak, J.H. Choy, Intracrystalline structure of DNA molecules stabilized in the layered double hydroxide, J Phys Chem Solids, 67 (2006) 1028-1031.
[29] J.H. Choy, Y.H. Son, Intercalation of vitamer into LDH and their controlled release properties, B Kor Chem Soc, 25 (2004) 122-126.
[30] S.D. Li, J.H. Li, C.J. Wang, Q. Wang, M.Z. Cader, J. Lu, D.G. Evans, X. Duan, D. O'Hare, Cellular uptake and gene delivery using layered double hydroxide nanoparticles, J Mater Chem B, 1 (2013) 61-68.
[31] Z.P. Xu, G.Q. Lu, Layered double hydroxide nanomaterials as potential cellular drug delivery agents, Pure Appl Chem, 78 (2006) 1771-1779.
[32] J.M. Oh, S.J. Choi, S.T. Kim, J.H. Choy, Cellular uptake mechanism of an inorganic nanovehicle and its drug conjugates: Enhanced efficacy due to clathrin-mediated endocytosis, Bioconjugate Chem, 17 (2006) 1411-1417.
[33] S.J. Choi, G.E. Choi, J.M. Oh, Y.J. Oh, M.C. Park, J.H. Choy, Anticancer drug encapsulated in inorganic lattice can overcome drug resistance, J Mater

Chem, 20 (2010) 9463-9469.
[34] Z. Gu, H.L. Zuo, L. Li, A.H. Wu, Z.P. Xu, Pre-coating layered double hydroxide nanoparticles with albumin to improve colloidal stability and cellular uptake, J Mater Chem B, 3 (2015) 3331-3339.
[35] S.J. Choi, J.H. Choy, Layered double hydroxide nanoparticles as target-specific delivery carriers: uptake mechanism and toxicity, Nanomedicine-Uk, 6 (2011) 803-814.
[36] F.Z. Lv, L.N. Xu, Y.H. Zhang, Z.L. Meng, Layered Double Hydroxide Assemblies with Controllable Drug Loading Capacity and Release Behavior as well as Stabilized Layer-by-Layer Polymer Multilayers, Acs Appl Mater Inter, 7 (2015) 19104-19111.
[37] Q.S. Zheng, Y.L. Hao, P.R. Ye, L.Q. Guo, H.Y. Wu, Q.Q. Guo, J.Z. Jiang, F.F. Fu, G.N. Chen, A pH-responsive controlled release system using layered double hydroxide (LDH)-capped mesoporous silica nanoparticles, J Mater Chem B, 1 (2013) 1644-1648.
[38] G. Choi, J.H. Lee, Y.J. Oh, Y. Bin Choy, M.C. Park, H.C. Chang, J.H. Choy, Inorganic-polymer nanohybrid carrier for delivery of a poorly-soluble drug, ursodeoxycholic acid, Int J Pharmaceut, 402 (2010) 117-122.
[39] P.K. Zhao, Y.Y. Liu, L. Xiao, H.B. Deng, Y.M. Du, X.W. Shi, Electrochemical deposition to construct a nature inspired multilayer chitosan/layered double hydroxides hybrid gel for stimuli responsive release of protein, J Mater Chem B, 3 (2015) 7577-7584.
[40] A.I. Khan, L.X. Lei, A.J. Norquist, D. O'Hare, Intercalation and controlled release of pharmaceutically active compounds from a layered double hydroxide, Chemical Communications, (2001) 2342-2343.
[41] J.D. Enderle, J.D. Bronzino, Introduction to biomedical engineering, Academic press, 2012.
[42] R.P. Patel, G. Patel, A. Baria, Formulation and evaluation of transdermal patch of aceclofenac, International Journal of Drug Delivery, 1 (2009).
[43] A. Shivaraj, R.P. Selvam, T.T. Mani, T. Sivakumar, Design and evaluation of transdermal drug delivery of ketotifen fumarate, Int. J. Pharm. Biomed. Res, 1 (2010) 42-47.
[44] M.R. Prausnitz, S. Mitragotri, R. Langer, Current status and future potential of transdermal drug delivery, Nat Rev Drug Discov, 3 (2004) 115-124.
[45] M.R. Prausnitz, R. Langer, Transdermal drug delivery, Nat Biotechnol, 26 (2008) 1261-1268.
[46] S. Prodduturi, N. Sadrieh, A.M. Wokovich, W.H. Doub, B.J. Westenberger, L. Buhse, Transdermal Delivery of Fentanyl from Matrix and Reservoir Systems: Effect of Heat and Compromised Skin, J Pharm Sci-Us, 99 (2010) 2357-2366.
[47] J. Hadgraft, M.E. Lane, Passive transdermal drug delivery systems, American Journal of Drug Delivery, 4 (2006) 153-160.
[48] S. Ida, C. Ogata, D. Shiga, K. Izawa, K. Ikeue, Y. Matsumoto, Dynamic control of photoluminescence for self-assembled nanosheet films intercalated with lanthanide ions by using a photoelectrochemical reaction, Angew Chem Int Edit, 47 (2008) 2480-2483.

[49] M. Osada, T. Sasaki, Exfoliated oxide nanosheets: new solution to nanoelectronics, J Mater Chem, 19 (2009) 2503-2511.
[50] I. Rousselot, C. Taviot-Guého, F. Leroux, P. Léone, P. Palvadeau, J.-P. Besse, Insights on the structural chemistry of hydrocalumite and hydrotalcite-like materials: investigation of the series Ca 2 M 3+ (OH) 6 Cl· 2H 2 O (M 3+ : Al 3+ , Ga 3+ , Fe 3+ , and Sc 3+ ) by X-ray powder diffraction, Journal of Solid State Chemistry, 167 (2002) 137-144.
[51] J.M. Oh, D.H. Park, J.H. Choy, Integrated bio-inorganic hybrid systems for nano-forensics, Chem Soc Rev, 40 (2011) 583-595.
[52] L. Desigaux, M. Ben Belkacem, P. Richard, J. Cellier, P. Leone, L. Cario, F. Leroux, C. Taviot-Gueho, B. Pitard, Self-assembly and characterization of layered double hydroxide/DNA hybrids, Nano Lett, 6 (2006) 199-204.
[53] D.G. Evans, D.A. Xue, Preparation of layered double hydroxides and their applications as additives in polymers, as precursors to magnetic materials and in biology and medicine, Chemical Communications, (2006) 485-496.
[54] S.J. Choi, J.M. Oh, J.H. Choy, Human-related application and nanotoxicology of inorganic particles: complementary aspects, J Mater Chem, 18 (2008) 615-620.
[55] S.J. Choi, J.H. Choy, Effect of physico-chemical parameters on the toxicity of inorganic nanoparticles, J Mater Chem, 21 (2011) 5547-5554.
[56] A. Burgos, M.P. Busquier, J.G. Reino, J.L. Ferreiro, F. Navarro, J. Valverde, E. Moreno, Double-blind, double-dummy comparative study of local action transcutaneous flurbiprofen (flurbiprofen LAT) versus piketoprofen cream in the treatment of extra-articular rheumatism, Clin Drug Invest, 21 (2001) 95-102.
[57] Z.G. Gao, H.G. Choi, H.J. Shin, K.M. Park, S.J. Lim, K.J. Hwang, C.K. Kim, Physicochemical characterization and evaluation of a microemulsion system for oral delivery of cyclosporin A, Int J Pharmaceut, 161 (1998) 75-86.
[58] M.J. Lawrence, G.D. Rees, Microemulsion-based media as novel drug delivery systems, Adv Drug Deliver Rev, 45 (2000) 89-121.
[59] J.Y. Kim, J.H. Yang, J.H. Lee, G. Choi, D.H. Park, M.R. Jo, S.J. Choi, J.H. Choy, 2D Inorganic-Antimalarial Drug-Polymer Hybrid with pH-Responsive Solubility, Chem-Asian J, 10 (2015) 2264-2271.
[60] A. Kogan, N. Garti, Microemulsions as transdermal drug delivery vehicles, Adv Colloid Interfac, 123 (2006) 369-385.
[61] P. Balakrishnan, B.J. Lee, D.H. Oh, J.O. Kim, Y.I. Lee, D.D. Kim, J.P. Jee, Y.B. Lee, J.S. Woo, C.S. Yong, H.G. Choi, Enhanced oral bioavailability of Coenzyme Q(10) by self-emulsifying drug delivery systems, Int J Pharmaceut, 374 (2009) 66-72.
[62] V.R. Cunha, P.A. Petersen, M.B. Goncalves, H.M. Petrilli, C. Taviot-Gueho, F. Leroux, M.L. Temperini, V.R. Constantino, Structural, spectroscopic (NMR, IR, and Raman), and DFT investigation of the self-assembled nanostructure of pravastatin-LDH (Layered Double Hydroxides) systems, Chem Mater, 24 (2012) 1415-1425.
[63] T.J. Franz, Percutaneous absorption. On the relevance of in vitro data, Journal of Investigative Dermatology, 64 (1975) 190-195.

[64] M. Meyn, K. Beneke, G. Lagaly, Anion-exchange reactions of layered double hydroxides, Inorganic Chemistry, 29 (1990) 5201-5207.
[65] B. Li, J. He, D.G. Evans, X. Duan, Inorganic layered double hydroxides as a drug delivery system—intercalation and in vitro release of fenbufen, Appl Clay Sci, 27 (2004) 199-207.
[66] V. Rives, F. Labajos, R. Trujillano, E. Romeo, C. Royo, A. Monzon, Acetylene hydrogenation on Ni-Al-Cr oxide catalysts: the role of added Zn, Appl Clay Sci, 13 (1998) 363-379.
[67] G.Y. Berguig, A.J. Convertine, S. Frayo, H.B. Kern, E. Procko, D. Roy, S. Srinivasan, D.H. Margineantu, G. Booth, M.C. Palanca-Wessels, D. Baker, D. Hockenbery, O.W. Press, P.S. Stayton, Intracellular Delivery System for Antibody-Peptide Drug Conjugates, Mol Ther, 23 (2015) 907-917.
[68] M.B. Kryger, S.L. Pedersen, B.M. Wohl, A.N. Zelikin, Tools of gene transfer applied to the intracellular delivery of non-nucleic acid polyanionic drugs, Chem Commun, (2016).
[69] L. Xiong, X. Du, B.Y. Shi, J.X. Bi, F. Kleitz, S.Z. Qiao, Tunable stellate mesoporous silica nanoparticles for intracellular drug delivery, J Mater Chem B, 3 (2015) 1712-1721.
[70] M.Q. Zhao, Q. Zhang, J.Q. Huang, F. Wei, Hierarchical Nanocomposites Derived from Nanocarbons and Layered Double Hydroxides - Properties, Synthesis, and Applications, Adv Funct Mater, 22 (2012) 675-694.
[71] Z.P. Xu, Q.H. Zeng, G.Q. Lu, A.B. Yu, Inorganic nanoparticles as carriers for efficient cellular delivery, Chem Eng Sci, 61 (2006) 1027-1040.
[72] Y.M. Kuo, Y. Kuthati, R.K. Kankala, P.R. Wei, C.F. Weng, C.L. Liu, P.J. Sung, C.Y. Mou, C.H. Lee, Layered double hydroxide nanoparticles to enhance organ-specific targeting and the anti-proliferative effect of cisplatin, J Mater Chem B, 3 (2015) 3447-3458.
[73] R. Ma, Z.G. Wang, L. Yan, X.F. Chen, G.Y. Zhu, Novel Pt-loaded layered double hydroxide nanoparticles for efficient and cancer-cell specific delivery of a cisplatin prodrug, J Mater Chem B, 2 (2014) 4868-4875.
[74] Z.P. Xu, M. Niebert, K. Porazik, T.L. Walker, H.M. Cooper, A.P.J. Middelberg, P.P. Gray, P.F. Bartlett, G.Q. Lu, Subcellular compartment targeting of layered double hydroxide nanoparticles, Journal of Controlled Release, 130 (2008) 86-94.
[75] J.H. Choy, S.Y. Kwak, J.S. Park, Y.J. Jeong, Cellular uptake behavior of [gamma-P-32] labeled ATP-LDH nanohybrids, J Mater Chem, 11 (2001) 1671-1674.
[76] L. Yan, W. Chen, X.Y. Zhu, L.B. Huang, Z.G. Wang, G.Y. Zhu, V.A.L. Roy, K.N. Yu, X.F. Chen, Folic acid conjugated self-assembled layered double hydroxide nanoparticles for high-efficacy-targeted drug delivery, Chem Commun, 49 (2013) 10938-10940.
[77] A.I. Khan, D. O'Hare, Intercalation chemistry of layered double hydroxides: recent developments and applications, J Mater Chem, 12 (2002) 3191-3198.
[78] R.G.G. Russell, M.J. Rogers, Bisphosphonates: From the laboratory to the clinic and back again, Bone, 25 (1999) 97-106.
[79] G.A. Rodan, T.J. Martin, Therapeutic approaches to bone diseases,

Science, 289 (2000) 1508-1514.
[80] J.F. Bukowski, C.C. Dascher, H. Das, Alternative bisphosphonate targets and mechanisms of action, Biochem Bioph Res Co, 328 (2005) 746-750.
[81] K.L. Kavanagh, K.D. Guo, J.E. Dunford, X.Q. Wu, S. Knapp, F.H. Ebetino, M.J. Rogers, R.G.G. Russell, U. Oppermann, The molecular mechanism of nitrogen-containing bisphosphonates as anti osteoporosis drugs, P Natl Acad Sci USA, 103 (2006) 7829-7834.
[82] Y. Xiong, H.J. Yang, J. Feng, Z.L. Shi, L.D. Wu, Effects of Alendronate on the Proliferation and Osteogenic Differentiation of MG-63 Cells, J Int Med Res, 37 (2009) 407-416.
[83] G.G. Reinholz, B. Getz, L. Pederson, E.S. Sanders, M. Subramaniam, J.N. Ingle, T.C. Spelsberg, Bisphosphonates directly regulate cell proliferation, differentiation, and gene expression in human osteoblasts, Cancer Res, 60 (2000) 6001-6007.
[84] F. von Knoch, C. Jaquiery, M. Kowalsky, S. Schaeren, C. Alabre, I. Martin, H.E. Rubash, A.S. Shanbhag, Effects of bisphosphonates on proliferation and osteoblast differentiation of human bone marrow stromal cells, Biomaterials, 26 (2005) 6941-6949.
[85] M. Fazil, S. Baboota, J.K. Sahni, Ameeduzzafar, J. Ali, Bisphosphonates: therapeutics potential and recent advances in drug delivery, Drug Deliv, 22 (2015) 1-9.
[86] M.J. Rogers, New insights into the molecular mechanisms of action of bisphosphonates, Current pharmaceutical design, 9 (2003) 2643-2658.
[87] M. Chakraborti, J.K. Jackson, D. Plackett, D.M. Brunette, H.M. Burt, Drug intercalation in layered double hydroxide clay: Application in the development of a nanocomposite film for guided tissue regeneration, Int J Pharmaceut, 416 (2011) 305-313.
[88] J. Kuljanin, I. Jankovic, J. Nedeljkovic, D. Prstojevic, V. Marinkovic, Spectrophotometric determination of alendronate in pharmaceutical formulations via complex formation with Fe(III) ions, J Pharmaceut Biomed, 28 (2002) 1215-1220.
[89] N. Itano, F. Atsumi, T. Sawai, Y. Yamada, O. Miyaishi, T. Senga, M. Hamaguchi, K. Kimata, Abnormal accumulation of hyaluronan matrix diminishes contact inhibition of cell growth and promotes cell migration, P Natl Acad Sci USA, 99 (2002) 3609-3614.
[90] D.-H. Park, J.-H. Yang, A. Vinu, A. Elzatahry, J.-H. Choy, X-ray diffraction and X-ray absorption spectroscopic analyses for intercalative nanohybrids with low crystallinity, Arabian Journal of Chemistry, (2015).
[91] F. Benyettou, I. Chebbi, L. Motte, O. Seksek, Magnetoliposome for alendronate delivery, J Mater Chem, 21 (2011) 4813-4820.
[92] F. Benyettou, R. Rezgui, F. Ravaux, T. Jaber, K. Blumer, M. Jouiad, L. Motte, J.C. Olsen, C. Platas-Iglesias, M. Magzoub, A. Trabolsi, Synthesis of silver nanoparticles for the dual delivery of doxorubicin and alendronate to cancer cells, J Mater Chem B, 3 (2015) 7237-7245.
[93] X.M. Liu, S.X. Qu, X. Lu, X. Ge, Y. Leng, Time-of-flight secondary ion mass spectrometry study on the distribution of alendronate sodium in drug-loaded ultra-high molecular weight polyethylene, Biomed Mater, 4 (2009).

[94] F. Errassifi, S. Sarda, A. Barroug, A. Legrouri, H. Sfihi, C. Rey, Infrared, Raman and NMR investigations of risedronate adsorption on nanocrystalline apatites, J Colloid Interf Sci, 420 (2014) 101-111.
[95] Y.J. Oh, G. Choi, Y.B. Choy, J.W. Park, J.H. Park, H.J. Lee, Y.J. Yoon, H.C. Chang, J.H. Choy, Aripiprazole-Montmorillonite: A New Organic-Inorganic Nanohybrid Material for Biomedical Applications, Chem-Eur J, 19 (2013) 4869-4875.
[96] J.S. Baek, H.H. Kwon, J.S. Hwang, H.C. Sung, J.M. Lee, S.C. Shin, Y.R. Kim, C.W. Cho, Alendronate-loaded microparticles for improvement of intestinal cellular absorption, J Drug Target, 19 (2011) 37-48.
[97] G.I. Im, S.A. Qureshi, J. Kenney, H.E. Rubash, A.S. Shanbhag, Osteoblast proliferation and maturation by bisphosphonates, Biomaterials, 25 (2004) 4105-4115.
[98] S.J. Choi, J.M. Oh, J.H. Choy, Biocompatible ceramic nanocarrier for drug delivery with high efficiency, J Ceram Soc Jpn, 117 (2009) 543-549.
[99] C.G. Ambrose, T.O. Clanton, Bioabsorbable implants: Review of clinical experience in orthopedic surgery, Ann Biomed Eng, 32 (2004) 171-177.
[100] P.B. Maurus, C.C. Kaeding, Bioabsorbable implant material review, Oper Techn Sport Med, 12 (2004) 158-160.
[101] M. Niinomi, Recent metallic materials for biomedical applications, Metall Mater Trans A, 33 (2002) 477-486.
[102] U. Yolcu, H. Alan, S. Malkoc, S.B. Bozkurt, S.S. Hakki, Cytotoxicity Evaluation of Bioresorbable Fixation Screws on Human Gingival Fibroblasts and Mouse Osteoblasts by Real-Time Cell Analysis, J Oral Maxil Surg, 73 (2015).
[103] J. Poircuitte, P. Popkov, D. Huber, E. Polirsztok, P. Lascombes, P. Journeau, Resorbable osteosynthetic devices in pediatric traumatology: a prospective series of 24 cases, European Journal of Orthopaedic Surgery & Traumatology, 25 (2015) 997-1004.
[104] J.C. Middleton, A.J. Tipton, Synthetic biodegradable polymers as orthopedic devices, Biomaterials, 21 (2000) 2335-2346.
[105] P.U. Rokkanen, O. Bostman, E. Hirvensalo, E.A. Makela, E.K. Partio, H. Patiala, S. Vainionpaa, K. Vihtonen, P. Tormala, Bioabsorbable fixation in orthopaedic surgery and traumatology, Biomaterials, 21 (2000) 2607-2613.
[106] W. Wu, J. Zhou, C.T. Xu, J. Zhang, Y.J. Jin, G.L. Sun, Biomechanical evaluation of maxillary Lefort I fracture with bioabsorbable osteosynthesis internal fixation, Dent Traumatol, 30 (2014) 447-454.
[107] G. Buijs, E.B. van der Houwen, R.R.M. Bos, G.J. Verkerke, Mechanical strength and stiffness of biodegradable and titanium osteofixation systems, J Oral Maxil Surg, 65 (2007) 2148-2158.
[108] R.M. Laughlin, M.S. Block, R. Wilk, R.B. Malloy, J.N. Kent, Resorbable plates for the fixation of mandibular fractures: A prospective study, J Oral Maxil Surg, 65 (2007) 89-96.
[109] A. Artola, M. Gurruchaga, B. Vazquez, J. San Roman, I. Goni, Elimination of barium sulphate from acrylic bone cements. Use of two iodine-containing monomers, Biomaterials, 24 (2003) 4071-4080.
[110] K.W. Davy, M.R. Anseau, C. Berry, Iodinated methacrylate copolymers

as X-ray opaque denture base acrylics, Journal of dentistry, 25 (1997) 499-505.
[111] S. Kiran, N.R. James, A. Jayakrishnan, R. Joseph, Polyurethane thermoplastic elastomers with inherent radiopacity for biomedical applications, Journal of Biomedical Materials Research Part A, 100A (2012) 3472-3479.
[112] G. Lewis, Properties of acrylic bone cement: state of the art review, Journal of biomedical materials research, 38 (1997) 155-182.
[113] G. Lewis, C.S. van Hooy-Corstjens, A. Bhattaram, L.H. Koole, Influence of the radiopacifier in an acrylic bone cement on its mechanical, thermal, and physical properties: barium sulfate-containing cement versus iodine-containing cement, Journal of biomedical materials research. Part B, Applied biomaterials, 73 (2005) 77-87.
[114] M.P. Ginebra, L. Albuixech, E. Fernandez-Barragan, C. Aparicio, F.J. Gil, R.J. San, B. Vazquez, J.A. Planell, Mechanical performance of acrylic bone cements containing different radiopacifying agents, Biomaterials, 23 (2002) 1873-1882.
[115] H. Bala, W. Fu, Y. Guo, J. Zhao, Y. Jiang, X. Ding, K. Yu, M. Li, Z. Wang, In situ preparation and surface modification of barium sulfate nanoparticles, Colloids and Surfaces A: Physicochemical and Engineering Aspects, 274 (2006) 71-76.
[116] A. Ricker, P. Liu-Snyder, T.J. Webster, The influence of nano MgO and BaSO4 particle size additives on properties of PMMA bone cement, International journal of nanomedicine, 3 (2008) 125.
[117] C. Shasteen, S.M. Kwon, K.Y. Park, S.Y. Jung, S.H. Lee, C.G. Park, M.H. Kim, S. Kim, W.C. Son, T.H. Choi, Y.B. Choy, Biodegradable internal fixation plates enabled with X-ray visibility by a radiopaque layer of beta-tricalcium phosphate and poly (lactic-co-glycolic acid), J Biomed Mater Res B, 101B (2013) 320-329.
[118] S.Y. Choi, W. Hur, B.K. Kim, C. Shasteen, M.H. Kim, L.M. Choi, S.H. Lee, C.G. Park, M. Park, H.S. Min, S. Kim, T.H. Choi, Y.B. Choy, Bioabsorbable bone fixation plates for X-ray imaging diagnosis by a radiopaque layer of barium sulfate and poly(lactic-co-glycolic acid), J Biomed Mater Res B, 103 (2015) 596-607.
[119] F. Mottu, D.A. Rufenacht, E. Doelker, Radiopaque polymeric materials for medical applications - Current aspects of biomaterial research, Invest Radiol, 34 (1999) 323-335.
[120] T.H. Kim, I. Heo, S.M. Paek, C.B. Park, A.J. Choi, S.H. Lee, J.H. Choy, J.M. Oh, Layered Metal Hydroxides Containing Calcium and Their Structural Analysis, B Kor Chem Soc, 33 (2012) 1845-1850.
[121] Y. Kuang, L.N. Zhao, S.A. Zhang, F.Z. Zhang, M.D. Dong, S.L. Xu, Morphologies, Preparations and Applications of Layered Double Hydroxide Micro-/Nanostructures, Materials, 3 (2010) 5220-5235.
[122] A.A. Ignatius, L.E. Claes, In vitro biocompatibility of bioresorbable polymers: poly(L, DL-lactide) and poly(L-lactide-co-glycolide), Biomaterials, 17 (1996) 831-839.
[123] S. Li, Hydrolytic degradation characteristics of aliphatic polyesters

derived from lactic and glycolic acids, J Biomed Mater Res (Appl Biomter), 48 (1999) 342-353.
[124] W. Rasband, Bethesda, Maryland: US National Institutes of Health; 1997-2008. ImageJ, in.
[125] T. An, J. Choi, A. Kim, J.H. Lee, Y. Nam, J. Park, B. kyung Sun, H. Suh, C.-j. Kim, S.-J. Hwang, Sustained release of risperidone from biodegradable microspheres prepared by in-situ suspension-evaporation process, Int J Pharmaceut, 503 (2016) 8-15.
[126] F. Xin, C. Jian, R. Jianming, Z. Zhongcheng, Z. Jianpeng, Effects of surface modification on the properties of poly (lactide-co-glycolide) composite materials, Polymer-Plastics Technology and Engineering, 48 (2009) 658-664.
[127] H. Maki, M. Takigawa, M. Mizuhata, Nickel-Aluminum Layered Double Hydroxide Coating on the Surface of Conductive Substrates by Liquid Phase Deposition, Acs Appl Mater Inter, 7 (2015) 17188-17198.
[128] J.A. Dyer, N.C. Scrivner, S.K. Dentel, A practical guide for determining the solubility of metal hydroxides and oxides in water, Environ Prog, 17 (1998) 1-8.
[129] J. Kobayashi, R. Kizu, H. Sugiyama, Influences of polyaromatic hydrocarbons and heavy metals on a thyroid carcinoma cell line, Journal of health science, 51 (2005) 202-206.
[130] S. Lanone, F. Rogerieux, J. Geys, A. Dupont, E. Maillot-Marechal, J. Boczkowski, G. Lacroix, P. Hoet, Comparative toxicity of 24 manufactured nanoparticles in human alveolar epithelial and macrophage cell lines, Part Fibre Toxicol, 6 (2009).
[131] L.E. Gerweck, K. Seetharaman, Cellular pH gradient in tumor versus normal tissue: potential exploitation for the treatment of cancer, Cancer Res, 56 (1996) 1194-1198.
[132] D.P. Coletti, A. Salama, J.F. Caccamese, Application of intermaxillary fixation screws in maxillofacial trauma, J Oral Maxil Surg, 65 (2007) 1746-1750.
[133] D. D'Avella, L. Denaro, V. Denaro, Pitfalls in Cervical Spine Surgery: Avoidance and Management of Complications, Springer, 2010.
[134] J.H. Noh, Y.H. Roh, B.G. Yang, S.W. Kim, J.S. Lee, M.K. Oh, Outcomes of operative treatment of unstable ankle fractures: a comparison of metallic and biodegradable implants, J Bone Joint Surg Am, 94 (2012) e166.
[135] H.M. Wong, K.W.K. Yeung, K.O. Lam, V. Tam, P.K. Chu, K.D.K. Luk, K.M.C. Cheung, A biodegradable polymer-based coating to control the performance of magnesium alloy orthopaedic implants, Biomaterials, 31 (2010) 2084-2096.
[136] H.Y. Tian, Z.H. Tang, X.L. Zhuang, X.S. Chen, X.B. Jing, Biodegradable synthetic polymers: Preparation, functionalization and biomedical application, Prog Polym Sci, 37 (2012) 237-280.
[137] A.J.R. Lasprilla, G.A.R. Martinez, B.H. Lunelli, A.L. Jardini, R. Maciel, Poly-lactic acid synthesis for application in biomedical devices - A review, Biotechnol Adv, 30 (2012) 321-328.
[138] C.C. Wu, C.L. Kuo, F.Y. Fan, K.C. Yang, Strontium-Impregnated

Bioabsorbable Composite for Osteoporotic Fracture Fixation, Journal of Biomedical Materials Research Part A, (2015).
[139] W. Hur, M. Park, J.Y. Lee, M.H. Kim, S.H. Lee, C.G. Park, S.-N. Kim, H.S. Min, H.J. Min, J.H. Chai, Bioabsorbable bone plates enabled with local, sustained delivery of alendronate for bone regeneration, Journal of Controlled Release, (2015).
[140] D.W. Lee, Y.P. Yun, K. Park, S.E. Kim, Gentamicin and bone morphogenic protein-2 (BMP-2)-delivering heparinized-titanium implant with enhanced antibacterial activity and osteointegration, Bone, 50 (2012) 974-982.
[141] T.X. Gong, Z.Q. Wang, Y.B. Zhang, C.S. Sun, Q.Z. Yang, T. Troczynski, U.O. Hafeli, Preparation, characterization, release kinetics, and in vitro cytotoxicity of calcium silicate cement as a risedronate delivery system, Journal of Biomedical Materials Research Part A, 102 (2014) 2295-2304.
[142] T. Andersson, F. Agholme, P. Aspenberg, P. Tengvall, Surface immobilized zoledronate improves screw fixation in rat bone: A new method for the coating of metal implants, J Mater Sci-Mater M, 21 (2010) 3029-3037.
[143] Y. Gao, E. Luo, J. Hu, J. Xue, S.S. Zhu, J.H. Li, Effect of combined local treatment with zoledronic acid and basic fibroblast growth factor on implant fixation in ovariectomized rats, Bone, 44 (2009) 225-232.
[144] W.L. Gou, X. Wang, J. Peng, Q. Lu, Y. Wang, A.Y. Wang, Q.Y. Guo, X.P. Gao, W.J. Xu, S.B. Lu, Controlled Delivery of Zoledronate Improved Bone Formation Locally In Vivo, Plos One, 9 (2014).
[145] S. Niu, X.R. Cao, Y. Zhang, Q.S. Zhu, J.Y. Zhu, P. Zhen, Peri-implant and systemic effects of high-/low-affinity bisphosphonate-hydroxyapatite composite coatings in a rabbit model with peri-implant high bone turnover, Bmc Musculoskel Dis, 13 (2012).
[146] F. Daubine, D. Cortial, G. Ladam, H. Atmani, Y. Haikel, J.C. Voegel, P. Clezardin, N. Benkirane-Jessel, Nanostructured polyelectrolyte multilayer drug delivery systems for bone metastasis prevention, Biomaterials, 30 (2009) 6367-6373.
[147] W. Ji, H.A. Wang, J.J.J.P. van den Beucken, F. Yang, X.F. Walboomers, S. Leeuwenburgh, J.A. Jansen, Local delivery of small and large biomolecules in craniomaxillofacial bone, Adv Drug Deliver Rev, 64 (2012) 1152-1164.
[148] H.S. Alghamdi, J.A. Jansen, Bone Regeneration Associated with Nontherapeutic and Therapeutic Surface Coatings for Dental Implants in Osteoporosis, Tissue Eng Part B-Re, 19 (2013) 233-253.
[149] N.Y.C. Yu, M. Gdalevitch, C.M. Murphy, K. Mikulec, L. Peacock, J. Fitzpatrick, L.C. Cantrill, A.J. Ruys, J.J. Cooper-White, D.G. Little, A. Schindeler, Spatial Control of Bone Formation Using a Porous Polymer Scaffold Co-Delivering Anabolic Rhbmp-2 and Anti-Resorptive Agents, Eur Cells Mater, 27 (2014) 98-111.
[150] R. Rizzoli, K. Åkesson, M. Bouxsein, J. Kanis, N. Napoli, S. Papapoulos, J.-Y. Reginster, C. Cooper, Subtrochanteric fractures after long-term treatment with bisphosphonates: a European society on clinical and economic aspects of osteoporosis and osteoarthritis, and international osteoporosis foundation working group report, Osteoporosis Int, 22 (2011) 373-390.

[151] P.N. Sambrook, C. Roux, J.-P. Devogelaer, K. Saag, C.-S. Lau, J.-Y. Reginster, C. Bucci-Rechtweg, G. Su, D.M. Reid, Bisphosphonates and glucocorticoid osteoporosis in men: results of a randomized controlled trial comparing zoledronic acid with risedronate, Bone, 50 (2012) 289-295.
[152] X. Liu, S. Qu, X. Lu, X. Ge, Y. Leng, Time-of-flight secondary ion mass spectrometry study on the distribution of alendronate sodium in drug-loaded ultra-high molecular weight polyethylene, Biomedical Materials, 4 (2009) 065008.
[153] F. Benyettou, J. Hardouin, J.H. Marc Lecouvey, L. Motte, PEGylate d Versus Non-PEGylated ɣFe 2 O 3@ Alendronate Nanoparticles, J Bioanal Biomed, 4 (2012) 39-45.
[154] N. Redman-Furey, M. Dicks, A. Bigalow-Kern, R.T. Cambron, G. Lubey, C. Lester, D. Vaughn, Structural and analytical characterization of three hydrates and an anhydrate form of risedronate, J Pharm Sci-Us, 94 (2005) 893-911.
[155] A.M. Hounslow, J. Carran, R.J. Brown, D. Rejman, G.M. Blackburn, D.J. Watts, Determination of the microscopic equilibrium dissociation constants for risedronate and its analogues reveals two distinct roles for the nitrogen atom in nitrogen-containing bisphosphonate drugs, J Med Chem, 51 (2008) 4170-4178.
[156] T.H. Kim, G.J. Lee, J.H. Kang, H.J. Kim, T.I. Kim, J.M. Oh, Anticancer Drug-Incorporated Layered Double Hydroxide Nanohybrids and Their Enhanced Anticancer Therapeutic Efficacy in Combination Cancer Treatment, Biomed Res Int, (2014).
[157] K. Ladewig, M. Niebert, Z.P. Xu, P.P. Gray, G.Q.M. Lu, Efficient siRNA delivery to mammalian cells using layered double hydroxide nanoparticles, Biomaterials, 31 (2010) 1821-1829.
[158] E. Vaculikova, D. Placha, M. Pisarcik, P. Peikertova, K. Dedkova, F. Devinsky, J. Jampilek, Preparation of Risedronate Nanoparticles by Solvent Evaporation Technique, Molecules, 19 (2014) 17848-17861.
[159] D.E. Hughes, K.R. Wright, H.L. Uy, A. Sasaki, T. Yoneda, D.G. Roodman, G.R. Mundy, B.F. Boyce, Bisphosphonates promote apoptosis in murine osteoclasts in vitro and in vivo, J Bone Miner Res, 10 (1995) 1478-1487.
[160] P. Heidari, A. Abbaspour, T. Baghdadi, R. Espandar, M. Farzan, S. Amanpour, M.R. Rasouli, M.A. Mohagheghi, H.R. Amiri, N. Yasui, Effect of risedronate on bone resorption during the consolidation phase of distraction osteogenesis: a rabbit model, Journal of orthopaedic surgery, 18 (2010).
[161] M. Gass, B. Dawson-Hughes, Preventing osteoporosis-related fractures: An overview, Am J Med, 119 (2006) 3S-11S.

# Abstract in Korean

# 국문 초록

본 논문은 다양한 의공학 분야 중에서 금속 이중층 수산화물 (LDH) 기반의 나노 혼성체를 이용하여 정확한 질병의 진단 및 적합한 치료에 관한 것이다. 또한, 나노 혼성체가 가지는 질병의 진단 및 치료 기능을 이용하여 보다 구체적인 맞춤형 치료가 가능한 테라노시스 시스템에 대해 연구하였다.

이 논문은 금속 이중층 수산화물 (LDH)을 이용하여 질병의 진단 및 치료효과를 극대화시킬 수 있는 금속 이중층 수산화물 기반 나노혼성체의 설계, 합성 및 평가에 대한 연구이다. LDH는 음이온성 약물 및 생기능성 분자를 담지 할 수 있고 세포내 투과율이 높으며 독성이 없기 때문에 유용한 약물 전달체이다. 그리고 LDH는 표적지향성 약물 전달이 가능하며, 약물을 서방방출 하는 특성을 가지기 때문에 약이 가지는 부작용을 최소화하고 치료 효과를 극대화 시킬 수 있는 장점을 가진다. 2장에서는 약물을 담지한 금속 이중층 수산화물 기반의 나노 혼성체를 포함하는 새로운 젤 제형을 개발에 대한 내용으로 본 제형을 경피 약물전달 시스템에 적용한 결과 우수한 약물전달 제어 특성을 가짐을 확인하였다. 3장에서는 세포 내로 효과적인 약물전달을 위한 금속 이중층 수산화물 기반의 나노 혼성체는 순수 약물 대비 약 10.6 배의 세포 내 전달 특성을 보여 주며 보다 효과적인 치유 능력을 보여줌을 세포수준에서 확인하였다.

4장에서 X선 조영특성을 가지는 생체흡수성 골 고정플레이트를 제안하였다. X선 흡수계수가 상대적으로 높은 금속으로 이루어진 LDH는 방사선비투과성을 가지는 조영제로써 생분해성 고분자와 함께 결합하여 조영층을 제작한 후 생체흡수성 골고정용 플레이트에 부착하여 다양한 방법을 이용하여 평가한 결과 X선 조영특성을 가지고 생체내에서 분해가 되며 생체적합성이 우수하였다.

마지막으로 진단 및 치료 기능을 동시에 가지는 금속 이중층 수산화물 기반의 나노혼성체를 이용하여 골고정용 플레이트에 융합하여 X선 진단 및 치료의 복합적 기능을 갖춘 새로운 형태의 골고정용 시스템을 구현하였다. 이 생체흡수성 골고정용 플레이트는 수술 후에 고정 장치의 위치를 쉽게 파악할 수 있게 할 뿐만 아니라 약물의 서방방출을 통하여 골 생성에 뛰어난 효과를 가짐을 확인하였다.

---

**핵심어: 금속수산화물, 나노혼성체, 진단, 치료, 테라노시스**

**학번: 2010-21053**

# Acknowledgement

# 감사의 글

본 박사학위 논문을 마무리하기까지 수 많은 어려움 속에서 저를 격려해주시고 아낌없는 도움을 주신 많은 분들께 진심 어린 마음으로 감사의 인사를 올립니다.

가장 먼저, 한없이 부족한 저를 독립된 연구자의 길로 이끌어주신 두 분 지도 교수님들께 머리 숙여 깊이 감사 드립니다. 교수님들이 계시지 않았다면 저의 이 작지만 영광의 결실을 맺을 수 없었을 것입니다. 학위를 마치는 이 순간까지 오랜 시간 동안 학문적으로나 인격적으로 수없이 많은 가르침을 주신 이화여자대학교 최진호 교수님께 감사 드립니다. 교수님의 연구자로서의 열정과 진지함 그리고 연구 인생철학은 앞으로 저의 독립된 연구자의 인생에 가장 존귀한 밑거름이 될 것이라고 생각합니다. 교수님의 마지막 남자제자로서 부끄럽지 않고 자랑스러운 제자가 되도록 항상 노력하겠습니다. 저를 항상 사랑으로 보살펴주신 최영빈 교수님께 진심으로 감사 드립니다. 교수님과 함께한 학위기간은 정말 따뜻했습니다. 학위과정 내내 너무나도 부족한 저를 믿어주시고 올바른 방향으로 인도하시며 연구 내외적으로 많은 가르침을 주셔서 감사합니다. 교수님의 가르침 덕분에 연구자란 무엇이며, 특히 교육자란 무엇인가에 대한 의미 있는 성찰을 할 수 있었습니다. 진정한 엔지니어로서 교수님을 본 받아 훌륭한 연구자가 되도록 쉼 없이 노력하겠습니다. 또한, 바쁘신 일정 중에 소중한 시간을 내주셔서 학위

심사를 맡아주신 김희찬 교수님, 최태현 교수님, 이정찬 교수님께 깊은 감사를 드립니다. 더불어 자주 뵙지는 못했지만 학과를 잘 이끌어 주시고 훌륭한 연구자의 모습을 보며 대학원 생활에 힘을 얻게 해주신 박광석 교수님, 윤형진 교수님, 최진욱 교수님, 김성완 교수님께도 감사의 인사를 드립니다.

석박사 통합과정 13학기 동안 함께 동거 동락했던 이화여자대학교 지능형 나노 바이오 소재 연구실 선후배님들과 서울대학교 생체재료공정 연구실 동료들에게도 모두 감사의 인사를 전합니다. 먼저 이화여대 연구실을 잘 이끌어 주시고 실험 및 연구에 대해서 아낌 없이 조언해주신 양재훈 박사님께 먼저 감사 드립니다. 힘든 학위과정 중에 뵐 때 마다 대학원 생활에 많은 조언을 해주시고 이화여자 대학교 황성주 교수님, 동국대학교 정현 교수님, 연세대학교 오제민 교수님, 서울여자대학교 최수진 교수님들께 감사의 인사를 올립니다. 주옥 같은 말씀들을 마음 깊게 새기고, 떠올리며 선배님들을 따라 훌륭한 연구자가 되도록 성심껏 노력 하겠습니다.

실험실에서 가장 의지하고 함께 했던 김수연 박사, 연구뿐 아니라 여러모로 많은 도움을 주신 최고은 박사, 퇴근길에 행복한 담소를 함께 즐긴 새란누나, 마음 따뜻한 지희누나에게도 고맙다는 인사를 전합니다. 그리고 오랜시간 함께 생활한 현주, 일용, 혜연, 지영이에게 감사를 전하며, 하루 빨리 목표로 한 것들을 달성하길 기원합니다. 지금은 아니지만 실험실을 나가 새로운 곳에서 잘 지내고 있는 재용이형, 가인이, 가영이, 미령이에게도 함께 감사의 인사를 전합니다.

언제나 고민을 나누고 함께한 타이거즈 정신의 박민 박사, 지금은 멀리 미국에서 공부하고 있지만 늘 마음 한 부분을 차지하는 고마운 박천권 박사, 처음 만남부터 상쾌했고 지금은 우리 연구실을 잘 이끌고 있는

승호, 늘 긍정적이고 따뜻한 마음을 가진 범강이형, 단단한 마음으로 연구실을 책임지고 있는 세나누나, 멀리 있어 자주 보지는 못했지만 항상 응원해주는 분당방장 병휘형 모두 진심으로 고맙습니다. 서울대에서 함께 있지 않아서 많은 이야기를 나누지 못하였지만 늘 볼 때마다 응원해주고 친절하게 맞이해준 생체재료공정연구실 석사과정 용찬, 재연, 송아, 병호, 동연, 한비, 지민, 범수에게도 감사의 인사를 전합니다. 연구에서 함께 생활 하던 Katie, 지은, 성윤, 수빈에게도 이 글을 통해 함께 있을 때는 말 못했지만 매 순간 고맙고 함께 할 수 있어서 행복했다는 말을 전하고 싶습니다. 그리고 함께 연구에 대해서 미래에 대해서 고민을 나눈 우종, 시완, 민영, 한나, 희윤, 소진에게 짧은 시간이었지만 고생했고 많이 도움 줘서 고맙고 함께 할 수 있어서 즐거웠다고 전하고 싶습니다.

학위과정 기간에 알게 되었지만 평생을 함께 응원하며 성장해 나갈 마음이 따뜻한 준식이, 만날 때 마다 먼 미래를 함께 설계하는 윤진이에게 고맙다는 말을 전하고 싶다. 특히 우리의 사랑하는 마음 절대 변치 않고 한결같이 곁에서 힘이 되어 주고 세상을 바꿀 수 있는 그 무엇을 만들 수 있도록 노력해보자. 학위과정 중이라, 가정을 위하여 자주 만나지 못했지만 마음으로 응원해주신 연수고 친구들, 리액션 선후배님, 샌디에이고 모임 친구들에게도 죄송한 마음과 더불어 감사의 인사를 전합니다. 앞으로 자주 연락하고 모임에서 만날 수 있었으면 좋겠습니다.

마지막으로 제게 주신 사랑과 관심에 대해서 감사의 마음을 형언할 길이 없는 가족에게 이 영광을 함께 돌립니다. 먼저, 묵묵히 아들이 하는 일을 모두 믿어 주시고 지지해주시는 아버지, 언제나 사랑과 관심으로 응원해주시는 어머니께 무한한 감사 인사를 올립니다. 이제 한 가정의 가장으로서 부모님께 효도하고 행복한 모습만 보여드리겠습니다.  늘 바쁘다고 연락을 못한 동생 나영에게도 언제나 오빠를 믿고 사랑해줘서

고맙다는 말 전하고 싶다. 지혜롭고 현명하며 세상에서 가장 사랑하는 아내 수진에게도 감사의 말을 전합니다. 늘 힘들어하고 짜증내고 불만만 늘어놓았던 나의 모습을 반성하며 이제 더 행복한 한 가정의 가장, 그리고 자상하고 존경할 수 있는 남편이 될 수 있도록 끊임없이 노력하겠습니다. 학위 기간 중에 태어난 우리 사랑스런 덩이, 언제나 환하게 미소 지으며 아빠는 훌륭한 과학자라고 응원해준 진우야 고맙고 사랑해. 더불어, 늘 한마음 한 뜻으로 응원해주신 장인어른, 장모님, 처형, 동서 형님께도 감사의 인사를 드립니다. 다시 한번 저를 사랑해주신 많은 분들께 감사 드리며 하시는 일 모두 잘 풀리시고 늘 건강하시길 기원합니다.

한 가정의 가장으로서, 아버지로서, 아들로서, 사위로서, 훌륭한 제자로서 무거운 책임감을 가지고 새로운 세상으로 나아가고자 합니다. 저의 마음 속 깊은 곳에 분에 넘치는 사랑을 안고 언제나 자랑스러운 김명훈이 되도록 하루하루 열심히 노력하겠습니다. 감사합니다.

2016년 7월 사랑하는 사람들을 그리며...

김 명 훈

# APPENDIX

## EDUCATION

☐ Ph. D. Mar. 2010–Aug. 2016

Interdisciplinary Program in Bioengineering,
College of Engineering, Seoul National University
Supervisor: Professor Young Bin Choy
Dissertation Topic: LAYERED DOUBLE HYDROXIDE BASED NANOHYBRIDS FOR DIAGNOSIS AND THERAPY

☐ B. S. Mar. 2005–Feb. 2010

Department of Chemical and Biomolecular Engineering
College of Engineering, Yonsei University

## PUBLICATIONS

1. **Kim M. H.**[+], Jun Y. J.[+], Elzatahry A., Alothman Z. A., Vinu A., Choy Y.B.[*], Choy J.–H.[*], Hydrophobic Guest Mediated Micellization and Demicellization of Rationally Designed Amphiphilic Poly(organophosphazene) for Efficient Drug Delivery, Science of Advanced Materials, accepted.

2. **Kim M. H.**, Elzatahry A., Vinu A., Choy Y. B., Choy J.–H.[*], Clay–drug hybrid Materials for biomedical applications; administration routes, Clays and Clay Minerals, accepted.

3. Hur W. J.[+], Park M.[+], Lee J. Y., **Kim M. H.**, Lee S. H., Park C. G., Kim S. N., Min H. S., Min H.J., Chai J. H., Lee S. J., Kim S., Choi T. H.[*], Choy Y. B.[*], Bioabsorbable Bone Plates Enabled with Local, Sustained Delivery of Alendronate for Bone Regeneration, Journal of Controlled Release, 222, 97–106, 2016.

4. Park, S. B.+, Park, M.+, Kim, B. H.+, Lee, J. E., Park, H. J., Lee, S. H., Park, C. G., **Kim M. H.**, Kim R., Kim, E. H., Heo. C. Y.*, Choy, Y. B.*, Acute Suppression of TGF-ß with Local, Sustained Release of Tranilast against the Formation of Fibrous Capsules around Silicone Implants, Journal of Controlled Release, 200, 125-137, 2015.

5. Lee, J. E.+, Park, S.+, Park, M, **Kim M. H.**, Park, C. G., Lee, S. H., Choi, S. Y., Kim, B. H., Park, H. J., Park, J. -H., Heo, C. Y.*, Choy, Y. B.*, Surgical suture assembled with polymeric drug-delivery sheet for sustained, local pain-relief, Acta Biomaterialia, 9(9), 8318-8327, 2013.

6. Shasteen, C., Kwon, S. M., Park, K. Y., Jung, S. Y., Lee, S. H., Park, C. G., **Kim, M. H.**, Kim, S., Son, W.-C., Choi, T. H.*, Choy, Y. B.*, Biodegradable internal fixation plates enabled with X-ray visibility by a radiopaque layer of $\beta$-tricalcium phosphate and poly (lactic-co-glycolic acid), Journal of Biomedical Materials Research: Part B - Applied Biomaterials, 101(2), 320-329, 2013.

7. **Kim. M. H.**, Park D. -H., Yang. J. -H., Choy Y. B. *, Choy J. -H. *, Drug-inorganic-polymer nanohybrid for transdermal delivery, International Journal of Pharmaceutics, 444(1-2), 120-127, 2013.

8. Lee, J. E.+, Park, C. G.+, An, B. M., **Kim, M. H.**, Park, M., Lee, S. H., Choy, Y. B.*, Linear delivery of verapamil *via* nanofibrous sheet-based system, Pharmaceutical Research, 29(7), 1787-1796, 2012.

9. Park, C. G., **Kim, M. H.**, Park, M., Lee, J. E., Lee, S. H., Park, J.-H., Yoon, K.-H., Choy, Y. B.*, Polymeric nanofiber coated esophageal stent for sustained delivery of an anticancer drug, Macromolecular Research,19(11), 1210-1216, 2011.

## HONORS and AWARDS

1. Best Paper Award
   7th Conference on Bioengineering, Seoul National University, Seoul, Korea (2015)
   Paper entitled with "Theragnostic Bone Fixation System with Drug-Inorganic Nanohybrids"

2. Best Presentation Award/Grants
   Joint with 2nd Korea-France Workshop 2015, Korean Clay Science, Wonju, Korea (2015)
   Paper entitled with "Theragnostic Bone Fixation System with Drug-Clay Nanohybrids"

3. Best Paper Award/Grants
   Annual Conference, Biomedical Research Institute, Seoul National University Hospital, Seoul, Korea (2013)
   Paper entitled with "Drug-Inorganic-Polymer Nanohybrid for Transdermal Delivery"